Numerical investigation of the geophysical response to methane migration in an unconfined aquifer with implications for hydrocarbon wellbore leakage

by

Dylan Richard Klazinga

A thesis
presented to the University of Waterloo
in fulfillment of the
thesis requirement for the degree of
Master of Science
in
Earth Science

Waterloo, Ontario, Canada, 2018

I hereby declare that I am the sole author of this thesis. This is a true copy of the thesis, including any required final revisions, as accepted by my examiners.

I understand that my thesis may be made electronically available to the public.

Abstract

Methane gas leakage from oil and gas development can impact freshwater aquifers. Accurate depictions of gas migration in the subsurface will depend on knowledge of physical parameters and flow system conditions. Geophysical methods have the capacity to detect and track transient changes in gas-phase saturation; suitable methods can be deployed at surface or within boreholes depending on the required depth of investigation. While the application of geophysical methods to monitor immiscible-phase fluids in the subsurface has been extensively documented, knowledge of governing hydraulic parameters, flow system conditions, and impacts on the geophysical responses used to elucidate hydrogeologic processes remains underdeveloped. A series of numerical multi-phase flow models simulating a 72 day controlled methane leakage experiment in an unconfined aquifer at Canadian Forces Base (CFB) Borden (Cahill et al., 2017) were conducted to evaluate the utility of electrical resistivity tomography (ERT) and ground-penetrating radar (GPR) to monitor and characterize the transient evolution of the gas-phase plume, and to better understand the impacts of varying hydraulic properties and flow system conditions on the geophysical signatures used to interpret gas phase behaviour (Steelman et al., 2017). This study investigates the role of multi-phase parameters (e.g., relative permeability, air-entry pressure, and injection rate history), flow system conditions (e.g., heterogeneity, anisotropy, and groundwater velocity), and geometrical properties (e.g., confining layer thickness and continuity) on the flow of gas-phase methane emanating from a variable rate source, and the subsequent impacts of gas migration on the geophysical responses observed from surface geophysical surveys. Aquifer parameters were based on physical measurements of soil core from the injection site and literature values for the Borden sand, while the injected methane was considered to be non-reactive over the simulation period.

In a homogeneous, weakly anisotropic aquifer gas migrated vertically by buoyancy and efficiently vented to the vadose zone. As vertical migration was restricted through the addition of anisotropy, lower-permeable features, and increased horizontal groundwater velocity, an increase in the horizontal component of the gas migration was observed, leading to a broader gas-phase plume, establishment of variably distributed vertical preferential flow paths, and greater gas retention in the aquifer. The inclusion of a thin layer with moderately lower permeability with an increased entry pressure representing a thin sand lens within the aquifer, caused gas to accumulate within pools below the layer, extending farther down-gradient than would be expected from advection alone. These results showed that in all scenarios gas-phase methane mostly migrated vertically under buoyancy conditions until some barrier to vertical migration was reached, at which point gas

migrated laterally until pressures exceeded the entry pressure. Corresponding ERT and GPR models were run using the multi-phase flow model pore water saturation distributions to parametrize electrical resistivity and dielectric permittivity across the model domains using Archie's Law and the Complex Refractive Index Model, respectively. These models showed that ERT was effective at imaging the central plume (i.e., primary bulb around the shallow injector), but was less effective at detecting thinner lateral migration pathways (i.e., preferential flow paths migrating beyond the primary bulb). Conversely, GPR was able to detect thin gas pools emanating from the primary gas bulb and small-scale vertical preferential pathways arising from capillary boundaries; gradational boundaries, however, proved to be a more difficult target using GPR (e.g., outer boundary of the gas plume and gas trapped within lower-permeable layers with no increase in capillary pressure). The results of this study demonstrate that ERT and GPR can be very useful tools for longer-term monitoring of stray gas leakage in freshwater aquifers, particularly when there is a strong lateral migration component to flow and access to the contaminated aquifer zone is feasible. However, additional work remains to understand the impacts of methane oxidation (aerobic and anaerobic) on the geophysical signatures associated with gas and aqueous-phase methane migration and the role of external processes such as recharge, barometric pressure, and temperature on gas plume behaviour.

Acknowledgements

My passion for geophysics begins with a terrifying Walloon named Dr. Anthony Endres dispensing knowledge, assignments and rants on the topic of (or at least tangentially related to) geophysics. And while my interactions with my supervisor were the basis for the most difficult projects in my time at the University of Waterloo, I can't help but be grateful to him for the knowledge, advice, experience, job, caffeine, podcast recommendations, yak farm franchising rights, and friendship he has shared with me. Thank you, Tony.

In the months of field work that formed the foundation of this project and in the modelling, writing, and pondering that followed, Dr. Colby Steelman has always made himself available to smooth out the rough edges and push me to do better. I am a royal pain in the posterior and Colby has done an exceptional job of dealing with that pain.

To my committee members, Drs. Beth Parker and Andre Unger, thank you for overseeing this project and constantly urging me to dig deeper, ask hard questions, and do science well.

To CFB Borden, the scientists who have worked there and the scientists who will work there, thank you for welcoming me to your fold. Thank you for the lessons you have taught us and have yet to teach us. And a special thanks to those in the BMI experiment, thank you for making science fun.

An MSc can be maddening, thanks to those who kept me sane[1]. Max Salman, thank you for challenging me to be better and lead. Cameron Drever, I think we've seen more 3 AMs together than any person really needs to, but you made them bearable and, occasionally, bat-vomitingly fun. It's been seven long years since 1A, and I hope I've made them as good for you as you have for me.

Thank you to Sensors and Software for being so flexible and letting me work while I complete my thesis.

To my Ma and Pa, thank you for the support, love, and occasional cash injections that have shaped me into the man I am today. And to my wonderful sister Yo-yo. Thank you

[1]Well, relatively.

for the chats, visits, and never trying to fix me, but reassuring me that it's OK to be broken.

And to my love, Katelin. These past seven years have been hard on me and, because of your bottomless empathy, they have been hard on you. Thank you for supporting me and loving me, and I'm immeasurably happy that we have had and will have each other to lean on.

There are not enough words for me to thank everyone who I need to thank. So to the innumerable unnamed, thank you.

Table of Contents

List of Tables

List of Figures

From the quark to the supernova,
the wonders do not cease.
It is our attentiveness that is in short supply;
our ability and willingness
to do the work that wonder requires.

- John Green

Chapter 1

Introduction

1.1 Motivation

There are a number of environmental and public health issues surrounding hydrocarbon extraction, and understanding these issues is a vital step in their mitigation. Hydrocarbon reservoirs are typically formed when a porous host rock is covered by an impermeable layer which prevents the upward migration of buoyant hydrocarbons (Perrodon, 1983). One of the major constituents of trapped hydrocarbons is methane, either in free-gas pools floating on the top of the reservoir or as a dissolved component in the hydrocarbon resource. To extract hydrocarbons from these deposits, a well is drilled into the reservoir, possibly through a methane pocket. As the valuable hydrocarbons are extracted, methane flows up the wellbore. Leaks in a hydrocarbon extraction well can lead to groundwater contamination with free-phase methane (Osborn, Vengosh, Warner, & Jackson, 2011; Schout, Hartog, Hassanizadeh, & Griffioen, 2018), ethane (Jackson et al., 2013), or metallic ions associated with anaerobic degredation of methane (Kelly, Matisoff, & Fisher, 1985).

Figure 1.1 illustrates the migration and degradation of methane in shallow groundwater systems (Cahill et al., 2017). While much is known about the behaviour of methane in reservoirs (Perrodon, 1983), little is known about the impacts of stray gas in shallow, freshwater aquifers, particularly those used for drinking water supply. It is generally understood that free gas migrates upwards via buoyancy, and heterogeneity and anisotropy in the geologic formation will cause lateral migration. Research is needed to provide better tools for monitoring its migration and impact on groundwater quality (Vidic, Brantley, Vandenbossche, Yoxtheimer, & Abad, 2013) and public health and well-being (Council of

Canadian Academies, 2014; Royal Academy of Science, 2012).

Recent numerical studies of methane leakage from hydrocarbon production wells into overlying fresh water aquifers have illustrated the importance of multi-phase and multi-component flow system parametrization on the conceptualization of methane transport in the subsurface (e.g., Moortgat, Schwartz, & Darrah, 2018; Rice, McCray, & Singha, 2018; Roy, Molson, Lemieux, Van Stempvoort, & Nowamooz, 2016). Although the potential for methane oxidation exists, (e.g., Roy et al., 2016; Schout et al., 2018), much less is known about the mechanisms that influence rapid migration of the pressurized gas and the variably scaled dissolved-phase plumes. Moortgat et al. (2018) illustrated the importance of injection rate, existence of preferential pathways (e.g., fractures or channels) and optimal layer geometry to support lateral gas migration on the evolution of methane plumes. Rice et al. (2018) illustrated the relative importance of air-entry pressure and relative permeability parameters in achieving an accurate conceptual model of methane gas migration. It was found that variations in gas-phase pressure and saturation would significantly impact the flow rate of methane entering a freshwater aquifer; however, the evolution of the methane plume would be primarily controlled by the intrinsic permeability of the matrix.

The University of Guelph conducted a methane injection study at Canadian Forces Base (CFB) Borden to evaluate the migration of free-phase methane in an unconfined sandy aquifer and its impact on groundwater chemistry (Cahill et al., 2017). Alongside geochemical and hydrogeological monitoring to evaluate impacts on water quality (Cahill et al., 2017), the field experiment employed geophysical methods to monitor the evolution and migration of the methane gas-phase plume over time (Steelman et al., 2017). The Borden Methane Injection (BMI) Experiment is discussed further in Section 1.3.

Geophysical methods represent a powerful tool in the detection of groundwater contaminants and have been applied to a wide range of immiscible-phase liquid studies over the past 30 years (e.g., Brewster et al., 1995; Comas, Slater, & Reeve, 2005). Geophysics exploits differences in physical properties to image anomalous zones in the subsurface. Some of the most commonly measured properties include dielectric permittivity using ground-penetrating radar (GPR) and electrical resistivity using direct current electrical methods such as electrical resistivity tomography (ERT). When a contaminant is introduced to a saturated volume, it either displaces or mixes with the existing fluids, causing a change in the geophysical properties of the bulk mineral-pore water system. These changes can be measured to determine the spatial extent and temporal evolution of immiscible-phase contaminant, and can provide higher spatial sampling densities than that offered by con-

ventional groundwater monitoring techniques (Atekwana & Atekwana, 2010; Binley et al., 2015).

The BMI Experiment provided valuable insights into the migration of methane in an unconfined aquifer (Cahill et al., 2017). The research presented in this thesis aims to better understand the nature of the geophysical responses observed from time-lapse GPR and ERT measurements during the field experiment (Steelman et al., 2017) through a series of numerical simulations of the geophysical response to multiphase flow of methane gas leakage in an unconfined aquifer. Groundwater flow scenarios were developed using a range of physical properties and aquifer-aquitard geometries based on data related to the field experiment. These flow scenarios were used to develop idealized geophysical models to better understand the cumulative impacts of subsurface properties on the geophysical response observed during the field experiment.

1.2 Geophysics in the Petroleum Industry

The BMI Experiment investigated a novel use of geophysics for remediation in the oil and gas industry. While this application of geophysical methods is new to the industry, geophysics is already being used extensively for oil and gas exploration. The majority of this work is to image deep geologic features that trap gas and buoyant hydrocarbons (Dobrin & Savit, 1988). While a number of methods may be employed, seismic reflection is the most commonly used technique due to its capacity to measure kilometers into the earth and provide a geometrically accurate image of sedimentary boundaries and structures. This method accounts for 90% of geophysical exploration in the oil and gas industry (Bret-Rouzaut & Favennec, 2011).

The first use of geophysics in the oil and gas industry occurred with the Eötvös Torsion Balance, a gravitational method used to map salt domes at known production fields (Dobrin & Savit, 1988; Shaw & Lancaster-Jones, 1922). In the 1920s, this method was used for oil and gas exploration in the Gulf Coast (Dobrin & Savit, 1988), about the same time that seismic refraction was introduced in oil and gas exploration. Both methods were used to locate the salt domes that act as a cap on typical oil and gas deposits.

In the Soviet Union more interest was given to electrical methods than in other areas of the world (U. S. Exchange Delegation in Exploration Geophysics, 1974). While many of

these methods focussed on structural mapping (U. S. Exchange Delegation in Petroleum Geophysics, 1966) work was also done in the direct detection of oil and gas deposits and aureoles formed above deposits from leaked gas (Spies, 1983). These aureoles corresponded to zones of higher resistivity by a factor of 3.

1.3 Borden Methane Injection Experiment

The University of Guelph conducted a methane injection experiment in the Borden aquifer in order to better understand subsurficial methane migration and its impact on groundwater (Cahill, Parker, Mayer, Mayer, & Cherry, 2018; Cahill et al., 2017; Steelman et al., 2017). Over a period of 72 days, a total of 51.35 m^3 was injected into the sandy unconfined aquifer. Using a variety of hydrogeological, geophysical, and geochemical methods, the migration of the methane was characterized. These methods indicated that approximately half of the gas quickly (hours to days after the start of the injection) vented to the atmosphere, while the other half remained in the groundwater for an extended period of time (weeks to months) (Cahill et al., 2017). Despite the growth of methanotrophic bacteria, methane remained entrapped in the groundwater, while gas vented to the vadose zone oxidized.

Time-lapsed geophysical methods were used to delineate the extent of methane migration in the subsurface (Steelman et al., 2017). The formation of a gas plume down-gradient of the shallow injector was observed using ERT and GPR. The geophysically delimited gas-plume was accompanied by increases in the total dissolved gas pressure within the aquifer. Three major temporal peaks in reflectivity were noted in the radargram time-series (Days 8, 37, and 65) which indicate transient gas build-ups followed by large lateral gas release events. The largest GPR response was identified between Days 51 and 72. Based on these data, the methane travelled farther down-gradient than expected based on groundwater advection alone. Following these releases, gas was observed to accumulate at preexisting reflectors corresponding to stratigraphic boundaries with contrasts in hydraulic permeability. After the gas injection was stopped, the reflectivity of these reflectors diminished over time, indicating buoyancy driven migration and/or dissolution into the groundwater.

This experiment demonstrated the capacity of surface geophysics to track the transient behaviour of gas-phase methane (Steelman et al., 2017). The authors of the study concluded that heterogeneity and anisotropy in hydraulic parameters strongly controlled the lateral

migration pathways, including the periodic gas build-up and release events. Field observations revealed that gas migration extended much farther down-gradient than expected from advection alone and occurred through a series of rapid lateral migration events irrespective of changes in the injection rate. However, the exact role of the stratigraphic structures and their properties (e.g., permeability, capillary pressure, geometry) on the geophysical signatures associated with the migration and fate of the free-gas in the aquifer was not fully understood. A number of build-up and release events were detected during periods of constant injection rate. The factors controlling the timing of these releases remain poorly understood. Determining the factors that control the lateral migration pathways and the dynamic behaviour of the free gas in groundwater serves as the primary motivation for this thesis.

1.4 Study Objectives

Perhaps the most interesting observation from the Borden Methane Injection (BMI) Experiment was the impact of centimetre-scale bedding or sedimentary laminations on the flow of free-phase gas; an observation that has been made in a number of different studies concerning the migration of free phases in the saturated subsurface across the CFB Borden Research area, and other analogous sites (see Section 2.4).

This study seeks to better understand how factors, such as permeability contrast, entry pressure, stratigraphic structures, and groundwater flow, impact the migration of free-phase methane, and how these migration patterns in turn impact the geophysical response over time. This is achieved by defining a basic flow model and systematically adjusting the model parameters to produce a range of flow system scenarios to stylistically capture physical elements of the Borden aquifer believed to be contributing to the observed evolution in the gas-phase plume. Using the outputs of these flow models, the gas distribution at a given time is converted to dielectric permittivity and resistivity (inverse of conductivity) distributions. In this way, the multi-phase flow models are used as an input for modelling the geophysical response observed in the ERT and GPR data.

Modelling is completed using off-the-shelf modelling software packages: multi-phase flow modelling uses CompFlowBio (Unger, Sudicky, & Forsyth, 1995); ERT response modelling uses Res2DMod (Loke, 2002); and GPR response modelling uses ReflexW (Sandmeier, 2017). Discretization of the multi-phase flow model is relatively coarse (10 cm $\times$ 10 cm

cells), as is the modelling for the geophysical responses. These models are not intended to be predictive, but instead provide a stylistic response of the considered geophysical methods to the different subsurface conditions impacting the migration of the free-phase methane.

The free-phase flow modelling accounts for neither aerobic nor anaerobic degradation of the methane, nor geochemical reactions caused by the presence of the methane. Since these simplifications are included in the free-phase flow model, they will be inherited by the geophysical modelling. Further, changes in the geophysical properties along the mineral grain surface are not considered when determining the geophysical response of a gas distribution at a time. These processes were not considered because of the experiment's relatively short time scale (i.e., a 72 day injection). The primary objective of this study is to understand the transient behaviour of the methane gas plume within the aquifer during the active injection period. Additionally, the influence of temperature on the viscosity, dielectric permittivity, and electrical conductivity, as well as precipitation, evapotranspiration, and barometric pressure will be ignored. A constant temperature of 10°C, an average recharge of 0.7 mm/day, and a barometric pressure of 100 kPa were assumed for these simulations.

Several conclusions were drawn from the geochemical and geophysical evidence collected during the BMI Experiment (Cahill et al., 2018, 2017; Steelman et al., 2017). First, it was observed that the gas-phase is highly mobile and laterally extensive in groundwater; lateral migration is much faster and extends farther than that predicted by advection alone. Second, the gas-phase preferentially accumulates beneath subtle permeability contrasts or grain-scale bedding features; occassionally exhibiting periodic ebullition events resulting in sudden lateral and vertical migration. Finally, the plume will likely persist for at least one year with minimal microbial degradation.

Although GPR and ERT measurements yielded convincing evidence of gas-phase distribution and migration in the aquifer, the physical mechanisms that contributed to the evolution of the gas-phase plume and their contributions to the geophysical response were not fully understood. Therefore, this thesis will address the following questions relating to the interpretation of geophysical measurements collected during the field experiment (Steelman et al., 2017):

1. What is the relative sensitivities of GPR and ERT to porewater saturation changes

during variable rate methane leakage in a shallow unconfined aquifer?

2. What are the primary physical controls on the evolution of a free-gas plume in an unconfined aquifer?

3. How do these physical constraints influence the establishment of vertical preferential pathways to the vadose zone, gas distribution, and storage within the aquifer?

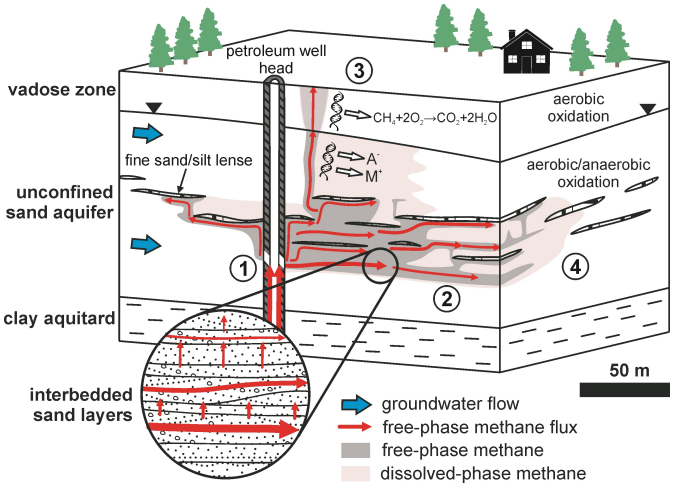

Figure 1.1: A conceptual model showing a methane leak from a well. (1) A compromised well casing releasing methane; (2) lateral migration of free-phase gas, controlled by subtle variations in geology; (3) variable methane efflux at surface; (4) a temporally persistent dissolved methane plume. Within the vadose zone the methane is degraded via microbes, but within the saturated zone degradation is negligible. The plume will migrate according to the geologic and hydrogeologic conditions present at the site (*from* Cahill et al., 2017).

Chapter 2

Background

2.1 Multi-phase Flow

Soil can be described as a three phase system: the solid particles, the liquids in the pore space, and the gas in the pore space. Typically, the pore fluids are water and air; however, other fluids can occupy the pore space of a soil. Gas can enter a soil system by displacing other pore fluids (i.e., imbibition) or through dissolution into the existing pore fluid.

Using conservation of mass for gas and water phases, the migration of a gas-phase contaminant can be mathematically modelled. The rate of migration in a medium is controlled by hydraulic conductivity, a property of both the soil and the fluid (Fetter, 1992). To separate the effects from the fluid and the effects from the medium the hydraulic conductivity can be expressed as:

$$K(\theta) = \frac{k_r(\theta) k \rho_w g}{\mu_w} \tag{2.1}$$

where:

- $K(\theta)$ is hydraulic conductivity (m/s) as a function θ,
- θ is volumetric water content (m^3/m^3),

- $k_r(\theta)$ is relative permeability (unitless) as a function of θ,
- k is intrinsic permeability of the medium (m^2),
- ρ_w is density of the pore water at a given temperature (kg/m^3),
- g is acceleration due to gravity (m/s^2),
- μ_w is dynamic viscosity of the pore water at a given temperature (Pa·s).

The pressure at which imbibtion occurs is called the air-entry pressure or capillary pressure (P_c) and is a characteristic of the pore geometry (Fetter, 1992). Leverett (1940) established that the capillary pressure is proportional to the squared inverse of the hydraulic permeability of a material. Thus for a decrease in hydraulic permeability by a factor of 4, the entry pressure doubles. When the pressure exceeds the air-entry pressure the soil will desaturate, asymptotically approaching the residual saturation. Brooks and Corey (1964) relate the pressure and the water content (Figure 2.1a) by:

$$S_e = \frac{S - S_r}{1 - S_r} = \frac{\theta - \theta_r}{\phi - \theta_r} = \left(\frac{P}{P_c}\right)^{-\lambda} \tag{2.2}$$

where:

- S_e is effective saturation (unitless),
- S is saturation (m^3/m^3),
- S_r is residual saturation (m^3/m^3),
- θ_r is residual volumetric water content (m^3/m^3),
- ϕ is porosity (m^3/m^3),
- P is pressure of the non-wetting phase (N/m^2),
- P_c is entry pressure of the medium (N/m^2),
- λ is Brooks-Corey Parameter, a property of the soil (unitless).

As desaturation occurs, the relative hydraulic permeability for the pore fluid decreases (Figure 2.1b). Using the Brooks-Corey Model (Brooks & Corey, 1964), the relative permeability for the wetting phase (k_{rw}), typically water, is calculated by:

$$k_{rw} = \left(\frac{P}{P_c}\right)^{-(2+3\lambda)} \quad \text{for} \quad P \geq P_c \tag{2.3}$$

or :

$$k_{rw} = (S_e)^{\frac{2+3\lambda}{\lambda}} \quad \text{for} \quad 0 \leq S_e \leq 1 \tag{2.4}$$

Conversely, relative permeability of the fluid that is displacing the native pore fluid (k_{rnw}) increases (Figure 2.1b) and can be calculated using (Brooks & Corey, 1964):

$$k_{rnw} = \left[1 - \left(\frac{P}{P_c}\right)^{-\lambda}\right]^2 \left[1 - \left(\frac{P}{P_c}\right)^{-(2+\lambda)}\right] \quad \text{for} \quad P \geq P_c \tag{2.5}$$

or :

$$k_{rnw} = [1 - (S_e)]^2 \left[1 - (S_e)^{\frac{2+\lambda}{\lambda}}\right] \quad \text{for} \quad 0 \leq S_e \leq 1 \tag{2.6}$$

As the injected gas displaces the pore water, the saturation of the soil decreases. This decrease in saturation will govern the geophysical response of the soil.

2.2 Electrical Resistivity Methods

2.2.1 Electrical Conductivity

An overview of the electrical conductivity of soil is presented by Friedman (2005). Conductivity (σ) represents the ease with which a medium conducts electricity (Burger, Sheehan, & Jones, 2006). The inverse of conductivity is resistivity ($\rho = 1/\sigma$); either term can be used

to describe the mechanisms contributing to the flow of electrical current (Burger et al., 2006). The term conductivity will be used to describe fundamental principles of electrical methods, while resistivity will be reserved for applications in the field.

Conductivity is controlled by a number of mechanisms, including: electrolytic conduction (Friedman, 2005), ohmic conduction (Robinson & Çoruh, 1988), and interfacial conduction (Ruffet, Darot, & Guéguen, 1995). In a clean, dry sand with no metal, electrical conduction is primarily a result of electrolytic conduction (i.e., the conduction of electricity through the movement of ions in a fluid). In fully or partially saturated soils, the pore water and the nature of the pore space (e.g., connectivity, pore throat size, etc.) will control the bulk conductivity of the medium. The conductivity of partially saturated porous media can be approximated by an empirical equation known as Archie's Law:

$$\sigma = \frac{\phi^m S_w^n}{a} \sigma_w \tag{2.7}$$

where:

- σ is total conductivity of the material (S/m),
- S_w is water saturation (unitless),
- ϕ is porosity of the soil (unitless),
- σ_w is conductivity of the pore fluid (S/m) (Everett, 2013).

a, m and n are empirical fitting parameters which account for the pore size, shape, and fluid distribution. The saturation exponent, n, depends on the pore fluid but typically has a value of 2 (Archie, 1942). The cementation exponent, m, represents the level of cementation in the porous media, and typically has a value between 1.3 – 2.6 (Doveton, 1986). The tortuosity factor, a, has a range of values typically between 1 and 2 (Attia, 2005). Table 2.1 provides conductivity values for some common geologic materials (Everett, 2013).

The conductivity of the pore fluid depends on a number of factors such as the ionic composition of the pore fluids (Jorgensen, 1996) and temperature (Ma, McBratney, Whelan, Minasny, & Short, 2011). These effects can alter the conductivity of the pore fluid by several orders of magnitude.

2.2.2 Data Acquisition

Electrical resistivity tomography (ERT) is a geophysical method that enables the collection of spatial variations in electrical conductivity (Everett, 2013). During ERT data collection a current is applied across a pair of electrodes and the voltage is measured across another pair of electrodes. The apparent resistivity of the material around the current-potential electrode pairs can be calculated from the applied current and measured voltage. The resistivity of the medium can be determined by accounting for the geometry of the electrodes. This section presents an overview of ERT; a more in depth summary can be found in Daily, Ramirez, Binley, and LaBrecque (2005), Zonge, Wynn, and Urquhart (2005), and Revil, Karaoulis, Johnson, and Kemna (2012).

ERT is an application of Ohm's Law, which relates the flow of electricity through a material to the electrical field within the material. Ohm's Law is commonly shown as:

$$\vec{E} = \rho\vec{j} \tag{2.8}$$

where:

- $\vec{E}$ is strength of the electric field at a point (V/m),
- ρ is resistivity of the material (Ω·m),
- $\vec{j}$ is electric current density at a point (A/m^2) (Everett, 2013).

The electric field is also related to the gradient of the electric potential, which can be expressed as:

$$\vec{E} = -\nabla V \tag{2.9}$$

Where V is the electric potential energy at a point (V) (Walker, 2011). By equating these two expressions, Ohm's Law can be expressed as:

$$\nabla V = -\rho\vec{j} \tag{2.10}$$

To collect data, four electrodes are inserted into the ground (Daily et al., 2005). Electrical current is applied across two electrodes (A and B) and the variation in electrical potential is then measured across the remaining two electrodes (M and N). There are a wide variety of electrode layouts that can be employed; the three layouts presented in Figure 2.2 are the most commonly used (Everett, 2013). The Wenner array places the potential electrodes between the current electrodes, with a constant spacing between adjacent electrodes. The Wenner-Schlumberger array uses a potential electrode pair between the current electrodes; the separation of adjacent current and potential electrodes is a multiple of the spacing between the potential electrodes. The dipole-dipole array pairs the potential electrodes and the current electrodes, and increases the separation between the pairs. A diagram of the electric current flow lines and voltage distribution in the subsurface during a dipole-dipole survey is presented in Figure 2.3 (Okpoli, 2013).

The measured resistivity for an arbitrary electrode array can be determined by using the formula:

$$\rho_a = \frac{2\pi\Delta V_{MN}}{I}\left(\frac{1}{r_{AM}} - \frac{1}{r_{BM}} - \frac{1}{r_{AN}} + \frac{1}{r_{BN}}\right)^{-1} \tag{2.11}$$

where:

- ρ_a is apparent resistivity of the equivalent homogeneous subsurface (Ω·m),
- ΔV_{MN} is voltage difference between electrodes M and N (V),
- I is current applied across electrodes A and B (A),
- r_{ij} is distance between electrodes i and j (m) (Burger et al., 2006).

By adjusting the spacing and layout of the electrodes, different spatial locations can be sampled. As the spacing between the electrodes increases, the subsurface is imaged deeper (Everett, 2013). If the entire array is moved laterally, then the zone being imaged also moves laterally.

ERT is performed by taking multiple readings with different electrode spacings at different locations (Everett, 2013). A plot called a pseudosection, which shows the approximate

position of the sampled soil volume and its corresponding apparent resistivity, can be compiled from these multiple readings. The lateral position of the sample volume is typically determined by the midpoint of the array while the depth of the sample volume is a function of the electrode spacing and configuration (Barker, 1989). For example, the dipole-dipole array uses one quarter of the distance between the two furthest electrodes as the effective investigation depth of a reading.

Following the collection of ERT data and the assembly of a pseudosection, the true resistivity distribution must be estimated through a process called inversion (Daily et al., 2005). During inversion, an initial resistivity distribution is assumed and a forward model is calculated to generate a theoretical pseudosection corresponding to the assumed resistivity distribution. Based on the differences between the true and generated pseudosections, the resistivity distribution is adjusted and the process is repeated. This procedure is repeated until the difference between the two pseudosections is below a specified threshold.

2.3 Ground-Penetrating Radar

2.3.1 Dielectric Permittivity

An overview of the dielectric properties of soil is presented by Everett (2013). Ground-penetrating radar (GPR) responds to changes in dielectric permittivity in the subsurface. Dielectric permittivity (ε) is the degree to which a material polarizes in the presence of an electrical field, which impacts the ability of the material to form an electric field. This value is typically presented in terms of the relative dielectric permittivity (κ); that is, the dielectric permittivity of a medium relative to the dielectric permittivity of a vacuum ($\varepsilon/\varepsilon_0$), where $\varepsilon_0 = 8.854 \times 10^{-12}$ F/m (Walker, 2011). Since the dielectric permittivity of all media is greater than that of a vacuum, the relative dielectric permittivity is greater than 1 for all materials. Table 2.2 gives the dielectric permittivities of some common geologic materials (Davis & Annan, 1989).

In a multi-component soil the bulk dielectric permittivity of the medium can be estimated using a general volumetric mixing model (Tsui & Matthews, 1997):

$$\kappa_T^\alpha = \sum_i \theta_i \kappa_i^\alpha \tag{2.12}$$

where:

- κ_T is dielectric permittivity of the composite medium (unitless),
- θ_i is volume fraction of the i-th component (unitless),
- κ_i is dielectric constant of the i-th component (unitless),
- α is a constant that accounts for the grain orientation relative to the electromagnetic field (Roth, Schulin, Fluhler, & Attinger, 1990, unitless).

The value of α is between -1 and 1, but is taken to be 0.5 for most geologic applications (Knight, 2001). This case is called the complex refractive index model (CRIM).

Water, the most common pore fluid, has a dielectric permittivity of 80.36 at 20°C, but varies with temperature (Roth et al., 1990), while gasses have dielectric permittivities of approximately 1 (Davis & Annan, 1989). Considering Equation 2.12, zones of gas accumulation would exhibit an overall reduction of the bulk dielectric permittivity.

Changes in the dielectric permittivity can be detected in two ways: changes in the velocity of an electromagnetic (EM) wave propagating through the medium and amplitude of reflected energy off a boundary separating two zones of dielectric permittivity (Everett, 2013). The velocity of an EM wave is given by the formula:

$$v = \frac{1}{\sqrt{\mu\varepsilon}} \tag{2.13}$$

where:

- μ is magnetic permeability of the medium (H/m),
- ε is dielectric permittivity of the medium (F/m) ,

- v is velocity of an EM wave through the medium (m/s) (Annan, 2005).

Magnetic permeability is the degree to which a material generates a magnetic field in the presence of an inducing magnetic field. In most media, the magnetic permeability is approximately equal to the magnetic permeability of a vacuum ($\mu_0 = 1.257 \times 10^{-6}$ H/m; Walker, 2011), which means that the velocity of the EM wave is governed mainly by dielectric permittivity (Annan, 2005). Dividing the velocity of the EM wave through a medium by the velocity of an EM wave in a vacuum ($c = 0.2998$ m/ns; Walker, 2011) gives:

$$\frac{v}{c} = \frac{\sqrt{\mu_0 \varepsilon_0}}{\sqrt{\mu \varepsilon}} \approx \sqrt{\frac{\mu_0 \varepsilon_0}{\mu_0 \varepsilon}} = \sqrt{\frac{\varepsilon_0}{\varepsilon}} = \sqrt{\frac{1}{\kappa}} \tag{2.14}$$

Rearranging gives:

$$v \approx \frac{c}{\sqrt{\kappa}} \tag{2.15}$$

When a wave travels across an interface between materials with different permittivities, a portion of the energy is reflected back to surface (Everett, 2013). The amount of reflected energy is proportional to the square of the reflection coefficient, R, a measure of the amplitude of the reflected wave relative to the incident wave. For a wave travelling perpendicular to a dielectric boundary, the reflection coefficient is defined as:

$$R = \frac{\sqrt{\kappa_2} - \sqrt{\kappa_1}}{\sqrt{\kappa_2} + \sqrt{\kappa_1}} \tag{2.16}$$

Where κ_1 and κ_2 are the dielectric constants of the incident and refracting media, respectively (Everett, 2013). The amount of energy reflected is proportional to the square of the reflection coefficient. Equation 2.16 shows that as the contrast between the dielectric permittivity in the two materials increases the amplitude of the reflected wave also increases.

Therefore, the reduction in saturation associated with imbibition above or below a reflecting interface would lead to an increase in EM wave velocity and the amplitude of the signal returned to surface. This implies that when a wave travels through the zone of gas accumulation, it will travel faster, causing the event to arrive earlier at a higher amplitude and will be more readily visible in a radar section.

For instance, if an injected gas encounters a hydraulic boundary, it will accumulates below the interface and displace pore water. Here, the dielectric permittivity in the zone of accumulation (i.e., κ_2) will decrease. If the change in gas saturation decreases the difference in dielectric permittivity between the two materials, then less energy will be reflected; whereas if the difference increases as a result of the desaturation, more energy will be reflected from the interface.

2.3.2 Data Acquisition

GPR is a geophysical method that responds to changes in dielectric permittivity within the subsurface. During GPR data collection, an antenna generates a high-frequency EM wave which then propagates into the subsurface (Annan, 2005). When the EM wave encounters a dielectric permittivity boundary, a portion of the energy from the wave is reflected back to the surface and a portion is transmitted (Everett, 2013). A second antenna measures the amplitude of the reflected energy over time. Using the timing and amplitude of certain events, information on the dielectric permittivity distribution can be obtained and displayed as a radargram (i.e., an image of the energy returned to surface as a function of the position of the antennas and recording time). This section presents an overview of GPR; a comprehensive summary can be found in Annan (2009) and Knight (2001).

GPR is an application of Maxwell's Equations:

$$\nabla \times \vec{E} = -\frac{\partial \vec{B}}{\partial t} \tag{2.17}$$

$$\nabla \times \vec{H} = \vec{J} + \frac{\partial \vec{D}}{\partial t} \tag{2.18}$$

$$\nabla \cdot \vec{D} = q \tag{2.19}$$

$$\nabla \cdot \vec{B} = 0 \tag{2.20}$$

where:

- $\vec{E}$ is strength of the electric field (V/m),

- $\vec{B}$ is magnetic flux density vector (T),
- $\vec{H}$ is magnetic field intensity (A/m),
- $\vec{J}$ is electric current density (A/m^2),
- $\vec{D}$ is electric displacement (C/m),
- q is the electric charge density (C/m^3) (Annan, 2009).

and the constitutive relationships:

$$\vec{J} = \sigma \vec{E} \tag{2.21}$$
$$\vec{D} = \varepsilon \vec{E} \tag{2.22}$$
$$\vec{B} = \mu \vec{H} \tag{2.23}$$

where:

- μ is magnetic permeability (H/m),
- σ is electrical conductivity (S/m),
- ε is dielectric permittivity (F/m) (Annan, 2009).

Setting $\nabla \cdot \vec{J} = 0$ and eliminating $\vec{B}$ gives the vector damped wave equation for $\vec{E}$ (Everett, 2013):

$$\nabla^2 \vec{E} = \mu\sigma \frac{\partial \vec{E}}{\partial t} + \mu\varepsilon \frac{\partial^2 \vec{E}}{\partial t^2} \tag{2.24}$$

A similar equation can be found for $\vec{B}$ (Everett, 2013):

$$\nabla^2 \vec{B} = \mu\sigma \frac{\partial \vec{B}}{\partial t} + \mu\varepsilon \frac{\partial^2 \vec{B}}{\partial t^2} \tag{2.25}$$

If the displacement currents (i.e., $\mu\sigma \frac{\partial}{\partial t}$ term) of the generated EM field is significantly higher than the conduction currents (i.e., $\mu\varepsilon \frac{\partial^2}{\partial t^2}$ term), an EM pulse will propagate as a

wave (Annan, 2009). This condition holds for high frequency signals in poorly conductive soils. Typically, a nominal frequency between 1 MHz and 1000 MHz is used in GPR (Knight, 2001).

If the conductivity is sufficiently low, the generated electrical pulse will travel as a wave through the subsurface. When the generated wave encounters a contrast in dielectric permittivity, the energy is partitioned; a portion of the energy is transmitted across the boundary and a portion of the energy is reflected at the boundary.

Following the generation of the wave, a second antenna records the amplitude of incoming waves over a given time window (Annan, 2009). These waves are composed of the direct wave from the transmitter and reflected waves from energy partitioned at an interface. A single series of amplitude-time data collected at a location and single transmitter-receiver separation is called a trace. In order to suppress noise, multiple traces are collected at each position and averaged (Neal, 2004).

Collection of data occurs in two main ways: reflection surveys and common midpoint surveys (CMPs) (Everett, 2013). In a reflection survey, the transmitter and receiver are kept at a constant spacing and moved along a line, with readings taken at regular intervals. During a CMP, the transmitter and receiver begin at an initial separation and then the separation is increased with readings collected at regular intervals, with the two antennae maintaining the same midpoint.

The Fresnel zone defines the lateral resolvability of a target. Objects smaller than the Fresnel zone are seen as point diffractors whereas larger objects are reflectors (Annan, 2009). The radius of the Fresnel zone is given by:

$$r = \sqrt{\frac{\lambda_D^2}{16} + \frac{\lambda_D z}{2}} \tag{2.26}$$

where:

- r is the radius of the Fresnel zone (m),
- λ_D is the dominant wavelength of the generated pulse (m),

- z is the depth to the target (m) (Pearce & Mittleman, 2002).

In order to define the thickness of a layer, there must be a sufficient lag in reflection events from the top and bottom of the layer such that both responses can be separated. The smallest resolvable layer thickness is one quarter of the dominant wavelength of the EM pulse:

$$h_{min} = \frac{\lambda_D}{4} = \frac{v}{4f_D} \tag{2.27}$$

where:

- h_{min} is the minimum thickness of a resolvable structure (m),
- v is the velocity of the EM wave (m/s),
- f_D is the dominant frequency of the EM wave (Hz) (Neal, 2004).

2.4 Historical Geophysical Monitoring of Multi-phase Flow

Geophysical methods are routinely employed to detect and track immiscible fluid phases in the subsurface (e.g., Knight, 2001). Much of the foundational geophysical work on gas-phase migration in porous media can be traced back to a number of non-aqueous phase liquid release experiments (e.g., Andres & Canace, 1984; Daniels, Roberts, & Vendl, 1992; Stanfill & McMillan, 1985). While the majority of these applications deal with non-aqueous phase liquids, more recent studies have been devoted to the tracking of gas-phases (e.g., Comas et al., 2005; Doetsch, Fiandaca, Auken, Christiansen, & Cahill, 2015). Here, buoyancy-driven migration of free-gas in the subsurface is analogous to the density-driven migration of dense non-aqueous phase liquids (DNAPLs). Both density-driven DNAPL migration and buoyancy-driven free-phase gas migration travel vertically, albeit in opposite directions, until a barrier to vertical flow is encountered and the contaminant spreads laterally along the barrier until the pore pressure exceeds the entry pressure of the bounding porous material (Hwang, Endres, Piggott, & Parker, 2008).

2.4.1 Dense Non-Aqueous Phase Liquids

DNAPLs are any liquid phase contaminants denser than water and immiscible in water. DNAPLs travel vertically downward due to gravity until encountering a permeability boundary, which causes lateral spreading, often forming a pool along the capillary interface. D. A. Thomson (2004) released trichloromethane, trichloroethylene, and perchloroethylene (PCE) into a 2.5 m × 3.5 m × 3.3 m sheet pile cell at CFB Borden. Groundwater was allowed to flow under natural groundwater conditions through the cell for 40 months prior to the retrieval of 3 continuous cores from the site. These cores were analyzed for DNAPL concentrations and hydraulic conductivity. PCE was the only DNAPL that was present in the cores at the time of sampling. Free- and aqueous-phase DNAPLs were observed to be highest at or above lithologic boundaries. DNAPL spreading showed a strong correlation to the d_{10} (the grain size which 10% of the soil in a given sample is smaller than), implying that subtle geologic variations can have a strong effect on the migration of DNAPLs.

Brewster and Annan (1994) observed a release of PCE using GPR. 770 L of PCE was injected 60 cm below ground surface over 70 hours. Over a period of 41 days, GPR data was collected over a grid of 16 lines. The results from this study demonstrated that as the PCE pooled at a permeability boundary, the radar reflectivity from the boundary varied temporally, providing a means of monitoring accumulation and lateral movement of the PCE over time (Brewster et al., 1995). Although they were unable to detect the vertical migration pathways directly with GPR data, using the geology interpreted from the background GPR data and the GPR imaged zones of contaminant accumulation, an approximation of the location of the vertical migration pathways could be inferred.

2.4.2 Air Sparging

Air sparging is a remediation technique wherein air is injected directly into the subsurface to fuel aerobic degradation of organic contaminants (Bass, Hastings, & Brown, 2000). Knowledge of the distribution of the gas during this process is important in assessing the efficacy of the remediation process. Geophysical techniques have been used as a non-invasive tool to track the movement of the gas in the formation over time.

N. R. Thomson and Johnson (2000) reviewed a number of mathematical air sparging models and found that in homogeneous and isotropic models gas tended to spread parabolically,

the gas plume remaining narrow near the injector and widened as it travelled to the surface. As heterogeneity was introduced gas still spread parabolically; however, saturations within the gas impacted zone became more variable. As anisotropy was introduced, zones of increased desaturation formed which tended to extend horizontally while remaining vertically thin. Throughout all of these models, desaturation still occurred in a recognizably parabolic shape, although with variable degrees of gas saturation within that parabola. While modelling can provide information on the macroscopic distribution of gas in the subsurface, a site would need to be characterized on a scale less than 0.1 m in order to produce a model capable of predicting the distribution of gas within a sparging project (N. R. Thomson & Johnson, 2000).

Tomlinson, Thomson, Johnson, and Redman (2003) used GPR, neutron logging and piezometric measurements, to monitor the distribution of air during a sparging event within an unconfined shallow sandy aquifer at CFB Borden, Canada. Pressurized air was injected at a single location 3 m below the water table for 7 days at a rate of 200 m^3/day. Borehole GPR noted an increase in wave velocity between boreholes while surface GPR noted an increase in reflectivity in zones of gas accumulation. Both of these responses indicate localized desaturation around the injection point and down-gradient along stratigraphic boundaries, which was consistent with the water saturation data obtained via neutron logging. Based on the GPR, gas saturations within the aquifer reached 15% to 60% within a radius of approximately 2.5 m from the sparging screen. Dissolved oxygen and hydraulic pressure measurements indicated migration as far as 6 m away from the air injection well; however, surface GPR measurements indicated that the gas had migrated beyond the groundwater monitoring network.

Lundegard and LaBrecque (1998) used cross hole ERT to monitor the performance of air sparging at two sites impacted by gasoline contamination. At Site A, the air was injected at 9.5 m below ground surface (bgs) (approximately 4.3 m below the water table) into a weakly heterogeneous aquifer; and, at Site B, the air was injected at a depth of 9.0 m bgs (approximately 3.7 m below the water table) in a strongly heterogeneous aquifer. In the case of a homogeneous aquifer, ERT showed that buoyant forces caused air to migrate vertically, while maintaining a sharp boundary between saturated and desaturated zones. In the case of a heterogeneous aquifer, air exhibited higher lateral mobility and was accompanied by slight desaturations along permeability transitions.

These studies demonstrate the importance of subtle changes in hydraulic property and geometry of sedimentary layers on the distribution and movement of gas phases in the

subsurface.

2.4.3 Free-Phase Carbon Dioxide

A number of experiments have been conducted to examine the migration and geochemical alterations caused by CO_2 during carbon capture and storage (CCS) using a variety of geophysical methods including seismic (Lumley, 2010), ERT (Doetsch et al., 2015), GPR (Lassen, Sonnenborg, Jensen, & Looms, 2015), as well as others (e.g., Gasperikova & Hoversten, 2006, 2008). CCS is a process in which CO_2 is injected into deep reservoirs as a liquid or supercritical fluid to mitigate the build-up of greenhouse gasses in the atmosphere (Kovacs, Poulussen, & de Dios, 2015). Geophysics is commonly employed to determine the distribution of the injected CO_2 in the subsurface. Generally, research shows that the imbibition of free-phase gas and alterations to the geochemical properties of the pore water associated with CO_2 injection are detectable using geophysical methods.

Lassen et al. (2015) monitored the movement of injected gas-phase CO_2 using cross borehole GPR. Four tests, each lasting two days, were performed, during which between 18.9 kg and 45 kg of free-phase CO_2 was injected approximately 8 m below the water table. Borehole GPR data was collected in two different modes, zero offset profiles and multiple offset gathers at multiple times during each injection event. As more CO_2 was introduced to the subsurface the wave velocity through the soil increased. The gas formed pockets within the saturated media causing the water content to decrease through imbibition (Kim, Nam, & Matsuoka, 2013). Slight variations in the water content in turn caused variations in the electromagnetic wave velocity (Annan, 2005). The gas was observed to travel vertically under buoyancy conditions until it reached a permeability barrier, at which point it travelled laterally away from the source (Lassen et al., 2015). Here, gas saturation was inferred using changes in the electromagnetic velocity of a GPR signal. Using the inferred gas saturations, Lassen et al. (2015) estimated the total volume of gas, but their estimates only accounted for 30% to 40% of the total volume of injected gas. Once the injection was turned off, the CO_2 began to dissolve into the groundwater and within two days, the bulk of the gas-phase CO_2 had either dissolved or migrated outside the study area. This dissolution, coupled with migration outside the study area, makes delineation of CO_2 plumes virtually impossible using GPR.

Doetsch et al. (2015) used ERT to monitor an injection of CO_2 into a shallow aquifer. Gas-phase CO_2 was injected at 12 L/min for 14 days, after which the injection rate was

lowered to 6 L/min for 58 days. The gas was injected at two depths in the aquifer, one injection well was screened from 4 m to 5 m bgs, and the other was screened from 9 m to 10 m bgs. A decrease in the electrical resistivity was observed in the region of the injected CO_2, which returned to baseline conditions following the cessation of the gas injection. Electrical conductivity of the pore water and concentrations of aluminum from geochemical reactions between the dissolved CO_2 and the soil indicated that no gas-phase CO_2 was present in the groundwater at the end of the experiment. The observed decrease in resistivity was attributed to two factors: the first was through the addition of free ions caused by the dissolution of CO_2 into the groundwater, and the second was the geochemical alteration of the grain surfaces formed by the acidification of the groundwater. While Doetsch et al. (2015) demonstrated the abilities of geophysical methods to qualitatively track the migration of dissolved CO_2, they also demonstrated the complexities associated with hydrogeological interpretation of geophysical data.

2.4.4 Gas-Phase Methane

The geophysical response associated with methane gas has focussed primarily on biogenic, non-point sources, such as peat bogs (e.g., Comas & Slater, 2007; Comas et al., 2005; Slater, Comas, Ntarlagiannis, & Moulik, 2007) and landfills (e.g., Johansson, Rosqvist, Svensson, Dahlin, & Leroux, 2011; Rosqvist et al., 2011). Here, methane arises from the decomposition of large volumes of organic matter in a largely anaerobic environment. In all of the studies, the location of the methane was determined by sensing changes in formation saturation, owing to pore water displacement by the gas-phase. This change in fluid-phase alters the dielectric permittivity and electrical resistivity of the bulk formation (Chen & Slater, 2015; Slater et al., 2007).

Comas et al. (2005) used surface and borehole GPR supplemented with moisture probe data to observe the migration of biogenic peat in a peatland, drawing three conclusions from their observations. Firstly, surface GPR produced signal scattering in specific zones that correlated with desaturation observed via moisture probe data. Secondly, borehole GPR showed that electromagnetic waves travelled faster in zones of gas accumulation, consistent with a localized desaturation caused by the presence of a free-phase contaminant. Finally, the zones of GPR signal scattering were often underneath strong reflectors, correlating with macroscopic structures that controlled the migration of methane and provide a hydraulic permeability contrast that would entrap gas. These conclusions presented a

means of defining the movement and distribution of free-phase gas.

Slater et al. (2007) used electrical resistivity to monitor free methane gas production within a 28 cm × 21 cm × 21 cm ex-situ block of peat. Five vertical electrode arrays, positioned at the centimetre-scale were used to measure the electrical resistivity of the block over a 48 day period. Surface deformation of the block was measured and used to account for porosity changes in the peat, while gas flux over the surface was monitored. Near the upper surface of the block, the resistivities consistently increased at all of the measuring points. After approximately 55 days, further increase in the resistivity was noted, which is consistent with the highly resistive, free-phase gas replacing the conductive water from the sample volume; however, not all of the measuring points experienced the same increase.

Comas and Slater (2007) monitored the dielectric properties within a 22 cm × 32 cm × 31 cm ex-situ peat block, instrumented with elevation rods and a methane flux meter to measure surface deformation and gas flux, respectively. Using a 1.2 GHz GPR system, the two-way traveltime was measured along three transects and three vertical lines during an eight day period of heating the peat block, followed by an extended period at a constant temperature. The dielectric permittivity was calculated from the two-way traveltime and the thickness of the block. Using a petrophysical relationship between dielectric permittivity (i.e., electromagnetic wave velocity) and water content, the gas content over the monitoring period was determined. The computed gas content values were consistent with the gas saturations inferred from the surface deformation and gas flux measurements. Gas ebullition appeared periodically, in a manner consistent with a build-up of gas until it reached a critical pressure, at which point it released the gas. The timing of these release events corresponded with atmospheric pressure data, with decreases in atmospheric pressure aligning with a release of methane from the block.

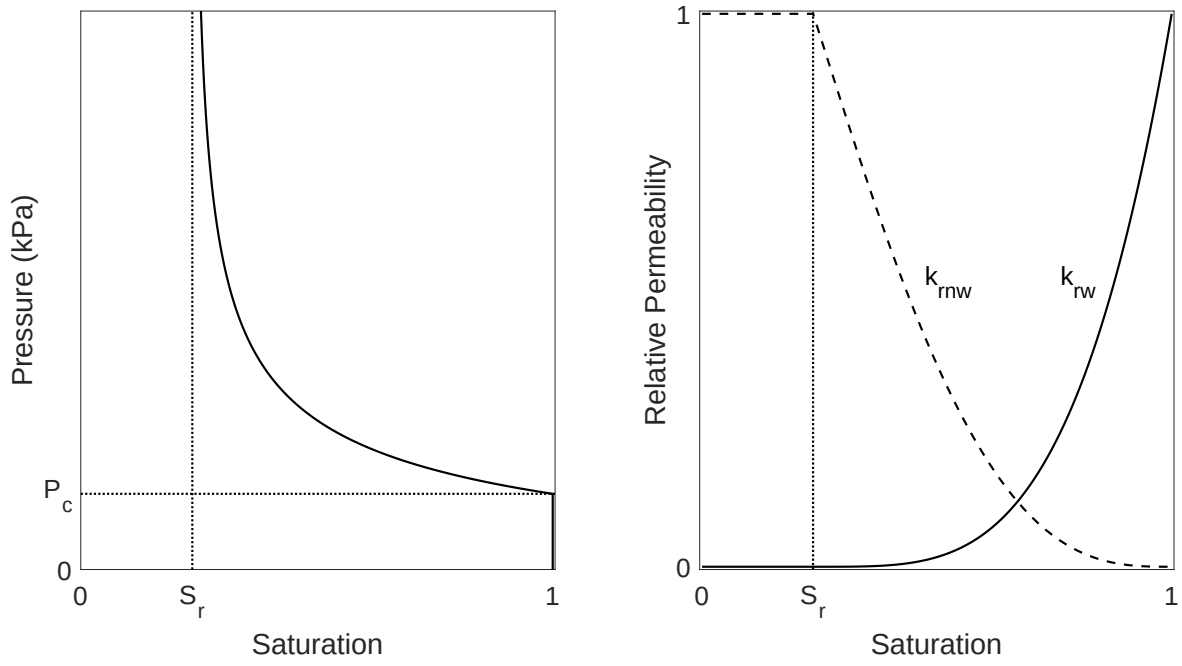

(a) Pressure-Saturation Curve

(b) Saturation-Relative Permeability Curve

Figure 2.1: Brooks-Corey Model (Brooks & Corey, 1964) relating saturation to (a) the capillary pressure (0 kPa represents the water table) and (b) relative permeability of the wetting (k_{rw}) and non-wetting (k_{rnw}) phases. The entry pressure is marked by P_c and the residual saturation is marked by S_r.

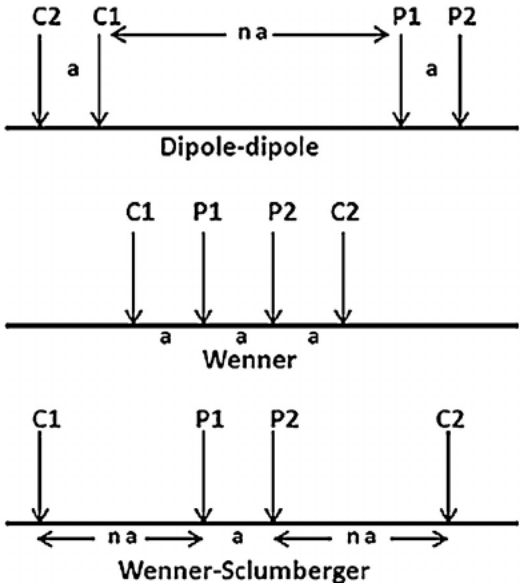

Figure 2.2: Illustrations of common arrays used in the acquisition of ERT data (*from* Ain-Lhout et al., 2015)

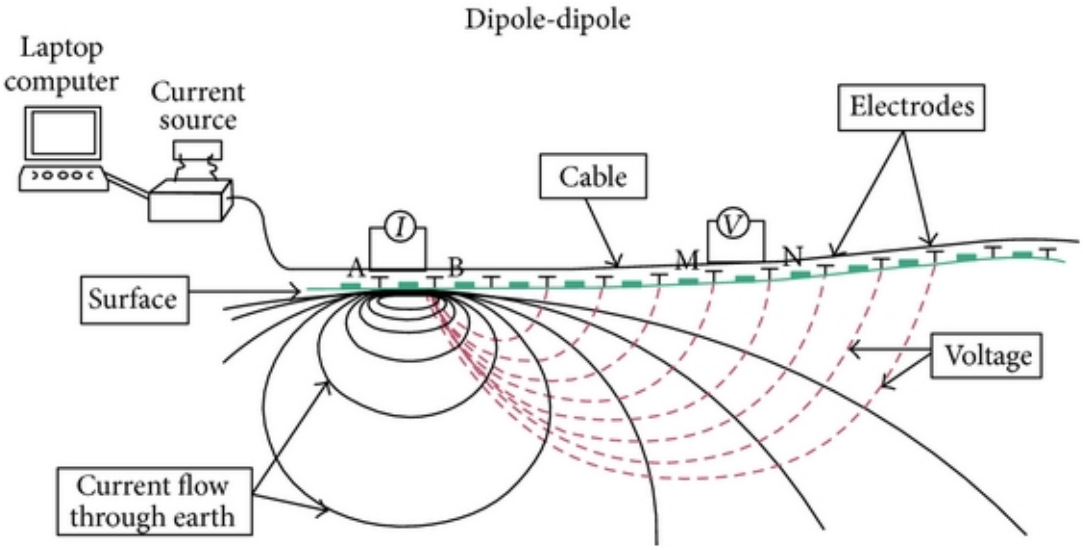

Figure 2.3: Diagram of current flow paths (black lines) and equipotential surfaces of voltage (red lines) in a dipole-dipole survey (*from* Okpoli, 2013).

Table 2.1: Values of electrical conductivity and resistivity for common geologic materials (*after* Everett, 2013)

Material	Electrical Conductivity (mS/m)	Electrical Resistivity (Ω·m)
Clay	50 – 1000	1 – 20
Sand (wet – moist)	5 – 50	20 – 200
Shale	2 – 1000	1 – 500
Limestone	10^{-3} – 10	10^{2} – 10^{6}
Metamorphic rocks	10^{-3} – 20	50 – 10^{6}
Igneous rocks	10^{-3} – 10	10^{2} – 10^{6}

Table 2.2: Values of Dielectric Permittivity for Common Geologic Materials, (*after* Davis & Annan, 1989)

Material	Dielectric Permittivity
Air	1
Fresh Water	78.5 (25 °C) – 86.1 (5 °C)
Dry sand	3 – 5
Saturated sand	20 – 30
Clays	5 – 40
Limestone	4 – 8
Shales	5 – 30
Granite	4 – 6

Chapter 3

Methodology

This project used modelling to explore the effects of different hydrogeologic parameters on the flow of methane through the saturated subsurface and the associated geophysical response. This objective was achieved by first using CompFlowBio (Cfbio) (Unger et al., 1995) to model the distribution of methane in the subsurface. The results from different times of the methane flow models were then used to generate distributions of geophysical properties; namely dielectric permittivity and electrical resistivity. Forward models of ground-penetrating radar (GPR) and electrical resistivity tomography (ERT) were generated based on these distributions using ReflexW's modelling package (Sandmeier, 2017) and Res2DMod (Loke, 2002), respectively. Figure 3.1 shows a flow chart, demonstrating the overall work flow of the modelling aspects of this project.

3.1 Multi-Phase Flow

3.1.1 CompFlowBio

Cfbio, the code used to complete the methane flow modelling, uses a first-order accurate, finite-volume formulation to solve a series of differential equations for the conservation of contaminant, water, and air (Unger et al., 1995; Walton, 2013). A full treatment can be found in Unger et al. (1995).

3.1.2 Basic Case

Modelling began with the definition of a basic case, informed by data retrieved during the Borden Methane Injection (BMI) Experiment at the CFB Borden Research Site (outlined in Table 3.1). Three cores were retrieved from the site. The results of the grain size analysis and permeameter testing of one of the cores (Figure 3.2) revealed a four layer system (Steelman et al., 2017). The first three layers were dominated by fine sands with high permeabilities ($k \approx 3 \times 10^{-12}$ m^2). The second layer had a higher percentage of coarse sands, pebbles, silts and sands, and a permeability approximately one order of magnitude lower than the first and third layers. The fourth layer, beginning at a depth of approximately 7.4 m, represents the aquitard. A higher percentage of silts and clays with low permeability ($k \approx 6 \times 10^{-14}$ m^2) was observed in layer 4.

The basic scenario consists of an unconfined aquifer over an aquitard. The first layer was an amalgamation of the upper three layers with a lateral permeability (k_h) of 2.2×10^{-12} m^2 and a porosity (ϕ) of 0.33, the average of the values for those parameters in the recovered core. The second layer represented the aquitard, $k_h = 6.4 \times 10^{-14}$ m^2 and $\phi = 0.39$. The lateral permeability was determined by taking the geometric average of the permeabilities of samples in the lower layer. Soil compaction and vibration of the core resulted in highly variable, and thus unreliable estimates of porosity. Therefore, literature values for porosity of the Borden sand were used in these models (Das, 2008). The boundary between the aquitard and the aquifer was set at 9.0 m bgs; both the aquifer and aquitard had an anisotropy ratio of $k_h/k_v = 10$.

The boundary conditions were set to maintain a 1.0 m depth to the water table directly above the injectors with an average linear groundwater velocity of 6 cm/day in the aquifer; the pressure was defined at the lower two corners of the model domain, creating a horizontal hydraulic gradient of 0.0106 m/m with a constant head boundary along the base and along the right and left sides of the domain. The upper boundary, representing the atmosphere, was defined by a pressure of 100 kPa and given a constant recharge rate of 0.7 mm/day. At initialization, the model was fully saturated below a depth of 0.7 m bgs and was 60% saturated above 0.7 m bgs. The model was run for 100 days prior to the start of the injection to allow it to come to a steady state flow condition.

The relative permeability was interpolated from a table of relative permeability values (Table 3.2). This table was constructed using the Brooks-Corey parameters from Kueper and Frind (1991): an entry pressure (P_c) of 2.22 kPa, residual saturation ($\theta_{w,r}$) of 0.078, and a

pore size distribution index (λ) of 2.48. A residual gas saturation of 10% was assumed.

The injector geometry was modelled after the actual injector geometry employed in the BMI Experiment (Cahill et al., 2017). Gas injectors were placed at 4.5 m and 9.0 m bgs, 8 m from the upgradient boundary. A four stage, stepped injection rate was used: a slow injection rate (Phase I: 2 × 0.06 L/min), a moderate injection rate (Phase II: 2 × 0.35 L/min), a moderate injection from the deeper well only (Phase III: 1 × 0.35 L/min), and a fast injection (Phase IV: 2 × 1.5 L/min). The injection schedule is presented in Table 3.3 (Cahill et al., 2017). Also during the BMI Experiment, a power outage resulted in the shut off of the injectors during Phase II between Days 38 – 44; the shut off was included in the simulated injection history schedule. The injectors were modelled as point sources during Phases I – III; distributed injectors were used during Phase IV to account for the high volume of gas being added to the system and ensure model stability. The distributed injectors were 0.3 m tall and 0.2 m wide with their base centred on the location of the previous point source injectors.

3.1.3 Model Parametrization

Multiple model domain dimensions were tested to evaluate potential boundary effects on the simulations: 5 m × 10 m, 20 m × 10 m and 30 m × 10 m. A model width of 20 m provided an adequate balance of model accuracy and computation time, and thus, was used for all subsequent simulations. A depth of 10 m was used as a negligible response was expected 1 m below the top of the aquitard. The model was discretized in a 10 cm × 10 cm grid. The convergence tolerances for the majority of the model time were 1.0×10^{-4} kPa for pressure, 1.0×10^{-5} for saturation, 1.0×10^{-7} for the mole fraction of methane, and 1.0×10^{-2} K for temperature. During Phase IV, the increased injection rate made it difficult for Cfbio to converge, so the tolerances were lowered to allow for the successful completion of the simulations; here the tolerances were changed to 5.0×10^{-3} kPa for pressure, 5.0×10^{-4} for saturation, 5.0×10^{-6} for the mole fraction of methane, and 5.0×10^{-2} K for temperature.

3.1.4 Modelled Scenarios

Following the definition of the basic case, a number of modifications were applied to investigate the impacts of varying hydraulic parameters and geometries on the migration of free-phase methane. This objective was achieved by changing the values of one of the parameters used to define the basic model, adding a structure, or a combination of these changes. Results from the various cases of each scenario were compared to investigate the impacts of model parametrization on the flow of the free-phase methane. Table 3.4 provides an overview of the individual cases for each model scenario.

Heterogeneity

Two scenarios were used to investigate the impact of heterogeneity, specifically the addition of macroscopic, continuous layers, in the subsurface. The first scenario compared a uniform aquifer (i.e., the base case) to an aquifer containing a layer from 3.0 m – 3.5 m bgs, with a horizontal permeability of $k = 5.1 \times 10^{-13}$ m^2 and $\phi = 0.31$. The hydraulic properties for the layer were based on values obtained from the core collected at the injection site (Steelman et al., 2017). In this scenario, the entry pressure of the layer was the same as the entry pressure of the aquifer. The second scenario investigated the impact of varying layer permeability. A layer was added from 3.0 m – 3.5 m bgs with $\phi = 0.33$. A range of permeability contrasts were considered to relate the permeability of the layer, k_L, to the permeability of the aquifer, $k_{aq} = 2.2 \times 10^{-12}$ m^2: $k_L = 1 \times k_{aq}$, $k_L = 0.55 \times k_{aq}$, $k_L = 0.3 \times k_{aq}$, $k_L = 0.1 \times k_{aq}$, and $k_L = 0.03 \times k_{aq}$. The entry pressure and porosity of the soil in the layer were kept at the same values as in the aquifer: $P_c = 2.22$ kPa and $\phi = 0.33$, respectively.

Anisotropy

To assess the impact of anisotropy on the flow of methane the basic case was modified using a range of anisotropy ratios. The horizontal hydraulic permeability of the aquifer and aquitard were fixed, having the same value as in the basic case, while the vertical hydraulic permeability was adjusted to create the desired anisotropy ratio. The following anisotropy ratios were considered: k_h/k_v =5, k_h/k_v =10, and k_h/k_v =30. These three cases were then repeated with a layer added within the aquifer from 3.0 m – 3.5 m bgs, with $k_L = 0.1 \times k_{aq}$ and $\phi = 0.33$.

Groundwater Velocity

One scenario was used to examine the impact of groundwater velocity on the flow of methane, the basic case was run with a range of different boundary pressure conditions to produce the desired groundwater flow velocity across the model domain while maintaining a fixed depth of 1.0 m to the water table. The aquifer permeability was $k_{aq} = 2.2 \times 10^{-12}$ m^2 and $\phi = 0.33$ with an anisotropy ratio of k_h/k_v =10. Four different groundwater velocities were modelled: 0 cm/day, 3 cm/day, 6 cm/day, and 10 cm/day. These flow rates corresponded to horizontal hydraulic gradients of 0 m/m, 0.00449 m/m, 0.0106 m/m, and 0.0177 m/m, respectively.

Layer Thickness

One scenario was used to assess the impact of the layer thickness on the flow of free-phase methane, a layer with $k = 5.1 \times 10^{-13}$ m^2 and $\phi = 0.31$ was added to the subsurface. The top of the layer was maintained at a depth of 3.0 m bgs while the depth to the base of the layer was adjusted to give the desired layer thickness. Three layer thicknesses were considered: 0.2 m, 0.5 m, and 1.0 m.

Entry Pressure

The impact of entry pressure on the flow of methane gas was assessed through two scenarios. In the first scenario a layer from 3.0 m – 3.5 m bgs was added to the basic case with $k_L = 0.55 \times k_{aq}$ and $\phi = 0.33$. This was modelled twice, once with layer entry pressure equal to the aquifer (i.e., $P_c = 2.22$ kPa) and once with the entry pressure of the layer increased to $P_c = 2.99$ kPa (following Leverett, 1940). A new relative permeability table was generated using the modified entry pressure at the saturation values shown in Table 3.2.

The second scenario compared two cases of a layer with $k = 5.1 \times 10^{-13}$ m^2 and $\phi = 0.31$, depicting values from the core sample. This aquifer geometry was modelled twice, once with the layer having the same entry pressure as the aquifer (i.e., $P_c = 2.22$ kPa) and once with the layer having an entry pressure of $P_c = 2.99$ kPa.

Layer Discontinuities

Two scenarios were modelled to evaluate the role of layer discontinuities on the evolution of a methane gas plume. A single layer was added to the basic case from a depth of 3.0 m – 3.5 m with $k = 5.1 \times 10^{-13}$ m^2 and $\phi = 0.31$ and was continuous across the model domain, with the exception of a 1.0 m window in the added layer; the hydraulic properties of the window were equal to those of the aquifer. Three different cases were simulated with the window centred at -1.5 m, 2.5 m, and 6.5 m downgradient of the injectors. The second scenario consisted of the same three scenarios only with the entry pressure within the layer increased to $P_c = 2.99$ kPa.

Injection History

To assess the impact of injection history on the flow of methane gas two different scenarios were considered. The first scenario consisted of fixed injection rates for the full 72 days at each of the three rates used in the actual actual experiment: Phases I (0.06 L/min), II (0.35 L/min), and IV (1.50 L/min). These cases were repeated with the addition of a layer from 3.0 m – 3.5 m, with $k_L = 2.2 \times 10^{-13}$ m^2 and $\phi = 0.33$.

The second scenario was comprised of the basic case with the actual injection rate history. Three different cases were modelled, one which used only the deep injector, one that used only the shallow injector, and one that used both the deep and shallow injectors. The same set of hydraulic properties were used in each scenario.

3.1.5 Model Evaluation Criteria

Following the simulation of each case, a contour plot was generated which showed the change in gas saturation across the model domain at key times during the injection period. For most cases, Day 56 was considered as it corresponded with a peak in total dissolved gas pressure during the BMI Experiment (Steelman et al., 2017). Contour snapshots were accompanied by the total volume of gas within the model domain over time. This quantity was computed by using the volume of gas that was injected and subtracting the amount that exited through the atmosphere, and the inflow and outflow boundaries. Qualitative observations concerning the impact of model parameters on the movement of methane

within the subsurface were made by comparing the spatial distribution of methane at given times with gas retention time-series over the full injection period.

3.2 Electrical Resistivity Tomography

3.2.1 Res2DMod

Res2DMod (version 3.01) was used in this study to model the ERT response to gas migration in the aquifer. Res2DMod uses a finite-difference formulation to solve Ohm's Law and a conservation of charge (Dey & Morrison, 1976; Loke, 2002). A full treatment can be found in Loke (2002).

3.2.2 Scenario Selection

Four cases were used to generate forward models for ERT: the homogeneous case ($k_{aq} = 2.2 \times 10^{-12}$ m^2 and $\phi = 0.33$); a single layer with no entry pressure change ($k_L = 5.1 \times 10^{-13}$ m^2; $\phi = 0.31$, and $P_c = 2.22$ kPa); a single layer with an entry pressure contrast with the aquifer ($k_L = 5.1 \times 10^{-13}$ m^2, $\phi = 0.31$, and $P_c = 2.99$ kPa); and the case of a layer with an entry pressure change with a 1 m discontinuity centred 2.5 m down-gradient from the injector ($k_L = 5.1 \times 10^{-13}$ m^2, $\phi = 0.31$, and $P_c = 2.99$ kPa).

3.2.3 Model Parametrization and Discretization

The Matlab script for converting the groundwater flow models to ERT models is available in Appendix A.

The hydrological models for select days (namely Days 0, 1, 20, 37, 56, 71, 102) were selected to generate an equivalent electrical resistivity distribution of the subsurface. For each day that was simulated, the model was discretized using 29 rows of blocks which increased geometrically in size with depth, such that at surface the blocks were 0.1 m tall and the deepest blocks were 0.8 m tall. Each block was 0.25 m wide. The total domain

of the ERT model ran from 23 m upgradient of the injectors to 24 m downgradient of the injectors and went from surface to a depth of 10 m bgs. The saturation values of each block were determined by averaging the saturations from the flow model cells within each block of the ERT model, as was porosity. A portion of the modelled zone in the ERT extended outside of the domain of the groundwater flow model. To determine the saturation and porosity of the cells in these regions, the saturation and porosity values on the edges of the groundwater flow model were extended beyond to the edge of the ERT model domain. In cases where the gas-phase reached the edge of the flow model domain (i.e., late-time, high injection rates), the saturations used to generate the geophysical model beyond the flow model domain will likely not be representative of the actual gas distribution.

Archie's Law (Equation 2.7; Archie, 1942) and the relationship of conductivity to resistivity ($\rho = {}^{1}/_{\sigma}$) were used to determine the resistivity of each cell of the ERT model. The empirical parameters and resistivity of water used were: $a = 1$ (Archie, 1942), $m = 1.3$ (Doveton, 1986), $n = 1.6$ (Mickle, 2005), and $\rho_W = {}^{1}/_{0.0482\ \mathrm{S/m}} = 20.75\ \Omega\mathrm{m}$ (Cahill et al., 2017). For this study, it is assumed that injected gas will displace the pore fluid, causing a reduction in the water saturation and remain relatively insoluble during the injection period, thus conductivity of the pore water should remain stable (Kaye & Laby, 1995). This relative insolubility implies that the saturation term is the only term in Equation 2.7 that changes during the injection period.

Once these values were determined all of the resistivity values were grouped into sixteen distinct values using k-means clustering (The MathWorks, 2010) and the distribution of these values was saved in a format readable by Res2DMod. Sixteen resistivity values represent the maximum number of resistivity units that can be modelled using this program.

Using Res2DMod a 48 electrode dipole-dipole survey with an electrode spacing of 1.0 m was simulated, during which 32 different electrode spacings were used. 3% noise was added to the apparent resistivity values from the forward modelled data.

3.2.4 Model Evaluation Criteria

Following the forward modelling process, the output of the resistivity model was inverted using Res2DInv (Geotomo Software, Malaysia) to obtain a possible resistivity distribution that would give the ERT response. Each cell (ignoring cells with resistivity drops) of the

inverted model was converted to a change in saturation using Archie's Equation (Archie, 1942). The original gas saturation used to generate the model, the inverted resistivities, and the calculated gas saturation were then plotted together. The vadose zone response was often very large, so data shallower than 1 m was muted.

3.3 Ground-Penetrating Radar

3.3.1 ReflexW

ReflexW (Version 8.2.2) was used in this study to model the forward GPR response. ReflexW uses a finite-difference formulation to solve Maxwell's Equations (Sandmeier, 2017). A full treatment of the software is available from Sandmeier (2017).

3.3.2 Scenario Selection

Four scenarios, corresponding to the models selected for ERT modelling, were used to generate the GPR simulations representing different levels of complexity in aquifer properties explored in the gas-phase flow modelling. These models were the case of the homogeneous case ($k_{aq} = 2.2 \times 10^{-12}$ m^2 and $\phi = 0.33$); a single layer with no air-entry pressure change ($k_L = 5.1 \times 10^{-13}$ m^2, $\phi = 0.31$, and $P_c = 2.22$ kPa); a single layer with an air-entry pressure contrast with the aquifer ($k_L = 5.1 \times 10^{-13}$ m^2, $\phi = 0.31$, and $P_c = 2.99$ kPa); and a layer with an air-entry pressure change with a 1 m discontinuity centred 2.5 m downgradient of the injectors ($k_L = 5.1 \times 10^{-13}$ m^2, $\phi = 0.31$, and $P_c = 2.99$ kPa).

3.3.3 Model Parametrization and Discretization

The Matlab scripts for converting the groundwater flow models to GPR models is available in Appendix A.

For each scenario at each day the gas distribution was used to determine the dielectric permittivity (κ) and conductivity (σ); these values were calculated using the CRIM formula 2.12 for each node in the groundwater flow model. Each cell was considered to have

three components: the solids, pore water, and gases (i.e., air and methane). Literature values were used to determine the κ values for each components; solids were assumed to be quartz grains ($\kappa = 4.2$; Keller, 1987) and gases were assumed to be comparable to a vacuum ($\kappa = 1$; Everett, 2013). Using a groundwater termperature of 10 °C (Steelman et al., 2017) the dielectric permitivitty of water was calculated to be $\kappa = 84.9$ (Roth et al., 1990). The volumetric components were determined using the porosity and simulated water saturations. Similarly, σ was determined using Archie's Equation (Equation 2.7; Archie, 1942). The values for the empirical parameters and the conductivity of water were taken from literature; $a = 1$ (Archie, 1942), $m = 1.3$ (Doveton, 1986), $n = 1.6$ (Mickle, 2005), and $\sigma_W = 0.0482$ S/m (Cahill et al., 2017). The κ and σ values were considered to be point measurements taken at the center of the node.

Two different models were calculated for each of the four selected cases. Firstly, full GPR profiles were computed for specific days of the simulation period (i.e., Days 0, 20, 37, 56, 71, and 102). In these models, a GPR trace response was recorded every 10 cm, beginning with the transmitter and receiver centred at -6 m and ending with the receiver centred at 10 m resulting in a 16 m long profile centred over the 20 m $\times$ 10 m flow model domain. The second set of models only considered a select number of positions (i.e., -1.5 m, 2.5 m, 6.5 m relative to the position of the injectors); however, for these cases a forward GPR response was computed for each day of the simulated period.

The modelling used a point source generating a 200 MHz Ricker wavelet. The GPR response was measure with a time step of 0.1 ns for a total time window of 300 ns with a fixed 0.5 m antenna separation. Excitation and registration occurred normal to the survey line (representing a typical antenna configuration in the field) utilizing linear absorbing boundaries along the edges of the model domain to reduce boundary effects. The model was discretized on a 0.025 m grid, linearly interpolating κ and σ between points.

3.3.4 Model Evaluation Criteria

For each trace (Figure 3.4a), a gain function was applied to account for signal attenuation. Subsequently, a bandpass filter was applied to each trace to remove high frequency noise (Figure 3.4b). The envelope of the GPR amplitude was calculated for each time-lapse trace to determine changes in the amount of energy reflected to surface (Figure 3.4c) relative to background conditions (e.g., Day 0).

GPR traces were assembled into either reflection profiles (i.e., a two dimensional snapshot of the flow model domain on a given day) or time-lapse sections (a time series plot of a single GPR trace over the entire injection period , e.g., Figure 3.4d); the normalized enveloped amplitude of the GPR plot was computed for all models.In addition, the sum of the enveloped amplitude between 50 ns and 150 ns was calculated to evaluate relative changes in reflected energy over the course of the injection period at different positions within the aquifer; these two-way traveltimes correspond to depths of 1.5 m bgs to 4.5 m bgs assuming a constant EM wave velocity of 0.06 m/ns. The normalized integrated amplitude data were plotted for three trace locations across the flow model domain over the simulated flow period.

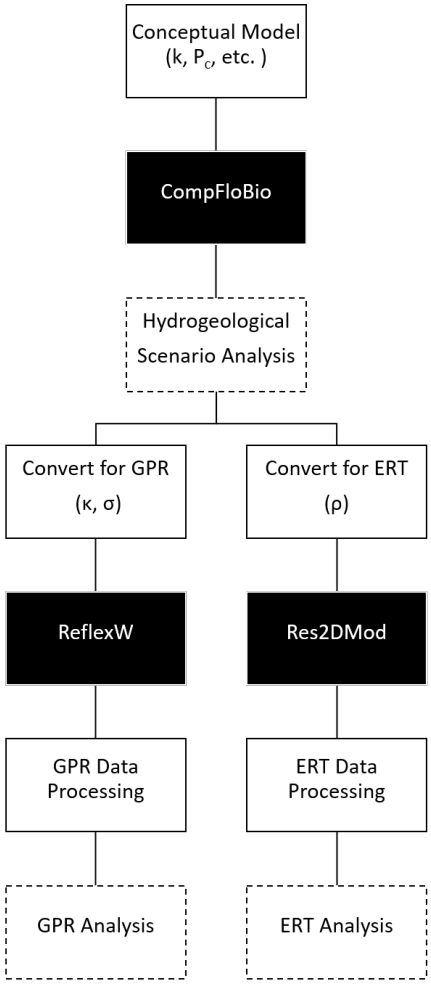

Figure 3.1: Flow chart outlining the series of models used to investigate the impact of hydraulic parameters and flow system conditions on gas migration and associated geophysical responses.

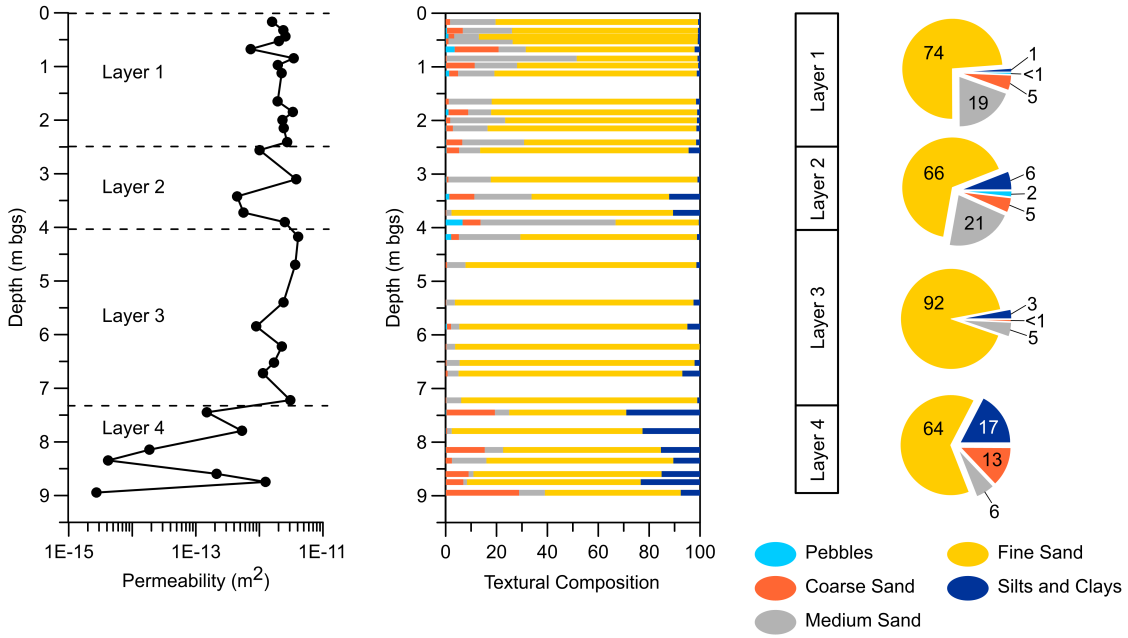

Figure 3.2: Results from falling head permeameter and grain size analysis testing from a core taken from the Borden Test Site. Layers represent units of the core with similar textural and hydrogeologic parameters (*from* Steelman et al., 2017).

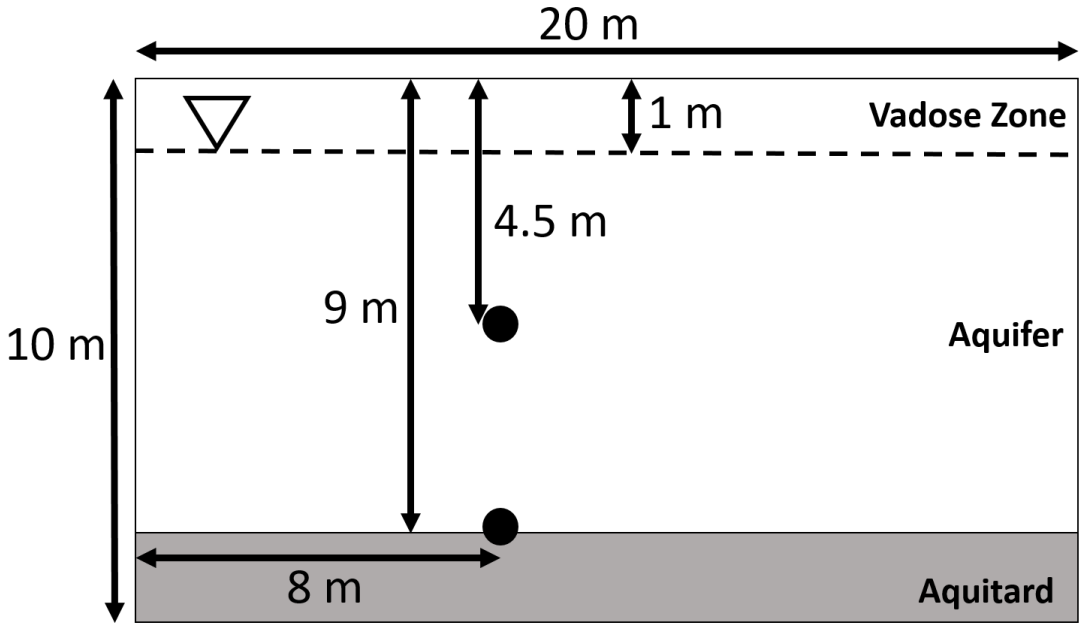

Figure 3.3: Geometry of the basic case consisting of a uniform aquifer overlying an aquitard with two injectors within the aquifer.

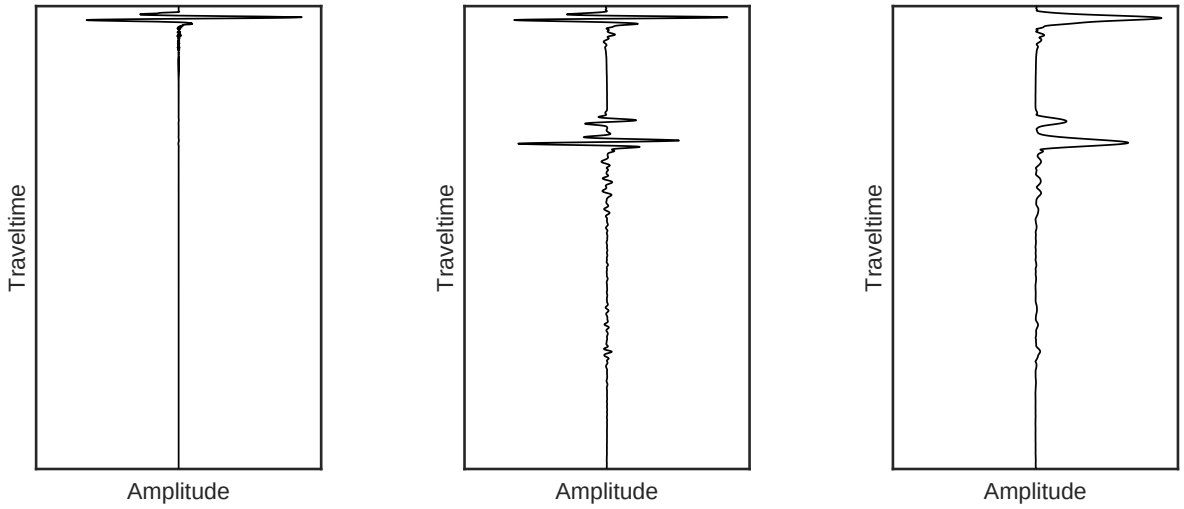

(a) Raw trace

(b) Trace with gain and bandpass filter applied

(c) Enveloped energy of trace

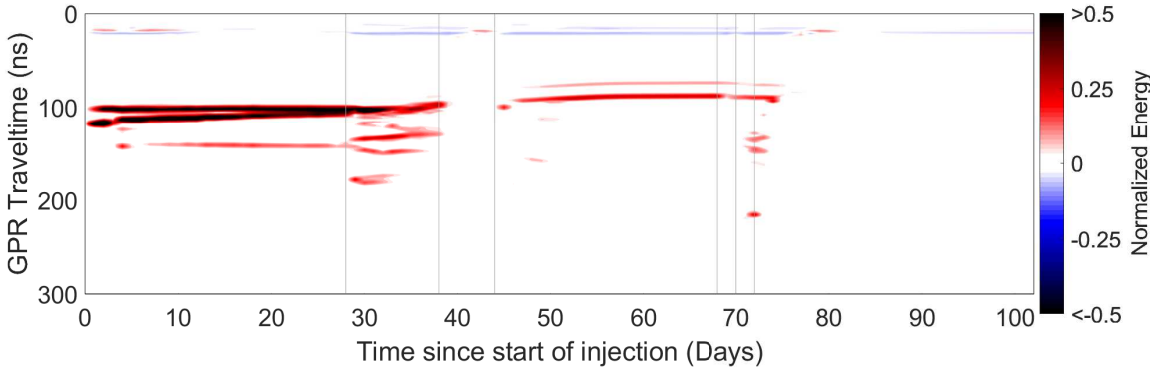

(d) Compiled time-lapse plot

Figure 3.4: GPR data processing procedure. After a raw trace is modelled (e.g., a) it has a gain and bandpass filter applied to compensate for signal attenuation, divergence, and high frequency noise associate with signal scattering (b). For time-lapse models the envelope of the energy is then computed (c). All of the individual traces are then compiled into either a reflection profile (two dimensional snapshot of the flow system) or a time-lapse section (time series plot of a single GPR trace over the full injection period, d).

Table 3.1: Parameters for the basic scenario of the hydrogeologic model.

Property	Value	Modelled Range
	Hydraulic Properties	
Aquifer permeability[1]	2.2×10^{-12} m^2	1.2×10^{-12} m^2 – 6.6×10^{-13} m^2
Aquifer porosity[1]	0.33	0.31, 0.33
Aquitard permeability	6.4×10^{-14} m^2	–
Aquitard porosity	0.39	–
Anisotropy ratio (k_h/k_v)	10	5 – 30
Groundwater velocity	6 cm/day	0 cm/day – 10 cm/day
Entry pressure	2.22 kPa	2.22 kPa, 2.99 kPa
Residual saturation	0.078	–
Pore size distribution index (λ)	2.48	–
Residual gas saturation	0.1	–
	Geometric Properties	
Depth to layer	3 m	–
Layer Thickness	0.5 m	0.2 m – 1.0 m
Aquifer-Aquitard Boundary Depth	9 m	–
Depth to Water Table (above injector)	1 m	–
Model width	20 m	5 m – 30 m
Model depth	10 m	–
Model discretization 0.1 m	–	
	Injector Properties	
Upper Injector Depth	4.5 m	–
Lower Injector Depth	9.0 m	–

[1]The modelled range in permeability and porosity was only applied to the layer

Table 3.2: Relative permeability values used in the basic scenario.

Saturation	Relative Permeability		Gas Phase
	Wetting Phase	*Gas Phase*	Pressure
0.078	0.00	-	-
0.08	-	9.96×10^{-1}	26.3 kPa
0.1	6.68×10^{-7}	9.57×10^{-1}	10.0 kPa
0.2	4.53×10^{-4}	7.33×10^{-1}	5.01 kPa
0.3	4.43×10^{-3}	5.32×10^{-1}	3.94 kPa
0.4	1.82×10^{-2}	3.60×10^{-1}	3.39 kPa
0.5	5.11×10^{-2}	2.22×10^{-1}	3.04 kPa
0.6	1.15×10^{-1}	1.21×10^{-1}	2.79 kPa
0.7	2.24×10^{-1}	5.39×10^{-2}	2.60 kPa
0.8	3.94×10^{-1}	1.68×10^{-2}	2.45 kPa
0.9	6.46×10^{-1}	2.20×10^{-3}	2.32 kPa
1.0	1.00	0.00	2.22 kPa

Table 3.3: Methane injection rates over the duration of the experiment.

Phase	Start Day	End Day	Injection Rates	
			shallow	*deep*
	(days)		(L/min)	
I	0	28	0.06	0.06
II[2]	28	68	0.35	0.35
III	68	70	0.00	0.35
IV	70	72	1.50	1.50
V	72	-	Shut down	

[2]Temporary shutdown between Days 38 – 44

Table 3.4: Investigated parameters and the number of cases used to investigate them. The * represents the hydrologic cases used in the geophysical modelling.

Scenarios	Number of Cases	Values of Parameter	Description
Heterogeneity	2	Uniform*	A uniform aquifer with and without a layer ($k_L = 5.1 \times 10^{-13}$ m^2, $\phi = 0.31$).
		With layer*	
(Varying Layer permeability)	5	$k_L = 1 \times k_{aq}$	An aquifer ($k_{aq} = 2.2 \times 10^{-12}$ m^2) with a layer from 3.0 m – 3.5 m bgs and $\phi = 0.33$.
		$k_L = 0.55 \times k_{aq}$	
		$k_L = 0.3 \times k_{aq}$	
		$k_L = 0.1 \times k_{aq}$	
		$k_L = 0.03 \times k_{aq}$	
Anisotropy	6	$2 \times {}^{k_h}/_{k_v}$ =5	A uniform aquifer with a fixed $k_h = 2.2 \times 10^{-12}$ m^2 and an aquifer with a layer ($k_{h,aq} = 2.2 \times 10^{-13}$ m^2, $\phi = 0.33$) each with adjusted k_v values.
		$2 \times {}^{k_h}/_{k_v}$ =10	
		$2 \times {}^{k_h}/_{k_v}$ =30	
Groundwater velocity	4	0 cm/day	A uniform aquifer with varying groundwater velocity.
		3 cm/day	
		6 cm/day	
		10 cm/day	
Layer thickness	3	0.2 m	A uniform aquitard containing a layer with $k_L = 0.55 \times k_{aq}$, $\phi = 0.33$ with varying thickness.
		0.5 m	
		1.0 m	
Layer entry pressure	2	2.22 kPa	A uniform aquitard containing a layer with $k_L = 0.55 \times k_{aq}$, $\phi = 0.33$ with varying entry pressure of the soil within the layer.
		2.99 kPa	
(Using values from core)	2	2.22 kPa	A uniform aquitard containing a layer with $k = 5.1 \times 10^{-13}$ m^2, $\phi = 0.31$ with varying entry pressure of the soil within the layer.
		2.99 kPa*	
Discontinuous layer	3	-1.5 m	A layer ($k = 5.1 \times 10^{-13}$ m^2, $\phi = 0.31$, $P_c = 2.22$ kPa) that ran across the entire model domain except for a 1 m discontinuity centred at different points in the layer.
		2.5 m	
		6.5 m	
(Increased layer entry pressure with values from core)	3	-1.5 m	A layer ($k = 5.1 \times 10^{-13}$ m^2, $\phi = 0.31$, $P_c = 2.99$ kPa) that ran across the entire model domain except for a 1 m discontinuity centred at different points in the layer.
		2.5 m*	
		6.5 m	
Injection Rate History	8	2 × Actual History	A uniform aquifer and an aquifer with a layer ($k_{aq} = 2.2 \times 10^{-13}$ m^2, $\phi = 0.33$) using different injection rate histories.
		2 × 0.06 L/min	
		2 × 0.35 l/min	
		2 × 1.50 L/min	
(Varying injector configuration)	3	Shallow only	A uniform aquifer using different injector configurations and the actual injection history.
		Deep only	
		Both	

Chapter 4

Results

4.1 Free-Phase Methane Flow

This section describes the impacts of macro-heterogeneity, anisotropy, groundwater velocity, air-entry pressure, layer discontinuity, and injection rate history on the evolution of a free-gas methane plume in an unconfined aquifer based on a numerical analysis of the Borden Methane Injection (BMI) experiment (Cahill et al., 2017). A summary of these scenarios is available in Table 3.4. Time-lapse videos of gas distribution and model outputs are provided in Appendix A.

4.1.1 Heterogeneity

The basic case of methane gas injection into a uniform aquifer ($k_{aq} = 2.2 \times 10^{-12}$ m^2 and $\phi = 0.33$) showed that the gas migrated vertically under buoyancy. As the gas migrated vertically it spread horizontally creating a plume that was thin near the source and wide where it vented into the vadose zone (Figure 4.1). This result is similar to that of the air sparging modelling work completed by N. R. Thomson and Johnson (2000). The plume was skewed in the direction of groundwater flow, extending farther down-gradient than up-gradient. The evolution of the plume in the homogeneous case shows the dominant role of buoyancy and pressure gradients in methane migration. The gas migrates upwards once the pressure gradients and buoyant forces exceed the hydrostatic pressure of the overlying water column; lateral spreading is enhanced by increased pressure (i.e., injection rate)

at the leakage points. In order to minimize energy, the gas pushes outward, extending predominantly down-gradient, where pressure heads are lower than in the up-gradient direction.

When a layer was added to the aquifer from 3.0 m – 3.5 m bgs, with a relatively lower permeability and porosity, $k_L = 5.1 \times 10^{-13}$ m^2 and $\phi = 0.31$, the simulations showed that at early time (e.g., Day 1; Figure 4.1) the gas from the shallow injector was more mobile, migrating vertically to the vadose zone more quickly, compared to the deeper injector for both uniform and layered cases. However, gas in the case of the uniform aquifer was more mobile than the gas in the layered case, reaching the vadose zone within the first 24 hours from the start of the injection.

As the gas injection proceeded (e.g., Days 20 – 71) the lower permeability layer enhanced lateral migration in both the up- and down-gradient direction with consistently higher gas saturations within and below the layer relative to the uniform case. At lower injection rates (i.e., Phases I – III; Days 0 – 70), the gas spread up- and down-gradient along the base of the layer before migrating vertically through the layer toward the vadose zone. At higher injection rates (i.e., Phase IV; Day 70 – 72), the gas further expanded along the base but did not establish a clear preferential pathway vertically to the vadose zone. During the late stages of the injection, the highest gas saturations were observed along the edges of the methane plume below the layer. Following the cessation of the injection on Day 72 residual gas saturation values were similar in both the uniform and layered cases, however in the layered case a larger area of the aquifer was impacted.

The volume of methane gas contained within the model domain (Figure 4.2) was higher in the case with a layer at all times during the 102 day simulation. Gas retention in the aquifer varied with injection rate. During Phase I (Days 0 – 28) of the injection, there was only a marginal increase in gas residence with the inclusion of a lower permeability layer; on average 0.10 m^3 more gas remained in the aquifer during the injection for the layered case. This result follows from Figure 4.1 which shows extensive vertical migration and limited lateral migration during this time. During the subsequent phases (i.e., Phases II – IV), the case with a layer retained much higher gas volumes than the uniform aquifer case (on average 0.67 m^3 for Phases II and III and 0.84 m^3 for Phase IV). Following the cessation of the injection, more gas remained in the model domain of the layered case, which is consistent with the enhanced lateral spreading shown in Figure 4.1.

The volume of gas in the subsurface changes rapidly following rate changes; but as time progresses, the rate of change of gas volume in the subsurface eventually slows, reaching a steady state flow (e.g., Figure 4.2). This response implies that once a preferential path is established, the system will reach equilibrium unless it is perturbed. While Cahill et al. (2017) did note spikes in total dissolved gas pressure following injection rate increases during the actual injection experiment similar to the trends observed in the modelling, there were also a number of distinct events observed in the field that did not correlate with injection rate changes in the modelled gas flow scenarios. These events were likely caused by changes in barometric pressure or irregularities not represented in these simulations (Terry et al., 2016).

The effects of a lower permeability layer were further evaluated with five different layer permeability (k_L) values relative to the background aquifer permeability ($k_{aq} = 2.2 \times 10^{-12}$ m^2): $k_L = 1 \times k_{aq}$, $k_L = 0.55 \times k_{aq}$, $k_L = 0.3 \times k_{aq}$, $k_L = 0.1 \times k_{aq}$, and $k_L = 0.03 \times k_{aq}$. These scaled permeabilities were considered with a uniform $\phi = 0.33$ for the aquifer and the layer. Results from Day 56 are shown in Figure 4.3. These results show that decreasing permeability layers caused greater lateral migration of the methane gas. As travelling through the layer to the vadose zone becomes more difficult, more gas travels laterally to relieve the pressure of the plume below the layer. In the cases of lower permeability contrast (e.g., $k_L \geq 0.3 \times k_{aq}$), the highest gas saturations formed between the shallow injector and the water table with minimal resistance to vertical flow from the layer, enabling the formation of a preferential gas pathway and hotspot at the water table interface. For conditions with higher layer permeability contrast (e.g., $k_L \leq 0.1 \times k_{aq}$) methane emission to the vadose zone was more dispersed, preferentially accumulating gas below the layer. D. A. Thomson (2004) found similar conclusions from cores taken at a contaminated site where dense non-aqueous phase liquids (DNAPLs) would preferentially pool at progressively permeability contrasts.

The addition of a layer also facilitates the mixing of the two plumes. As the pressure required to pass through the layer increases a portion of the gas will spread within and below the layer, resulting in a wider plume than observed without a permeability contrast. Wider plumes are also accompanied by higher gas retention in the aquifer which would have implications to potential chemical reactions or methane degradation. During the BMI Experiment, Cahill et al. (2017) noted that approximately half of the methane injected vented to the atmosphere while the other half remained in the subsurface. This observation, coupled with these simulations, suggest that the methane retained in the aquifer migrates laterally significant distances where it would remain until degradation occurs.

4.1.2 Anisotropy

Six cases with varying anisotropy ratios were considered: $k_h/k_v = 5$, $k_h/k_v = 10$, and $k_h/k_v = 30$ for a uniform aquifer and for an aquifer with a lower permeability layer ($k_L = 2.2 \times 10^{-13}$ m^2, $\phi = 0.33$). Each simulation was performed using a horizontal aquifer permeability of $k_h = 2.2 \times 10^{-12}$ m^2 and $\phi = 0.33$. On Day 56 (Figure 4.4) the gas from the shallow injector travelled upwards and spread laterally in the up- and down-gradient directions with increasing anisotropy, creating a wider zone of desaturation. This increased lateral spreading can be attributed to the decreased vertical hydraulic permeability.

In the cases with lower anisotropy ratios (e.g., $k_h/k_v = 5$) and a uniform aquifer, the methane plumes from both injectors mixed readily, forming a single focused hotspot above the injectors at the water table interface. For the cases with higher anisotropy ratios (e.g., $k_h/k_v = 30$) and a uniform aquifer, the gas plumes from both injectors experienced greater separation resulting in a more heterogeneous gas distribution. This distribution ultimately led to the early formation of two hotspots: one slightly up-gradient, above the shallow injector and another farther down-gradient emanating from the deeper injector. The presence of lower-permeability layers systematically enhanced lateral spreading and dampened the concentration of methane gas at the hotspots.

Enhanced spreading and lateral migration with increasing anisotropy (i.e., decreasing vertical permeability) resulted in higher gas volumes in the aquifer during the active injection phase (Figure 4.5). This increase in gas retention can be explained by the plume width increasing with the degree of anisotropy. The additional size of the methane gas plume, despite being at a lower gas saturation, increases the volume of gas retained in the model domain. Additionally, more time was required for the cases with higher anisotropy ratios to reach steady state flow during active injection and to reach the residual gas saturation after the injection was terminated on Day 72.

Similar to adjusting the permeability within the layer (e.g., Figure 4.3), changing anisotropy affects where the greatest desaturation occurs in the layered case. At low anisotropy, more gas preferentially accumulates within the layer, whereas at a higher degree of anisotropy gas remains below the layer. These two responses are similar to gas behaviour when a layer

in the aquifer has a low permeability contrast (i.e., $k_L \leq 0.3 \times k_{aq}$) or a high permeability contrast (i.e., $k_L \geq 0.1 \times k_{aq}$), respectively. The division between these two accumulation patterns appears to relate to the ratio of the vertical component of permeability to the horizontal component of permeability in the formation above, with a high contrast layer (i.e., gas preferentially accumulating below a layer) being defined by a vertical permeability two orders of magnitude less than the lateral permeability of the adjacent formation.

4.1.3 Groundwater Velocity

A uniform aquifer scenario was modelled with varying average linear groundwater velocity: 0 cm/day, 3 cm/day, 6 cm/day, and 10 cm/day (Figure 4.6 at Day 56). In the absence of groundwater flow (i.e., zero hydraulic gradient), a symmetric chimney formed directly above the injectors leading to rapid gas migration to the vadose zone and the formation of a hotspot at the water table interface. This behaviour aligned with the results of N. R. Thomson and Johnson (2000), whose modelling of air sparging at CFB Borden showed the formation of a symmetric chimney that spread in width as the gas migrated vertically. With the inclusion of horizontal groundwater flow the gas preferentially migrated down-gradient; the degree of down-gradient migration increased with groundwater velocity. Increasing the groundwater velocity eventually led to the formation of two distinct gas plumes (e.g., 10 cm/day), each emanating from their source of origin.

Horizontal groundwater flow enhanced lateral migration, effectively smearing the gas plume across a larger area of the aquifer, increasing the gas retention (Figure 4.7). Interestingly, the increase in gas retention in the model domain is non-linear with respect to the groundwater velocity, with negligible increase in the volume of gas between the 3 cm/day and 6 cm/day cases relative to the increases observed between the 0 cm/day and 3 cm/day cases and the 6 cm/day and 10 cm/day cases. The non-linearity of methane gas retention is likely related to plume separation caused by increased hydraulic gradients. When there is no groundwater flow, the pathway of gas migration forms a single compact pathway with the gas rising from the lower injector more quickly due to the sudden reduction in the hydrostatic pressure caused by the upper injector. When the groundwater begins to flow the pathway is pushed down-gradient and hydrostatic pressures become more variable. Since the gas is no longer migrating in a vertical path, a longer path, with a higher volume is needed to connect the gas from the deep injector to the gas plume from the shallow injector. The length of this path is not changed considerably when the groundwater velocity increases from 3 cm/day to 6 cm/day since the plumes from both injectors still eventually

combine to form a single pathway. Increasing the groundwater velocity further shifts the position of the plume from the deep injector until the plumes no longer converge. This divergence caused the large increase in gas retention (i.e., the increase observed between 6 cm/day and 10 cm/day), since the two individual pathways contain more gas than a single shared pathway.

4.1.4 Layer Thickness

A layer with $k_L = 5.1 \times 10^{-13}$ m^2 and $\phi = 0.31$ with an upper boundary at a depth of 3 m bgs was added to the aquifer ($k_{aq} = 2.2 \times 10^{-12}$ m^2, $\phi = 0.33$) for three different layer thicknesses: 0.20 m, 0.50 m, and 1.00 m. Conditions on Day 56 (Figure 4.8) reveal enhanced lateral spreading up- and down-gradient with increasing layer thickness. This lateral spreading was accompanied by a systematic reduction in the magnitude of gas saturation above the layer, resulting in a more diffuse gas distribution along the water table interface (i.e., defocussing hotspot). Gas retention in the aquifer (Figure 4.9) increased non-linearly with layer thickness. A more notable difference in gas volume was observed at moderate and higher injection rates (i.e., Phases II – IV) with more gas retained in the aquifer for progressively thicker layers.

4.1.5 Entry Pressure

The effects of layer entry pressure was considered for the case of an aquifer with a layer from 3.0 m – 3.5 m bgs with $k_L = 0.55 \times k_{aq}$ and $\phi = 0.33$ for two air-entry pressure scenarios: $P_c = 2.22$ kPa representing the case of a uniform entry pressure across the layer boundary, and $P_c = 2.99$ kPa representing the case of an increase in air-entry pressure of the less permeable layer (Figure 4.10 at Days 20, 37, and 56). An increase in the entry pressure of the layer relative to the adjacent material resulted in free-phase gas pooling along the lower layer boundary. This pooling was accompanied by the formation of distinct vertical preferential pathways up- and down-gradient from the injection points, contributing to a more heterogeneous distribution of gas within and above the layer. Although an increase in air-entry pressure enhanced the spatial distribution of the gas below the layer, a negligible increase in plume width was observed above the layer. However, gas efflux into the vadose zone was more variably distributed for the higher entry pressure scenario, resulting in the formation of multiple gas hotspots along the water table interface.

Methane gas migration simulations using the laboratory measured parameters for the layer (i.e., $k_L = 5.1 \times 10^{-13}$ m^2 and $\phi = 0.31$) with entry pressures of $P_c = 2.22$ kPa and $P_c = 2.99$ kPa (Figure 4.11), were similar to that based on the scaled permeability scenario (e.g., Figure 4.10). However, the vertical pathways appeared slightly earlier and with greater frequency compared to the scaled-permeability scenario creating a more heterogeneous gas distribution above the layer.

Even though changes in layer entry pressure contributed to more variable distributions of gas within the aquifer, it had a minor impact on the volume of gas retained in the aquifer (Figure 4.12). Based on Figure 4.10, the slight differences in gas accumulation between the cases with and without adjusted entry pressures in gas accumulation are likely attributed to the formation and timing of secondary and tertiary preferential pathways through the low permeability layer (e.g., single pathway during low injection rate on Day 20 compared to multiple pathways during higher injection rates on Days 37 and 56, in the low permeability case).

As the gas migrated vertically towards the low-permeable layer with a higher entry pressure it spread more quickly along the base of the layer, and travelled much farther than along an interface with no change in air-entry pressure (Figure 4.10 and 4.11). The migration occurred in a relatively thin pool of gas that formed as a distinct lens under the layer. From this pool thin paths broke through the layer and travelled upwards to vent to the vadose zone. All of these thin features that made up the migration pathways of the gas-phase methane created a distribution of gas much more heterogeneous than seen in the unadjusted cases. This pattern of migration is similar to observations from Brewster et al. (1995) with DNAPLs settling on top of less permeable lenses. The authors showed that dense fluids travelling downwards due to gravity would settle on top of the low-permeable lenses eventually breaking through as the DNAPL accumulated forming preferential pathways through the layer.

Cahill et al. (2017) made several observations consistent with the numerical simulations of gas migration. The first observation was the occurrence of variable methane efflux patterns at the surface. Cahill et al. (2017) began noting methane efflux hours after the beginning of the injection which agrees with the conceptual model of dominant veritcal migration caused by buoyancy. The zones from which the gas escaped to the atmosphere were on the order of a few meters, which is consistent with the modelling, indicates that the efflux zone tended to be more concentrated in cases where the layer had a higher entry pressure. The temporal pattern of gas release, however, was different between the models and this

research. Cahill et al. (2017) reported multiple large release events at one location, that quickly peaked and returned to background effluxes, while the modelling showed consistent venting that changed with injection rate. This difference could be attributable to the inherent qualities of a real system with subtle heterogeneities that cannot be captured by relatively simple models. The more transient response observed during the BMI Experiment could be explained by a barometric variations or by gas building-up and releasing in multiple interconnected lenses in the aquifer.

4.1.6 Layer Discontinuities

A discontinuous layer with $k = 5.1 \times 10^{-13}$ m^2 and $\phi = 0.31$ was added to the aquifer ($k_{aq} = 2.2 \times 10^{-12}$ m^2, $\phi = 0.33$) from 3.0 m – 3.5 m bgs. Six cases were modelled, in which the layer did not extend continuously across the entire width of the model domain (i.e., -8 m to 12 m downgradient of the injectors[1]) but had a 1 m long discontinuity with the same hydraulic properties as the aquifer centred at: -1.5 m, 2.5 m, and 6.5 m. Each of these three layer geometries were modelled twice with the layer having one of two entry pressures: $P_c = 2.22$ kPa (same as the aquifer) or $P_c = 2.99$ kPa. Based on the change in gas saturation relative to the start of the injection (Figure 4.13 at Day 56), the position of the primary hotspot was only slightly affected by the position of the discontinuity for the case of $P_c = 2.22$ kPa. However, the impact of a discontinuity on the vertical gas migration was more apparent for the case of higher layer entry pressure (e.g., discontinutity between 2 m and 3 m for $P_c = 2.99$ kPa). However, these effects diminished as the discontinuity moved farther downgradient (e.g., 6 m to 7 m).

In all cases with the higher layer entry pressure, the location of the discontinuity had a more pronounced effect on gas channelling and the distribution of the gas above the layer; however, in each of these cases, a portion of the gas migrates horizontally past the discontinuity, particularly for the case of a layer with higher entry pressure supporting the formation of laterally extensive gas pools.

[1]Positions are presented as distances down-gradient from the injector.

4.1.7 Injection Rate History

Eight cases were used to assess the impact of the injection rate history: two cases using the actual injection rate history, and six cases based on a single constant injection rate corresponding to the individual rate steps: Phase I (0.06 L/min), II (0.35 L/min), and IV (1.50 L/min). Each injection rate was modelled twice, once with a uniform aquifer ($k_{aq} = 2.2 \times 10^{-12}$ m^2, $\phi = 0.33$) and once with a layer included from 3.0 m – 3.5 m bgs with $k_L = 2.2 \times 10^{-13}$ m^2, $\phi = 0.33$. In both the cases with and without a layer, higher injection rates (i.e., pressure gradients) led to greater lateral migration in both the up- and down-gradient direction and higher levels of desaturation within the aquifer (Figure 4.14 at Day 56). In the uniform aquifer case, the plume characteristics drawn from the actual injection rate largely resembled that of the moderate (0.35 L/min) constant rate case. However, when a layer was added to the aquifer the plume characteristics resembled an amalgamation of each of the individual rates: low gas saturations above the layer resembled that of the lowest injection rate case; the broad lateral extent of the plume was consistent with that of the moderate injection rate; and the extensive desaturation and pooling of gas beneath the layer was similar to that observed at the highest injection rate.

The actual injection rate history (see Table 3.3) is characterized by a more variable gas residence curve relative to the constant rate injectors (Figure 4.15). An examination of the total gas in the model domain during Phase II, before and after the temporary shut-down, reveals hysteretic characteristics in gas saturation over that time that relate to the stepped increase in injection rate and the temporary shut-down event. For instance the actual injection rate led to higher gas residuals in the layered aquifer case and lower residuals in the uniform case, both of which were slightly less than those observed for the highest constant injection rate. The rate and magnitude of gas accumulation in the aquifer increased after the temporary shut down, compared to what was observed prior to the shut-down. These simulations suggest that gas residence is primarily associated with changes in injection rate; on the other hand, the BMI Experiment indicates that a variety of factors (e.g., heterogeneity, stratospheric pressure, precipitation) likely contribute to transience in gas retention alongside injection rate changes (Cahill et al., 2017).

To examine the impact of two simultaneous injectors on the spatiotemporal evolution of the gas plume, three cases using the actual injection rate history in a uniform aquifer were employed: one case using only the shallow injector; one case using only the deep injector; and one case using both injectors. At Day 71 (Figure 4.16), the shallow injector case formed a broad, nearly symmetrical plume, while the deeper injector formed a narrower and less

symmetric plume that preferentially migrated down-gradient. When both injectors were used simultaneously, the gas distribution resembled a superposition of the gas distributions from the individual injectors; however both lateral spreading above the shallow injector and down-gradient gas migration were enhanced relative to the individual cases.

Figure 4.16 exemplifies the effect of counteracting forces between buoyancy and hydrostatic pressure during methane injection. When gas is injected near the surface alone (i.e., 4.5 m bgs) the gas spread equally far up- and down-gradient, whereas gas from the deeper well alone migrated almost entirely down-gradient of the injection point. For the latter case, gas migration was heavily influenced by pressure head gradients.

4.2 Electrical Resistivity Tomography

4.2.1 Homogeneous Aquifer

Electrical resistivity tomography (ERT) in a homogeneous subsurface showed an anomalous rise in the electrical resistivity over the course of the injection that roughly approximated the location of the main gas plume. Figure 4.17 shows the simulated responses (hydrogeologic and geophysical) on Day 56 (further ERT modelling results are shown in Appendix B). Here, a resistivity increase corresponds to a reduction in the pore water within the aquifer material (Archie, 1942). Slater et al. (2007) reported similar results when observing the resistivity of an ex-situ peat block, whereby methanogenesis within the peat (i.e., methane gas formation) caused an increase in the electrical resistivity.

While the most apparent response seen by ERT was an increase in resistivity, small decreases, implying increasing saturation, were also observed. While Doetsch et al. (2015) observed decreases in resistivity during a gas-phase carbon dioxide injection, these were caused by alteration in the groundwater chemistry associated with the presence of dissolved carbon dioxide. Since chemical degradation and biological reactions were not incorporated in the gas flow modelling, changes in groundwater chemistry were not accounted for; thus, any decreases in resistivity can be attributed to the 3% noise added to the forward model and inversion artefacts.

Gas saturation estimates from the change in resistivity show similar saturation values near surface. At greater depths, the predicted saturation distributions from the ERT begin

to differ from the simulated distribution; the predicted saturation distribution is wider than the true gas distribution at the shallow injector, and there is no observed response in the calculated saturation at the deeper injector. The parabolic shape described by N. R. Thomson and Johnson (2000) is also not well defined by the resistivity response; instead the response describes a box-like distribution with an equal width.

Saturation values approximated from ERT data begins to approximate the true saturation near surface. The width of the hotspot, where methane is released to the vadose zone is reasonably well represented by the ERT data, suggesting that ERT may be useful for estimating the gross volume of methane in the subsurface and identifying the position of hotspots. However, the utility of ERT to estimate gas saturations will depend on the accuracy of fitting parameters in Archie's Equation, which typically requires calibration to specific site conditions.

4.2.2 Aquifer with a Layer

A large zone of increased resistivity is shown roughly in the center of the methane plume, as illustrated by the response on Day 56 (Figure 4.18; further days shown in Appendix B). Again, the change in resistivity roughly approximates the shape of the plume around the shallow injector with diminished agreement deeper in the aquifer. Despite the similarity in the resistivity responses between the homogeneous and heterogeneous cases, this case highlights some limitations in using ERT to estimate distribution of gas saturation. The central chimney in the layer case is much thinner than the width of the central chimney predicted by the resistivity data. Furthermore, the arrival of small preferential pathways (e.g., up-gradient) are not resolved by ERT. Although these are inherent limitations of ERT, these observations illustrate some of the considerations that need to be made in geophysical interpretations of gas distribution in the shallow subsurface.

4.2.3 Layer with Adjusted Entry Pressure

As in both previous cases, the ERT response ably captures the bulk gas migration in the shallow subsurface, but becomes more limited with depth, showing no response at the deep injector (Day 56 shown in Figure 4.19; further days in Appendix B). As in the previous cases, this diminished sensitivity with depth can be attributed to inherent limitations of

ERT. Here, the inability to detect thin features becomes even more apparent, as lateral migration in thin pools extends quite far in the up- and down-gradient directions and is not readily evident in the ERT response. The primary gas bulb emanating from the injectors is reasonably well defined by the central resistivity response; however, the establishment of more complex vertical gas pathways up- and down-gradient are not imaged in the ERT model. It should be noted that the position of multiple vertical pathways observed up-gradient coincides with a zone of high resistivity along the water table.

The presence of a discontinuity within the low-permeable layer (i.e., Day 56 shown in Figure 4.20) leads to a reduction in the bulk gas saturation below the layer. ERT simulations indicate that the primary response associated with the gas has shifted upward in the profile. These data also show an increase in resistivity slightly down-gradient along the water table interface which corresponds to the formation of a preferential gas pathway through the discontinuity and eventual efflux into the vadose zone. Similar responses were observed on other days of the injection period (refer to Appendix B).

4.3 Ground-Penetrating Radar

4.3.1 Homogeneous Aquifer

A lack of sedimentary structures limits the build-up of gas within the aquifer. Strong reflections in ground-penetrating radar (GPR) data require sharp dielectric boundaries (Everett, 2013), so little change can be expected in the GPR signal for the homogeneous case. An unexpected response was observed on Day 37 (Figure 4.21, additional days in Appendix C); here, a series of diffractions formed along the side of the plume. Diffractions tend to be associated with points marking an abrupt change in dielectric permittivity, such as a small void or discontinuity along a boundary. Many diffractions with small amplitudes line either side of the plume, while a large diffraction is present at the bottom of the plume, approximately at the methane injection point. The high concentration of gas and steep saturation gradient around the injector results in a stronger hyperbola at the base of the plume than along the sides, where the gas gradient is less extreme.

The only notable reflection response in the homogeneous case is that along the water table, which is demarcated by diminished reflection amplitude along the full extent of the

hotspot. This response is associated with a reduction in the dielectric contrast and smearing of the capillary fringe. At Day 37 (Figure 4.21) the water table above the injector nearly disappears, while it is still visible past the extent of the hotspot. Changes in the enveloped energy at positions -1.5 m, 2.5 m and 6.5 m from the injection horizon (Figure 4.22) show a dynamic GPR response along the water table, and near the injectors (i.e., Figure 4.22c). During Phase I, there is an increase in the water table reflection from background. This is likely attributed to a bulge in the water table above the gas injector caused by the disturbance in the pressure as gas began to migrate through the aquifer. During Phase II and beyond, the reflected energy from the water table decreases relative to background conditions, indicating that the water table has either dropped or simply become a more gradual change in saturation as gas begins to imbibe the pore space.

The time-lapse plots show a number of elevated amplitudes that are stationary over the course of the injection. These events represent the tails of diffractions associated with the outer extent of the gas plume and the gas injection points (discussed above; Figure 4.21). The fact that these events appear stationary in time indicates that the diffractions do not substantially change in shape or location over the course of the injection. Since these diffractions are related to the gas saturations, it is likely that gas saturations stabilize quickly following each change in injection rate.

4.3.2 Aquifer With a Layer

When a layer with $k = 5.1 \times 10^{-13}$ m^2 and $\phi = 0.31$ is present in the aquifer, a dielectric permittivity contrast forms within the saturated zone, which results in a strong reflection in the GPR profile. A number of diffractions still define the outer boundary of the gas plume, with a strong diffraction occurring at the injector (Day 37, Figure 4.23; additional days available in Appendix C). Additionally, the water table reflection disappears over time due to the formation of the hotspot. While these responses are similar to the homogeneous case, the addition of a layer led to the accumulation of gas, and thus, stronger dielectric permittivity contrasts in the aquifer.

Day 37 shows a pull-up in the reflection event associated with the layer due to increased GPR velocity resulting from higher gas saturations above the layer (e.g., Day 0, available in Appendix C). Lassen et al. (2015) observed a similar increase in the velocity of electromagnetic waves using cross borehole GPR during a carbon dioxide injection. Based on

the change in reflected energy over time at -1.5 m, 2.5 m, and 6.5 m from the injection horizon (Figure 4.24) the response of the layer is most noticeable between 50 ns and 150 ns (approximately 1.5 m to 4.5 m, assuming a constant velocity of 0.06 m/ns). During Phase I, gas build-up is most apparent within and around the layer, as evidenced by the increased signal amplitude. However, the response does not change the time at which it occurs, implying that less desaturation has occurred above the layer compared to the homogeneous case. During Phase II and later, the response is mostly consistent: four bands alternating between increased and decreased energies relative to background. The two increased energy responses are associated with the reflections from the top and bottom of the layer while the two decreased responses are the reflections from the top and bottom of the layer before the injection. This shows the reflection from the layer has shifted up in time (i.e., arrives at an earlier time relative to background).

Integrating the reflected energy between 50 ns and 150 ns shows that the GPR response around the layer changed sharply at each rate change, but stabilized quickly thereafter. These spikes are likely associated with a build-up of gas below the layer before pressures exceed entry pressure. Once a pathway through the layer is established the gas migrates vertically and vents to the surface, decreasing the gas saturation below the layer and lowering the reflected GPR energy.

This case represents a low contrast scenario, which tends to result in gas accumulation within the layer with comparable gas saturations above and below. Since the gas saturations are more uniformly distributed within the layer, the reflection events from the top and bottom of the layer are of similar amplitude. When the layer has a substantially lower permeability (>2 orders of magnitude), the gas saturations tend to be highest below the layer. These high contrast permeability cases tended to be laterally extensive with lower saturations above the layer, resulting in a less pronounced reflection pull-up.

4.3.3 Layer with Adjusted Entry Pressure

When a layer with $k_L = 5.1 \times 10^{-13}$ m^2 and $\phi = 0.31$ is added and the entry pressure is increased to $P_c = 2.99$ kPa the GPR response begins to show more spatial and temporal variability in amplitude compared to the homogeneous and layered cases. At Day 37 (Figure 4.25, further days in Appendix C), it is seen that the water table reflection at the hotspot has effectively disappeared, reflector pull-up is readily visible and is accompanied

by ample diffractions associated with the accumulation of gas along the base of the layer. Unlike the previous cases, the majority of the diffractions (i.e., the bulk of the reflected energy) occurs along the interface, marking the position of preferential pathways through the layer. Although the pull-up is visible in the layer, the intensity of the pull-up is masked by the diffractions. At later times, such as Day 56 (available in Appendix C) the diffractions begin to diminish as the gas distribution begins to homogenize (i.e., reduction in spatial variability in gas saturation).

Gas plume extension along the base of the layer is visible in the GPR response in all of the sections. Here, the sharp boundary formed by the migration of methane forms an ideal GPR target, especially in areas where methane migrated in thin pools laterally away from the main plume. This response shows that GPR has the capacity to track the pooling of methane at hydrogeologic boundaries. This result parallels those of Brewster and Annan (1994) who used GPR to monitor DNAPL migration in the Borden aquifer. In their case, the fluid was denser than water and moved downwards under gravity, and was shown to cascade along a series of discontinuous lenses of lower-permeability sand within the aquifer.

From the response at -1.5 m, 2.5 m, and 6.5 m from the injection horizon, both the build-up along the base of the layer and the pull up of the layer can be observed (Figure 4.26). The integrated amplitude between 50 ns and 150 ns (approximately 1.5 m to 4.5 m, assuming a constant velocity of 0.06 m/ns) shows large perturbations in signal amplitude corresponding to each rate change. Unlike the previous case, the time required for the GPR energy to stabilize (i.e., reach a steady state) is much longer. Additional high amplitude events occur below the layer; these correspond to the diffracted energy emanating from preferential pathways through the layer (see Figure 4.25). The gradual reduction in traveltime of these events is the result of progressively higher GPR velocities due to the accumulation of gas above the layer.

When a similar layer ($k_L = 5.1 \times 10^{-13}$ m^2, $\phi = 0.31$, $P_c = 2.99$ kPa) with a 1 m discontinuity centred at 2.5 m was introduced the diffractions become less pronounced along the base of the layer; additional diffraction events form along the terminus of the layer (i.e., at the edges of the discontinuity; Day 37 in Figure 4.27). The time-lapse enveloped amplitude plots at -1.5 m, 2.5 m, and 6.5 m from the injection horizon (Figure 4.28) show that the lateral extent of gas-phase along the base of the layer is constrained to the immediate up- and down-gradient directions (i.e., -1.5 m and 2.5 m) during Phase I, with limited distribution farther down-gradient during initiation of Phase II. However, after the temporary shut down and commencement of Phase II injection rate, a significant increase

in the reflection event was observed at 6.5 m. This suggests that the temporary shut down led to an enhancement in the lateral mobility of free-phase methane within the aquifer.

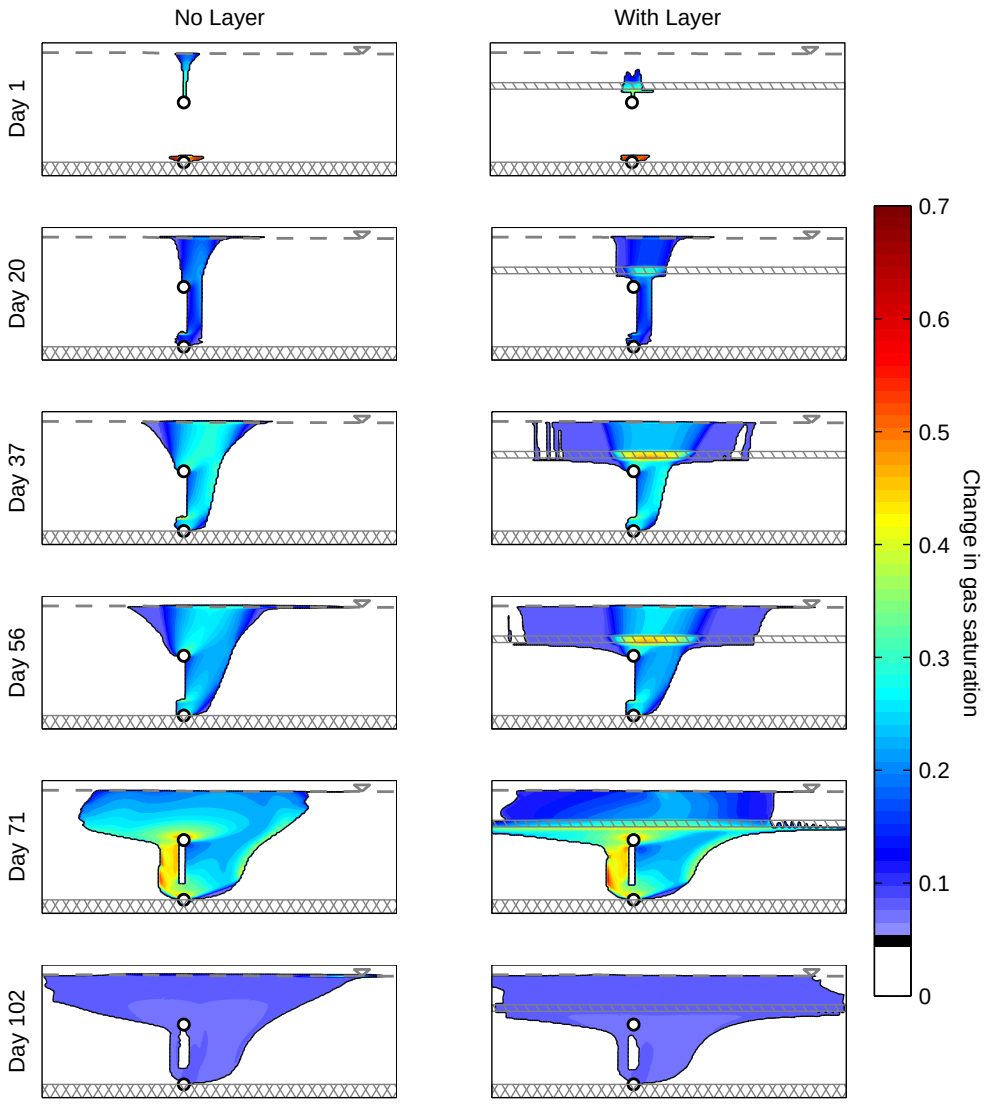

Figure 4.1: Change in gas saturation relative to the start of the injection at different times during the injection for a case of a uniform aquitard and for a case with a layer in the aquitard. The pre-injection water table is shown by the grey dashed line, the injectors by white circles with a black outline, the aquitard by the grey cross-hatching and the layer by the grey single hatched area.

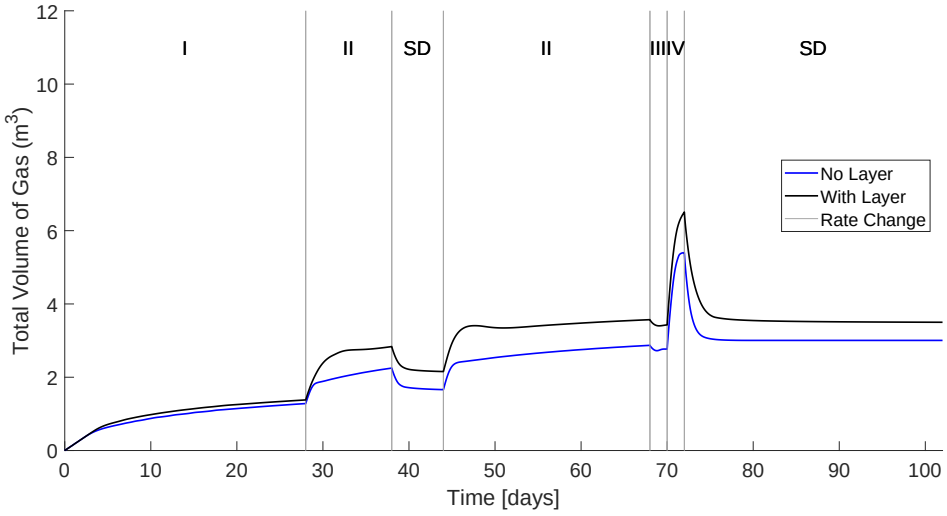

Figure 4.2: Total volume of methane within the model domain at standard temperature and pressure for two cases, one without a layer and one with a layer in the aquifer.

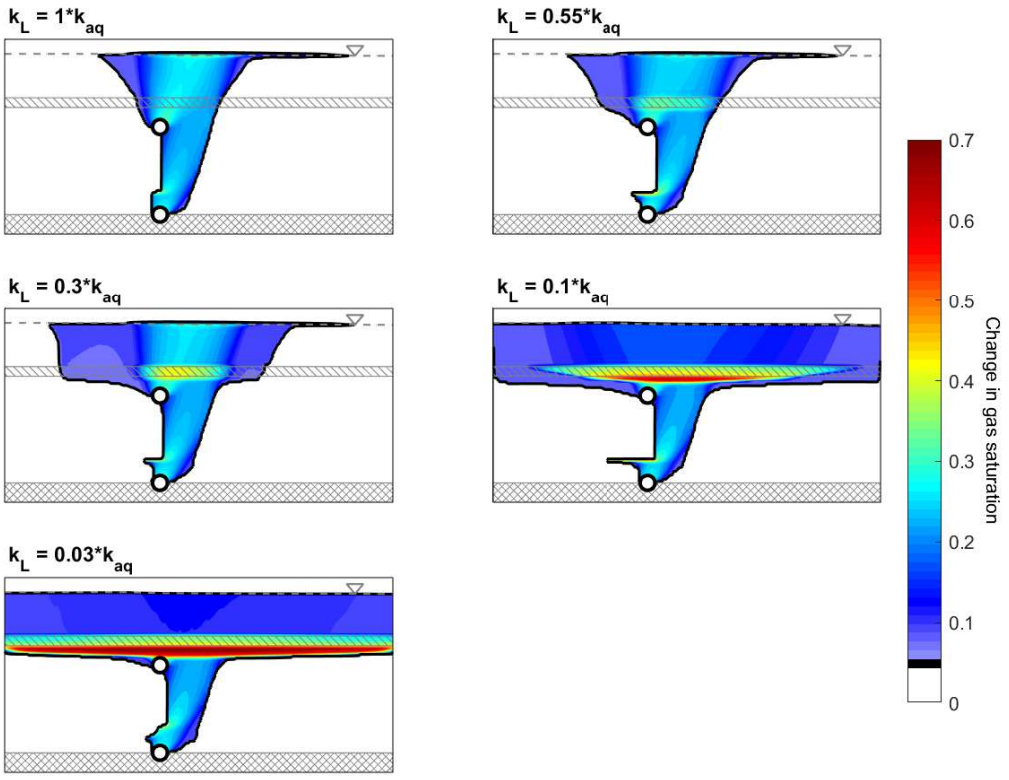

Figure 4.3: Change in gas saturation relative to the start of the injection at Day 56 of the injection for five cases with differing permeability contrasts between the layer (k_L) and the aquifer ($k_{aq} = 2.2 \times 10^{-12}$ m^2): $k_L = 1 \times k_{aq}$, $k_L = 0.55 \times k_{aq}$, $k_L = 0.3 \times k_{aq}$, $k_L = 0.1 \times k_{aq}$, and $k_L = 0.03 \times k_{aq}$. The pre-injection water table is shown by the grey dashed line, the injectors by white circles with a black outline, the aquitard by the grey cross-hatching and the layer by the grey single hatched area.

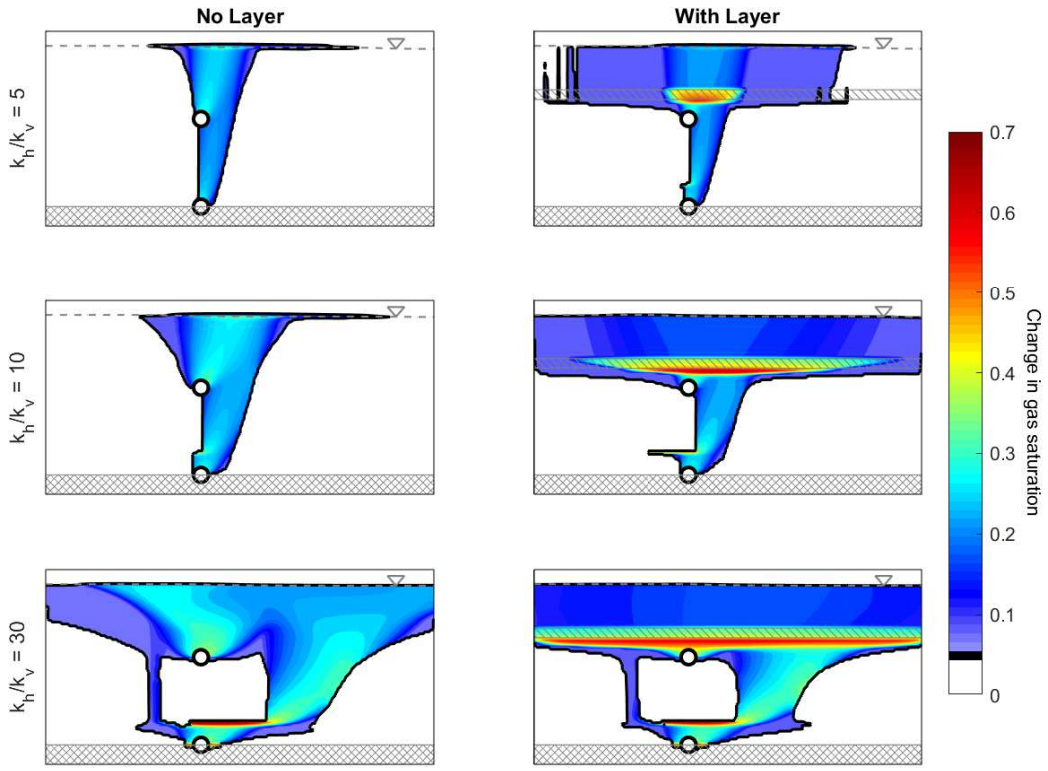

Figure 4.4: Change in gas saturation relative to the start of the injection at Day 56 of the injection for six cases with varying anisotropy ratios half in a homogenous aquifer and in an aquifer with a low permeability layer: $^{k_h}/_{k_v} = 5$, $^{k_h}/_{k_v} = 10$, and $^{k_h}/_{k_v} = 30$. The pre-injection water table is shown by the grey dashed line, the injectors by white circles with a black outline, and the aquitard by the grey cross-hatching.

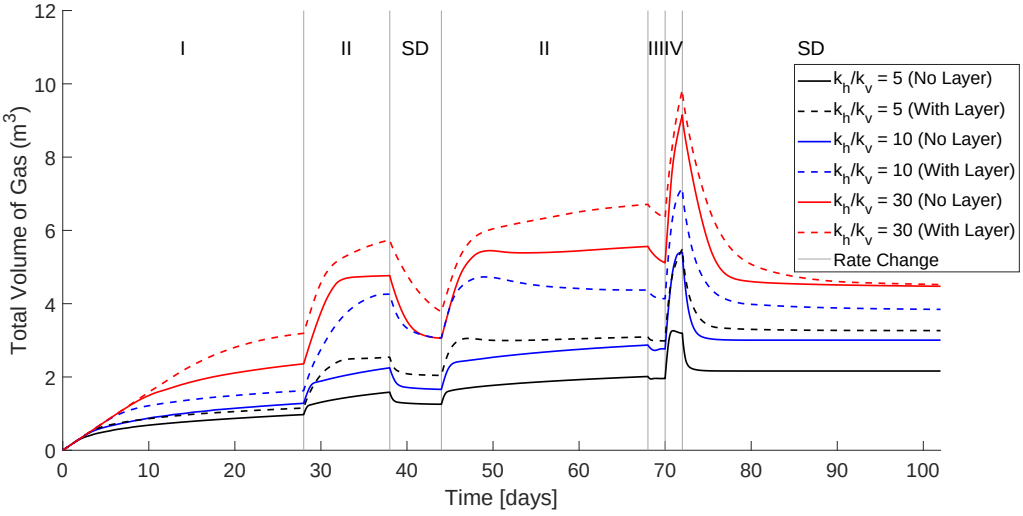

Figure 4.5: Total volume of methane within the model domain at standard temperature and pressure for six cases with differing anisotropy ratios: $k_h/k_v = 5$, $k_h/k_v = 10$, and $k_h/k_v = 30$ in a homogeneous aquifer and in an aquifer with a low permeability layer.

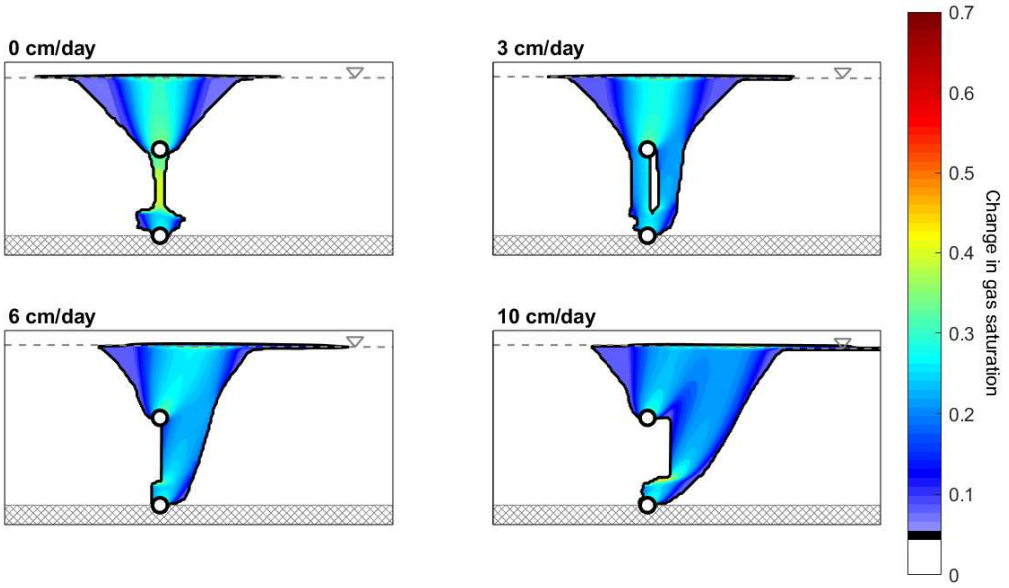

Figure 4.6: Change in gas saturation on Day 56 relative to the start of the injection for four cases with differing groundwater velocities in a uniform aquifer: 0 cm/day, 3 cm/day, 6 cm/day, and 10 cm/day. The pre-injection water table is shown by the grey dashed line, the injectors by white circles with a black outline, and the aquitard by the grey cross-hatching.

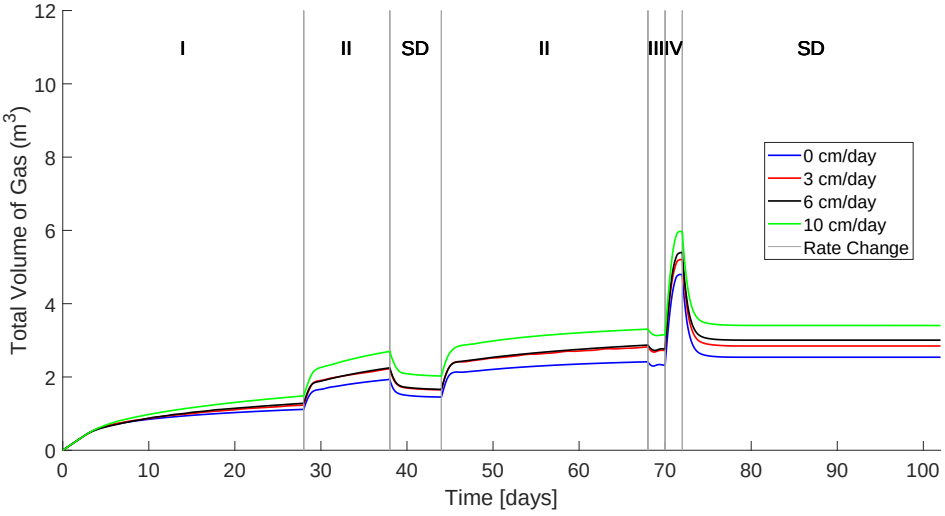

Figure 4.7: Total volume of methane within the model domain at standard temperature and pressure for four cases with differing groundwater velocities: 0 cm/day, 3 cm/day, 6 cm/day, and 10 cm/day.

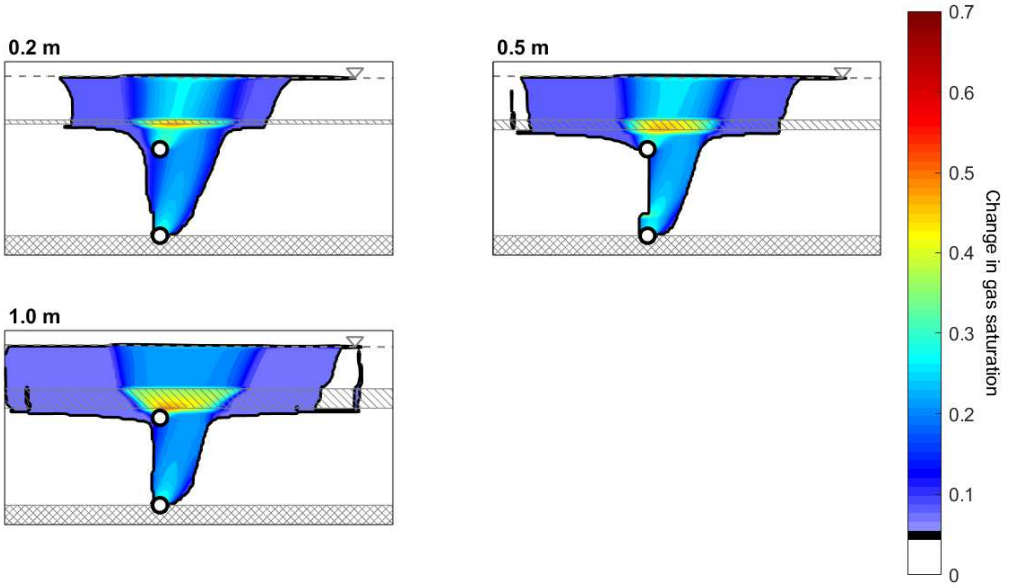

Figure 4.8: Change in gas saturation relative to the start of the injection at Day 56 of the injection for three cases with differing thicknesses of a layer within an aquifer: 0.20 m, 0.50 m, and 1.00 m. The pre-injection water table is shown by the grey dashed line, the injectors by white circles with a black outline, the aquitard by the grey cross-hatching and the layer by the grey single hatched area.

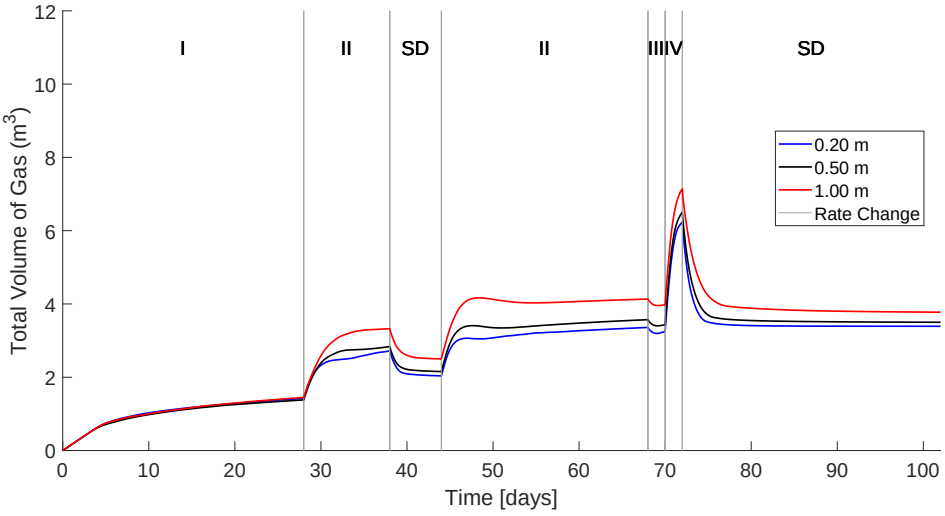

Figure 4.9: Total volume of methane within the model domain at standard temperature and pressure for three cases with differing layer thicknesses: 0.20 m, 0.50 m, and 1.00 m.

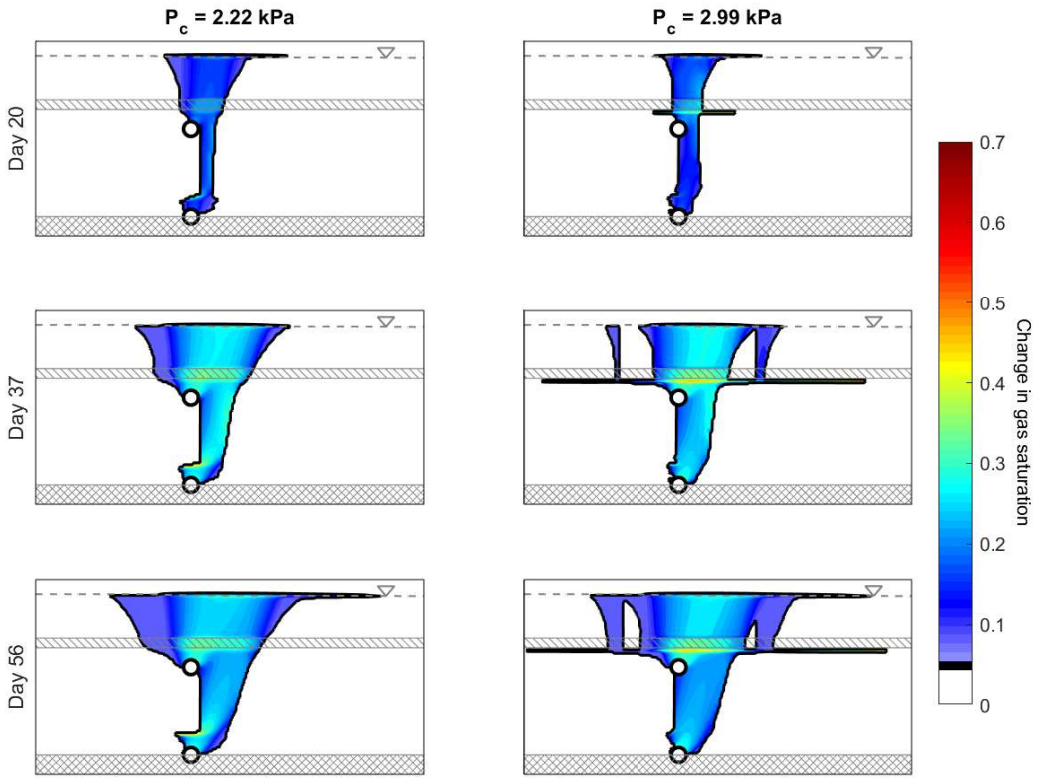

Figure 4.10: Change in gas saturation relative to the start of the injection at Days 20, 37, and 56 of the injection for two cases with differing entry pressures for a layer within an aquifer with $k_L = 0.55 \times k_{aq}$ and $\phi = 0.33$: $P_c = 2.22$ kPa, and $P_c = 2.99$ kPa. The pre-injection water table is shown by the grey dashed line, the injectors by white circles with a black outline, the aquitard by the grey cross-hatching and the layer by the grey single hatched area.

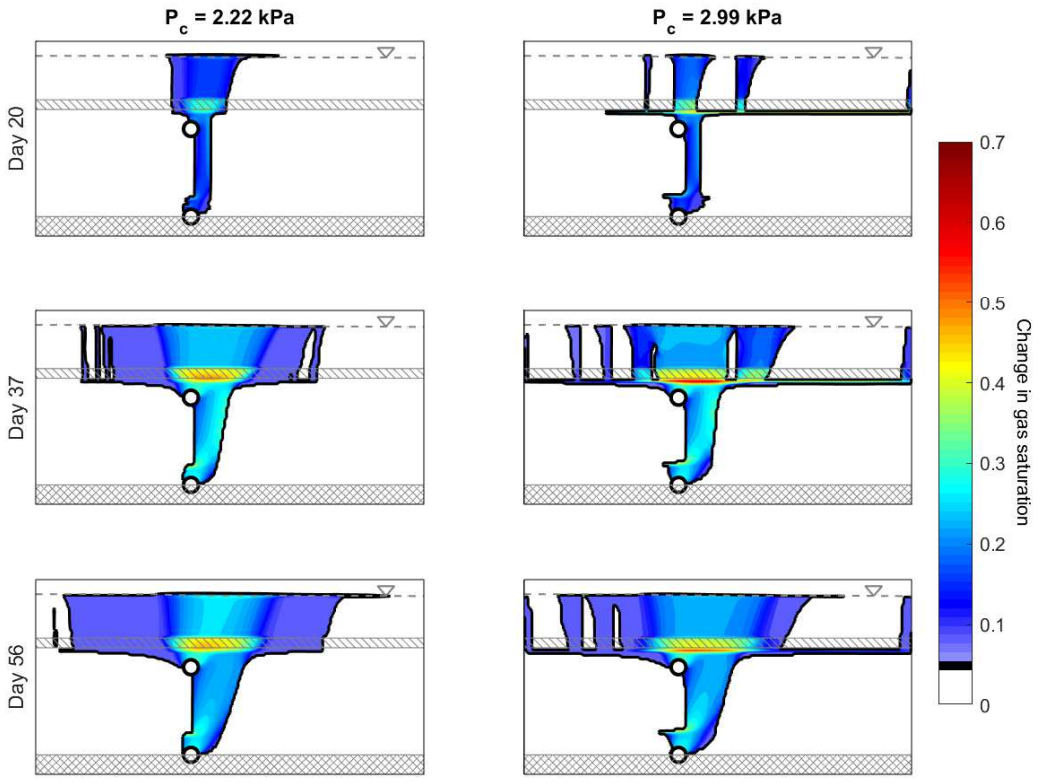

Figure 4.11: Change in gas saturation relative to the start of the injection at Days 20, 37, and 56 of the injection for two cases with differing entry pressures for a layer within an aquifer with $k = 5.1 \times 10^{-13}$ m^2 and $\phi = 0.31$: $P_c = 2.22$ kPa, and $P_c = 2.99$ kPa. The pre-injection water table is shown by the grey dashed line, the injectors by white circles with a black outline, the aquitard by the grey cross-hatching and the layer by the grey single hatched area.

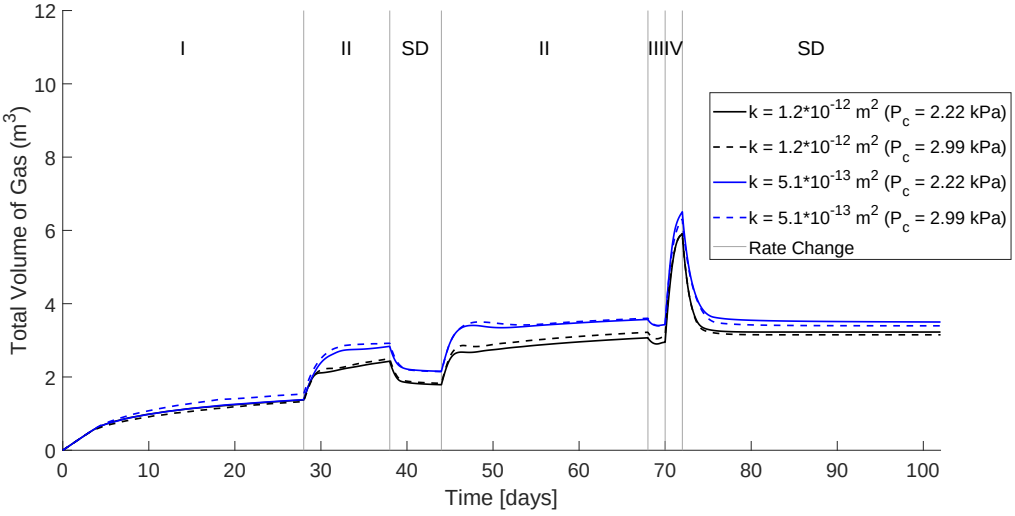

Figure 4.12: Total volume of methane within the model domain at standard temperature and pressure for two cases with differing entry pressure for the soil within the layer: $P_c = 2.22$ kPa and $P_c = 2.99$ kPa.

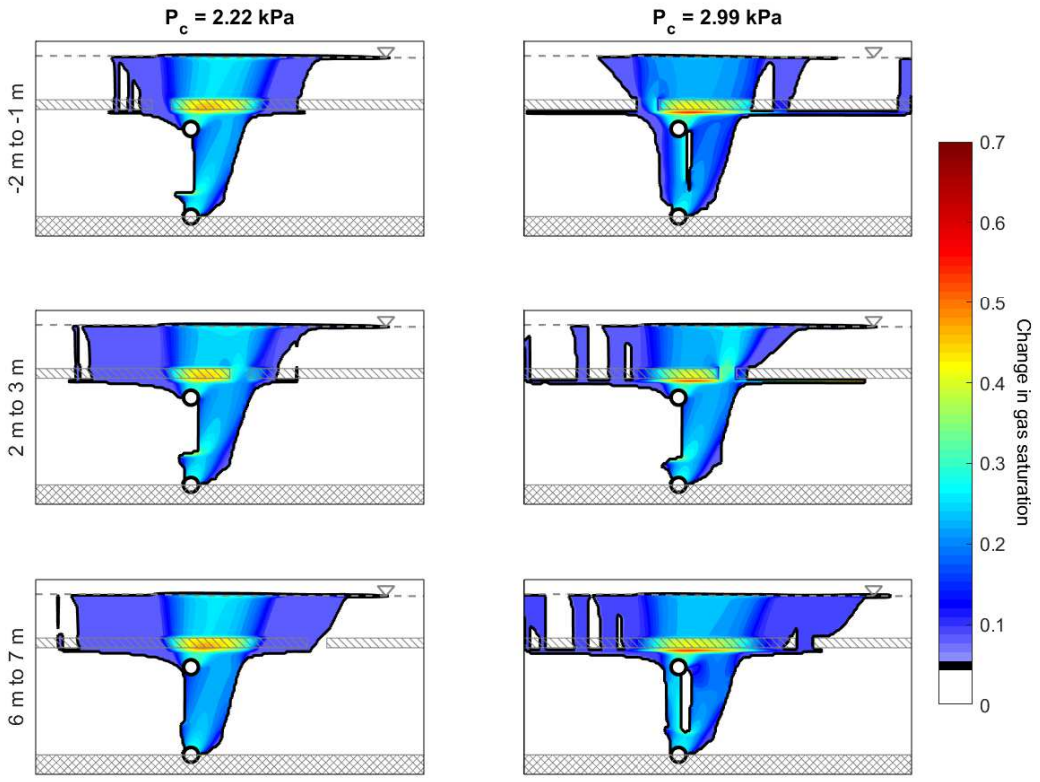

Figure 4.13: Change in gas saturation relative to the start of the injection at Day 56 of the injection for six cases with a discontinuous layer within an aquifer, with a 1 m discontinuity centred at: -1.5 m, 2.5 m, and 6.5 m downgradient of the injectors and two entry pressures: $P_c = 2.22$ kPa and 2.99 kPa. The pre-injection water table is shown by the grey dashed line, the injectors by white circles with a black outline, the aquitard by the grey cross-hatching and the layer by the grey single hatched area.

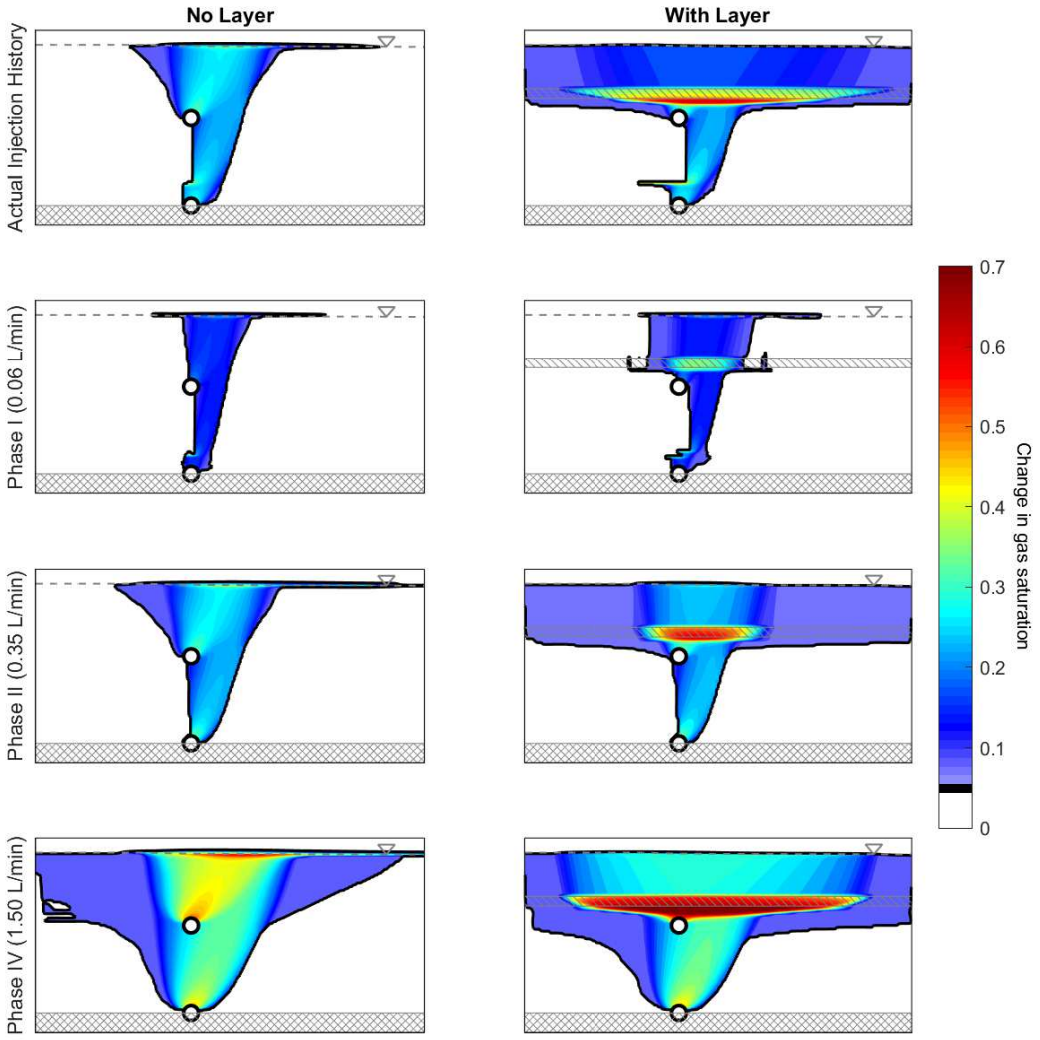

Figure 4.14: Change in gas saturation on Day 56 relative to the start of the injection for four cases of a uniform aquifer (left) and an aquifer with a low permeability layer with varying methane injection histories, one using the actual injection history and three using a constant injection rate of: 0.06 L/min, 0.35 L/min, or 1.50 L/min. The pre-injection water table is shown by the grey dashed line, the injectors by white circles with a black outline, the aquitard by the grey cross-hatching and the layer by the grey single hatched area.

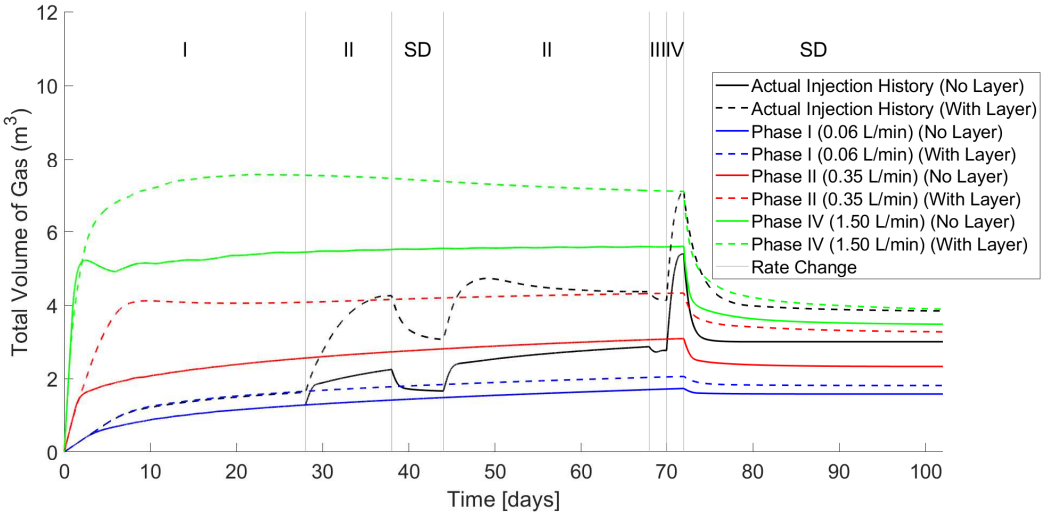

Figure 4.15: Total volume of methane within the model domain at standard temperature and pressure for eight cases with differing methane injection rates: actual injection history, 0.06 L/min, 0.35 L/min, and 1.50 L/min. Each was modelled for a homogeneous aquifer and for an aquifer with a layer.

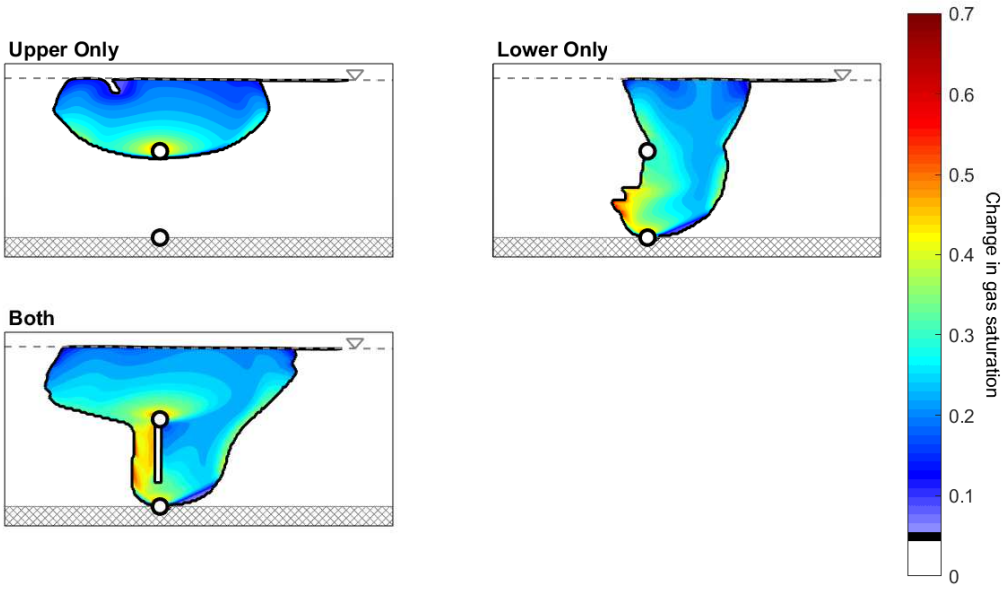

Figure 4.16: Change in gas saturation relative to the start of the injection at Day 71 of the injection for three cases of a uniform aquifer using the actual injection rate history, one using only the shallow injector, one using only the deep injector and one using both injectors simultaneously. The pre-injection water table is shown by the grey dashed line, the injectors by white circles with a black outline, the aquitard by the grey cross-hatching and the layer by the grey single hatched area.

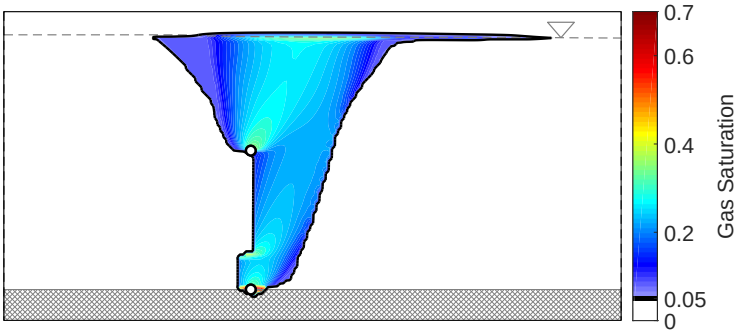

(a) Gas Saturation

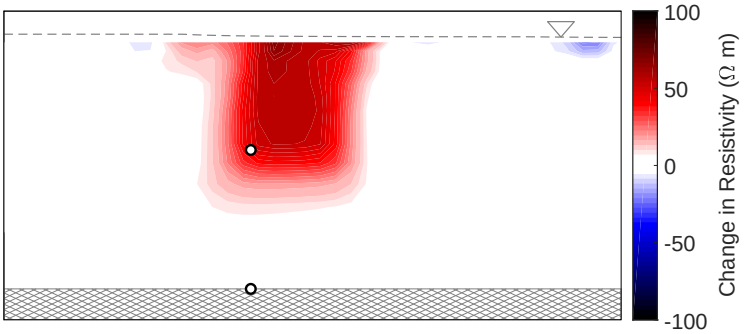

(b) ERT Response

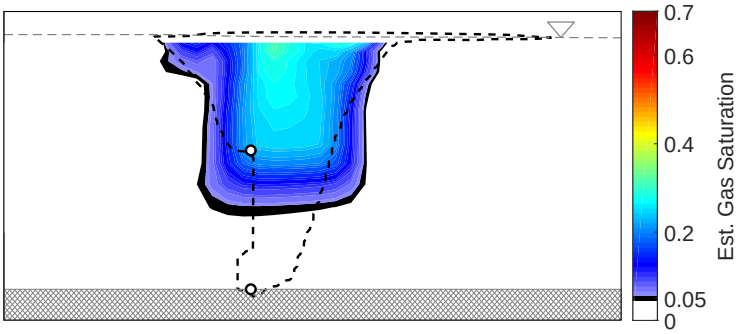

(c) Estimated change in the gas saturation from the inverted ERT data

Figure 4.17: Results from saturation model, ERT model, and the estimated saturation from ERT at Day 56 for a homogeneous aquifer.

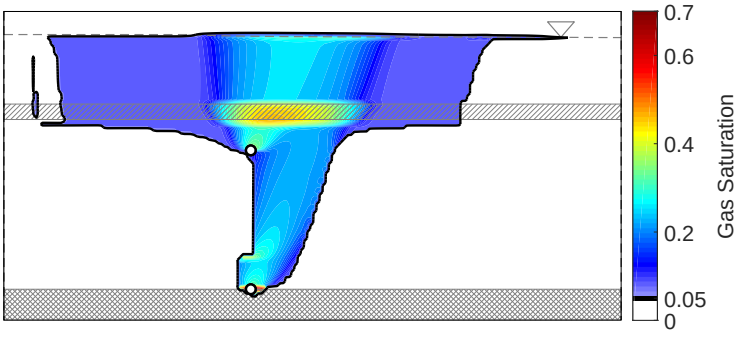

(a) Gas Saturation

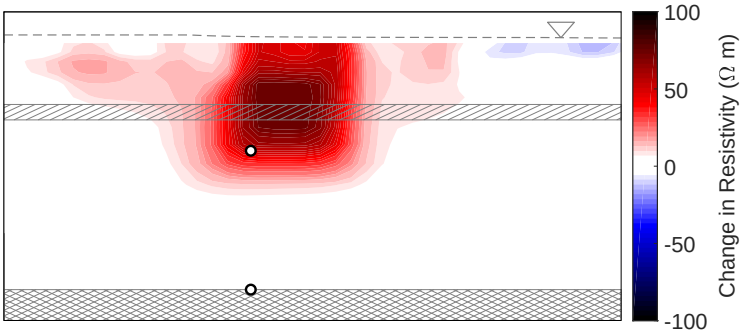

(b) ERT Response

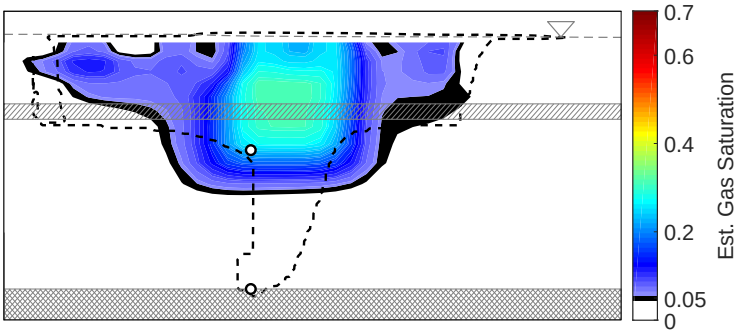

(c) Estimated change in the gas saturation from the inverted ERT data

Figure 4.18: Results from saturation model, ERT model, and the estimated saturation from ERT at Day 56 for a continuous layer ($k = 5.1 \times 10^{-13}$ m^2, $\phi = 0.31$), no entry pressure change.

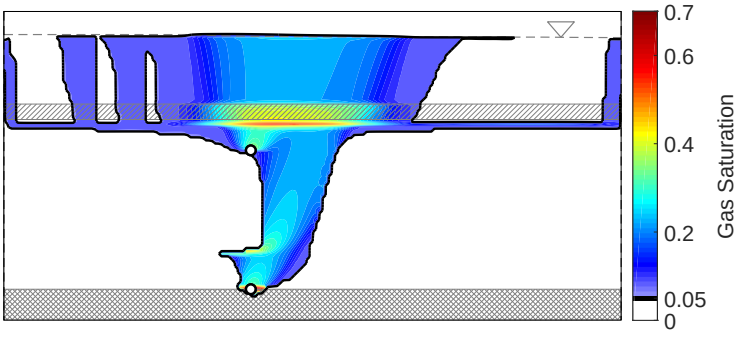

(a) Gas Saturation

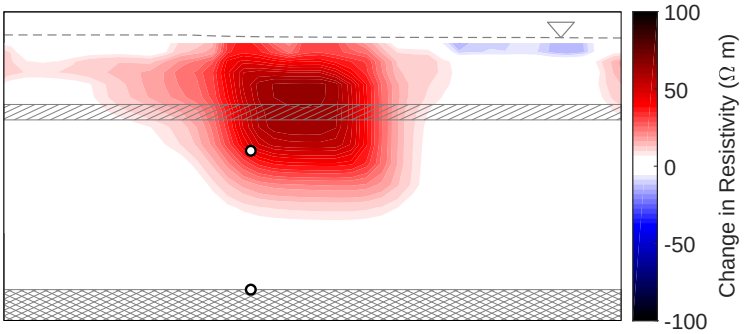

(b) ERT Response

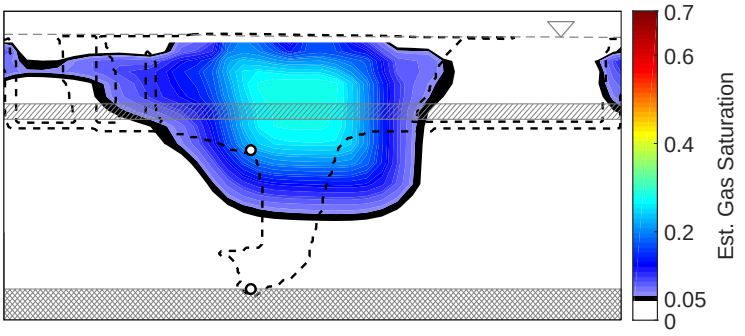

(c) Estimated change in the gas saturation from the inverted ERT data

Figure 4.19: Results from saturation model, ERT model, and the estimated saturation from ERT at Day 56 for a continuous layer ($k = 5.1 \times 10^{-13}$ m^2, $\phi = 0.31$) with a higher entry pressure ($P_c = 2.99$ kPa).

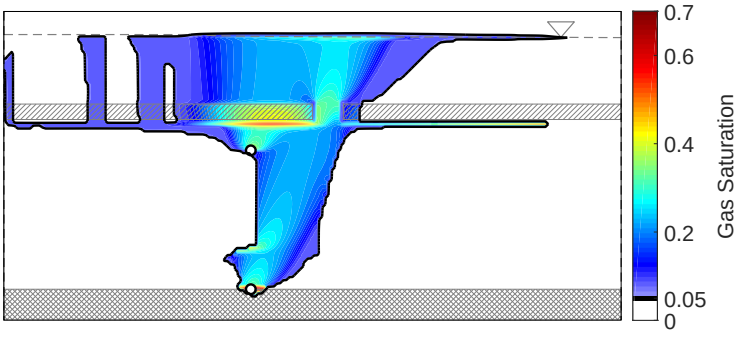

(a) Gas Saturation

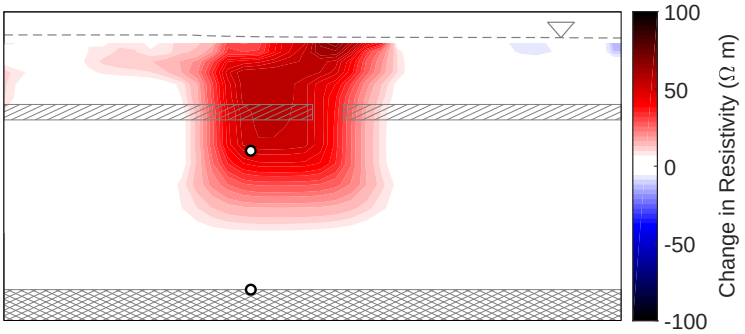

(b) ERT Response

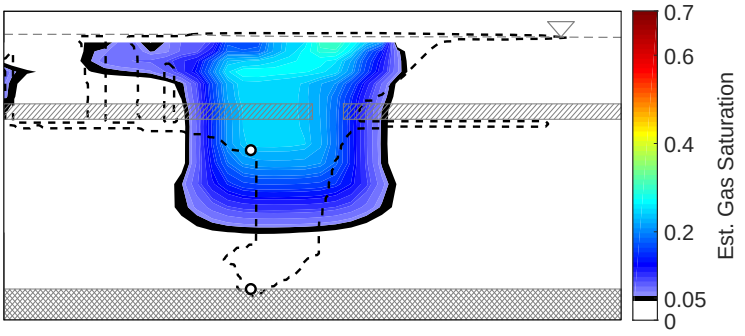

(c) Estimated change in the gas saturation from the inverted ERT data

Figure 4.20: Results from saturation model, ERT model, and the estimated saturation from ERT at Day 56 for a discontinuous layer ($k = 5.1 \times 10^{-13}$ m^2, $\phi = 0.31$) with a higher entry pressure ($P_c = 2.99$ kPa), discontinuous from 2 m to 3 m.

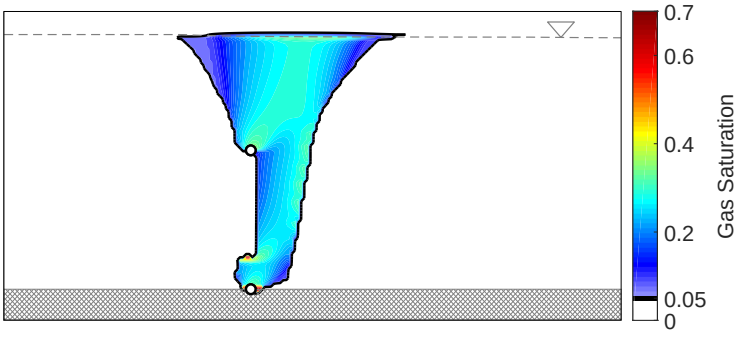

(a) Gas saturation

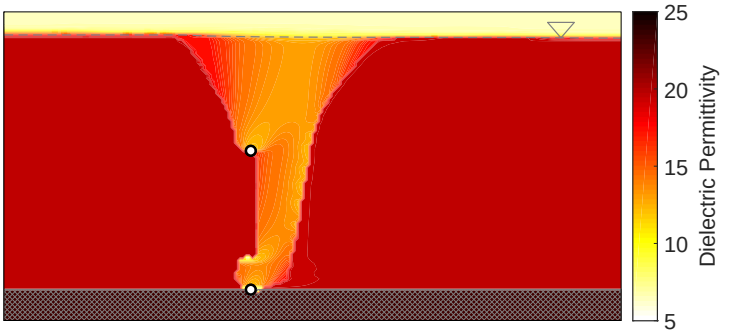

(b) Relative Permittivity

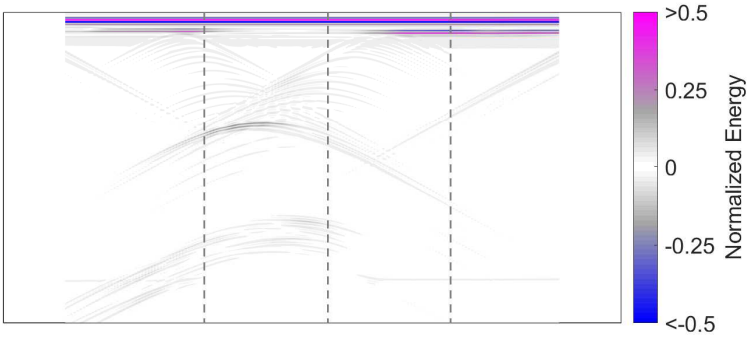

(c) Normalized GPR Amplitude

Figure 4.21: Results from saturation model and GPR model, as well as the dielectric permittivity distribution at Day 37 for a homogeneous aquifer. The black dashed lines show the locations used for the time-lapse plots.

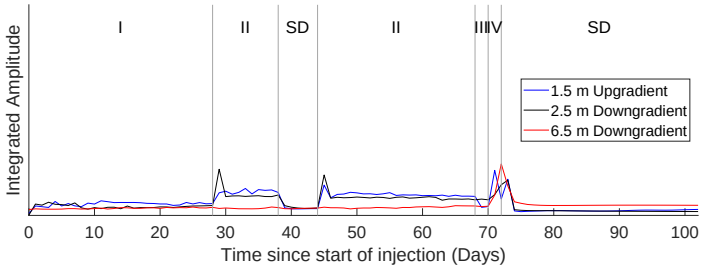

(a) Integrated normalized amplitude

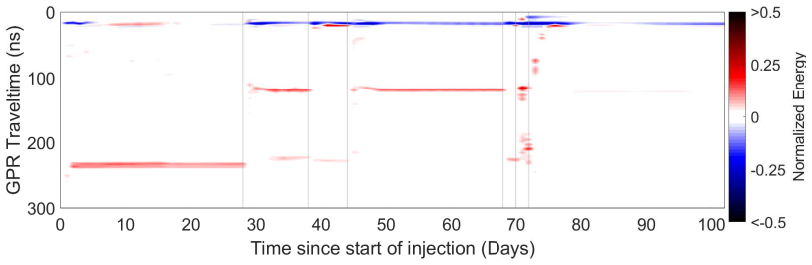

(b) Trace 1.5 m upgradient of the injector

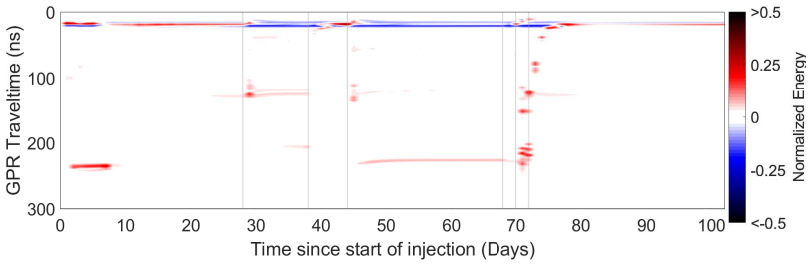

(c) Trace 2.5 m downgradient of the injector

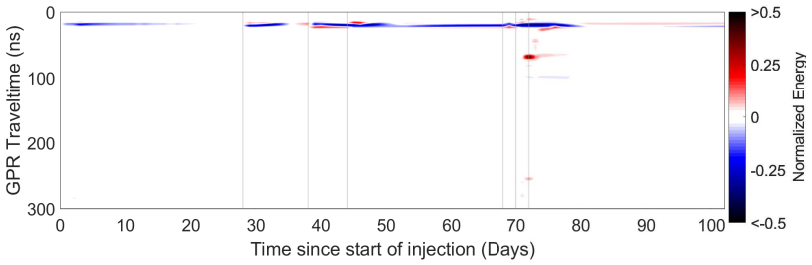

(d) Trace 6.5 m downgradient of the injector

Figure 4.22: Plot of the integrated normalized enveloped amplitude from the layer between 50 ns and 150 ns over the modelled period, as well as the change from background of three traces over the course of the modelling in a homogeneous aquifer.

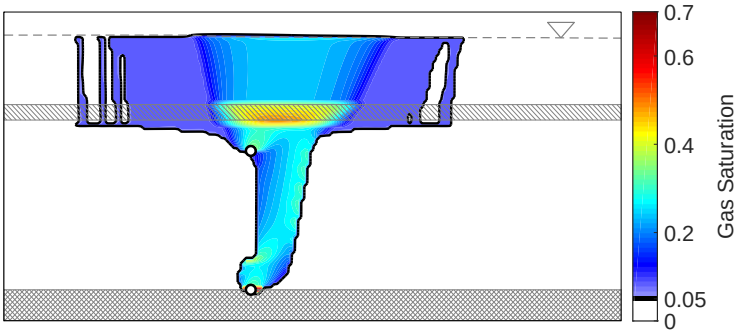

(a) Gas saturation

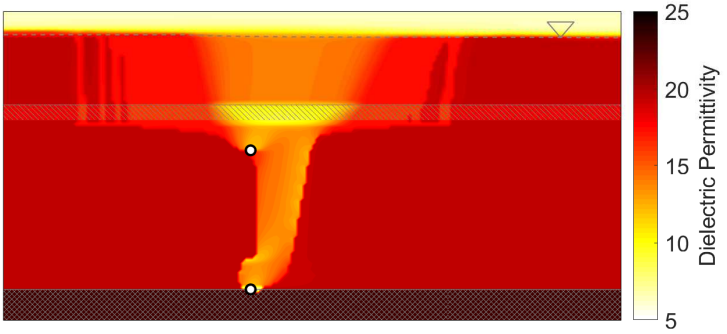

(b) Relative Permittivity

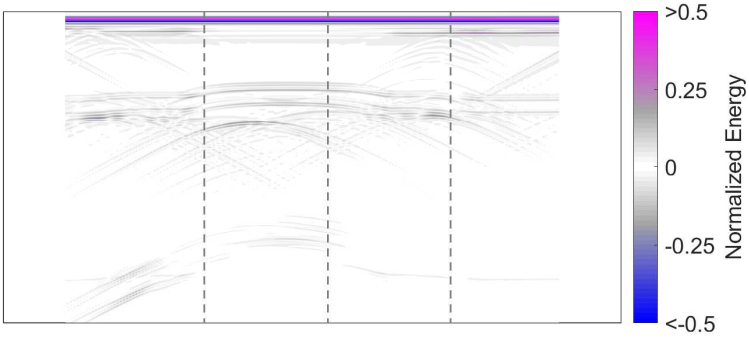

(c) Normalized GPR Amplitude

Figure 4.23: Results from saturation model and GPR model, as well as the dielectric permittivity distribution at Day 37 for a continuous layer ($k = 5.1 \times 10^{-13}$ m^2, $\phi = 0.31$), no entry pressure change. The black dashed lines show the locations used for the time-lapse plots.

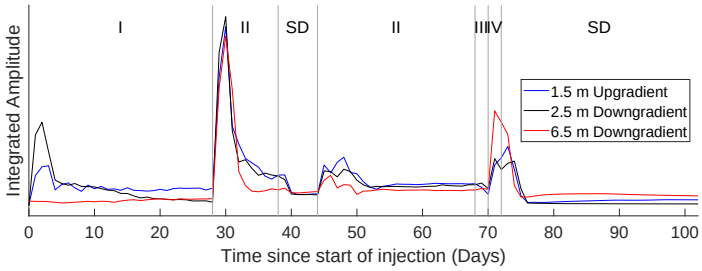

(a) Integrated normalized amplitude

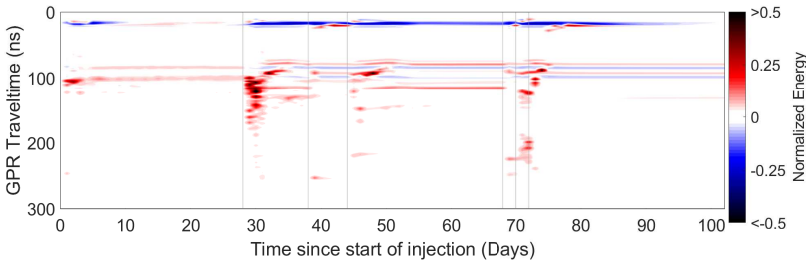

(b) Trace 1.5 m upgradient of the injector

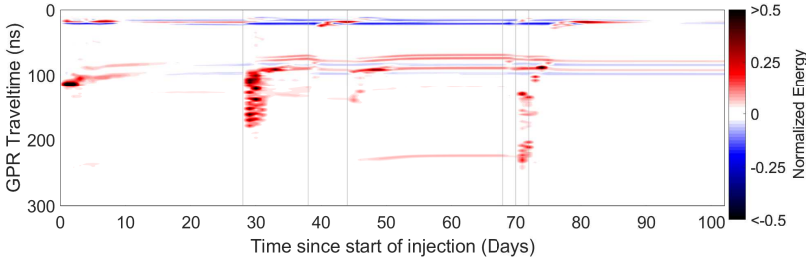

(c) Trace 2.5 m downgradient of the injector

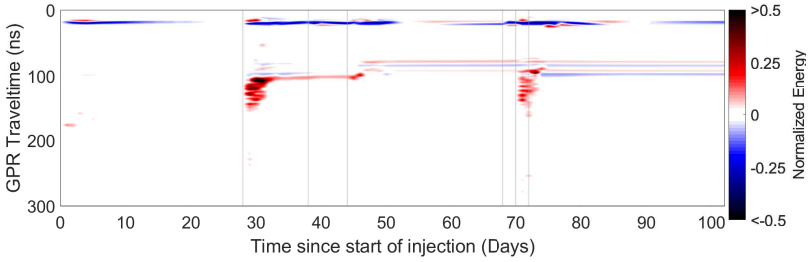

(d) Trace 6.5 m downgradient of the injector

Figure 4.24: Plot of the integrated normalized enveloped amplitude from the layer between 50 ns and 150 ns over the modelled period, as well as the change from background of three traces over the course of the modelling in a homogeneous aquifer with a continuous layer ($k = 5.1 \times 10^{-13}$ m^2, $\phi = 0.31$), no entry pressure change.

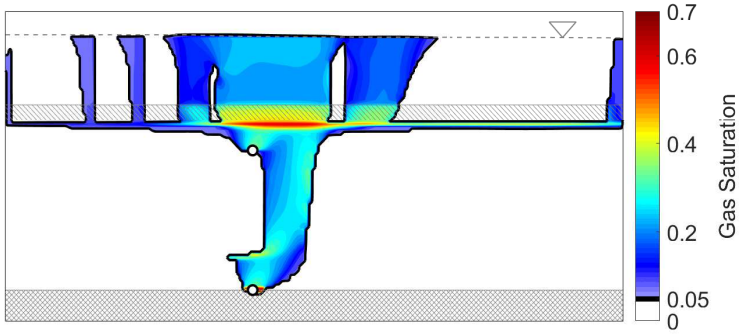

(a) Gas saturation

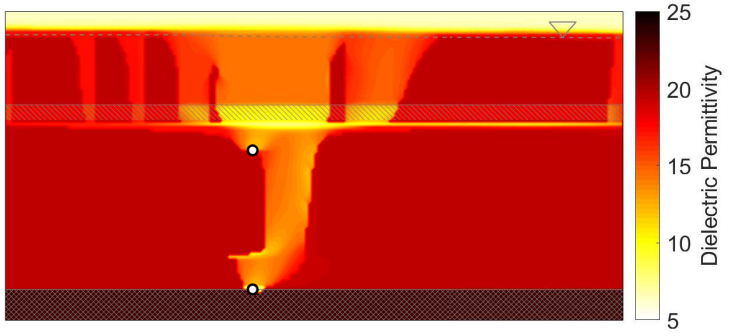

(b) Relative Permittivity

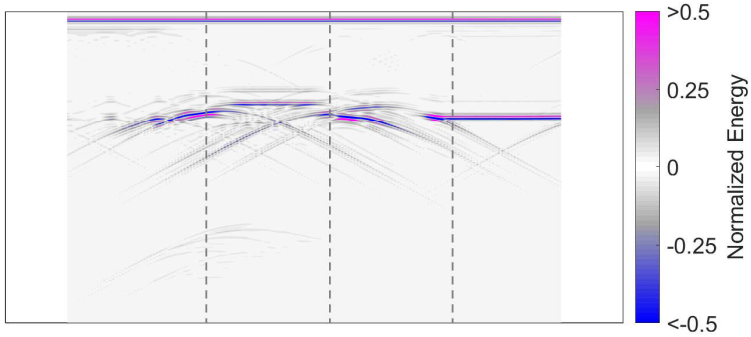

(c) Normalized GPR Amplitude

Figure 4.25: Results from saturation model and GPR model, as well as the dielectric permittivity distribution at Day 37 for a continuous layer ($k = 5.1 \times 10^{-13}$ m^2, $\phi = 0.31$) with a higher entry pressure ($P_c = 2.99$ kPa). The black dashed lines show the locations used for the time-lapse plots.

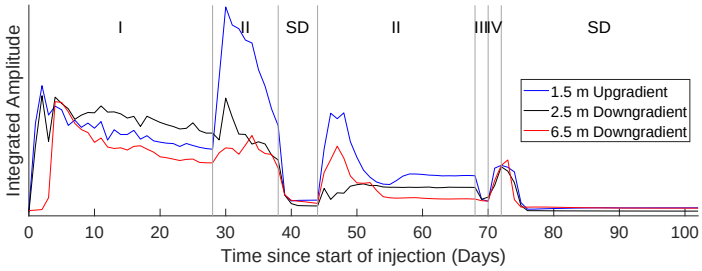

(a) Integrated normalized amplitude

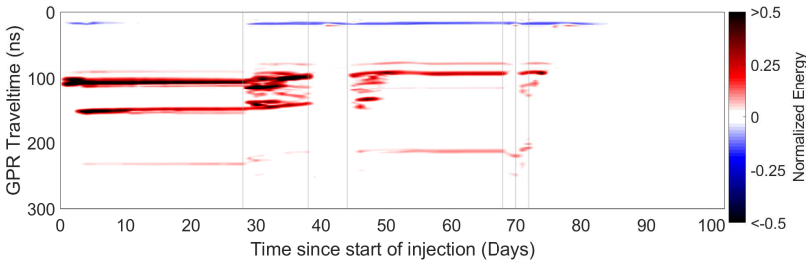

(b) Trace 1.5 m upgradient of the injector

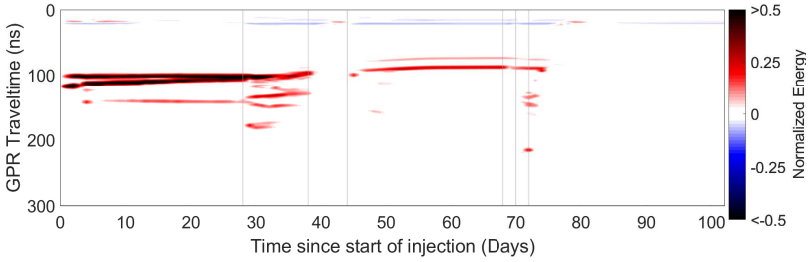

(c) Trace 2.5 m downgradient of the injector

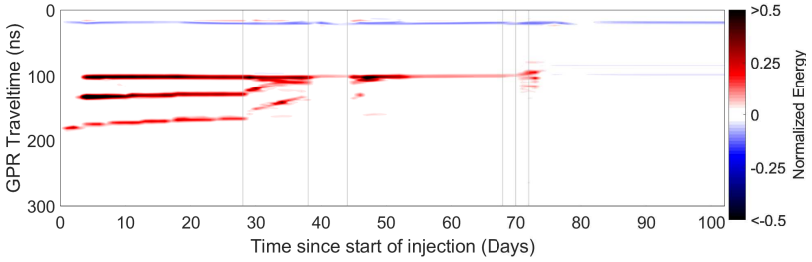

(d) Trace 6.5 m downgradient of the injector

Figure 4.26: Plot of the integrated normalized enveloped amplitude from the layer between 50 ns and 150 ns over the modelled period, as well as the change from background of three traces over the course of the modelling in a homogeneous aquifer with a continuous layer ($k = 5.1 \times 10^{-13}$ m^2, $\phi = 0.31$) with a higher entry pressure ($P_c = 2.99$ kPa).

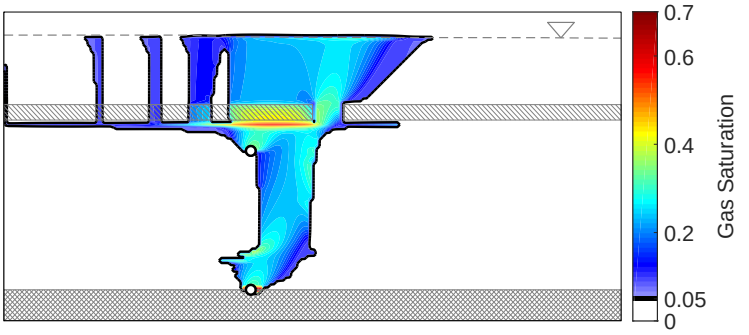

(a) Gas saturation

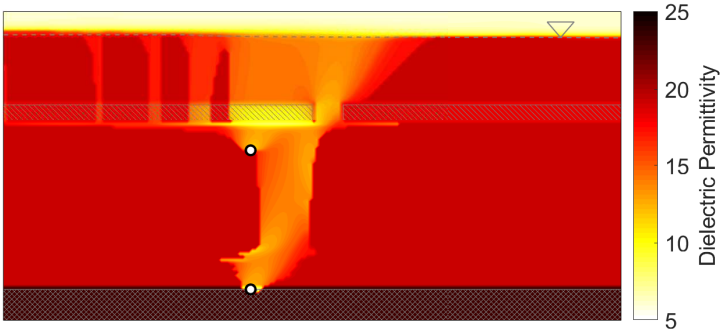

(b) Relative Permittivity

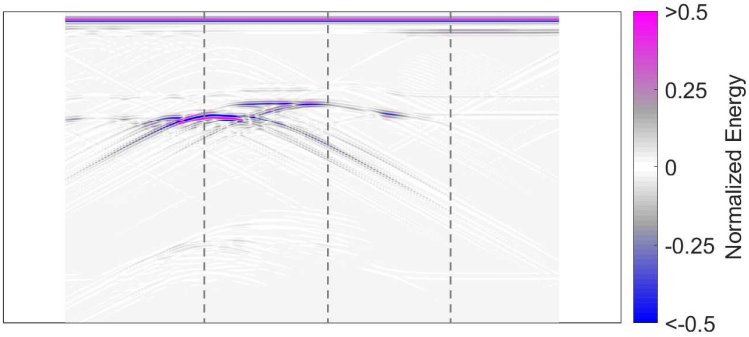

(c) Normalized GPR Amplitude

Figure 4.27: Results from saturation model and GPR model, as well as the dielectric permittivity distribution at Day 37 for a discontinuous layer ($k = 5.1 \times 10^{-13}$ m^2, $\phi = 0.31$) with a higher entry pressure ($P_c = 2.99$ kPa), discontinuous from 2 m to 3 m. The black dashed lines show the locations used for the time-lapse plots.

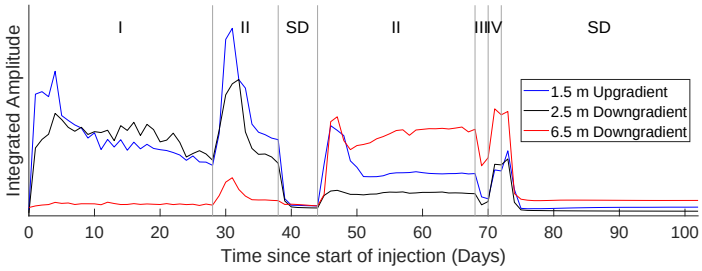

(a) Integrated normalized amplitude

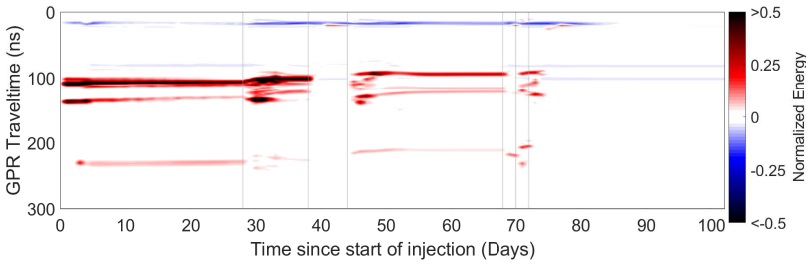

(b) Trace 1.5 m upgradient of the injector

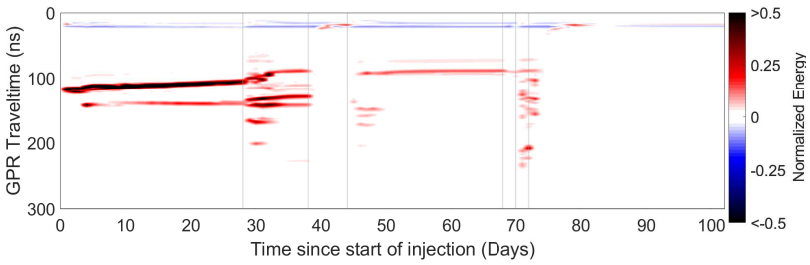

(c) Trace 2.5 m downgradient of the injector

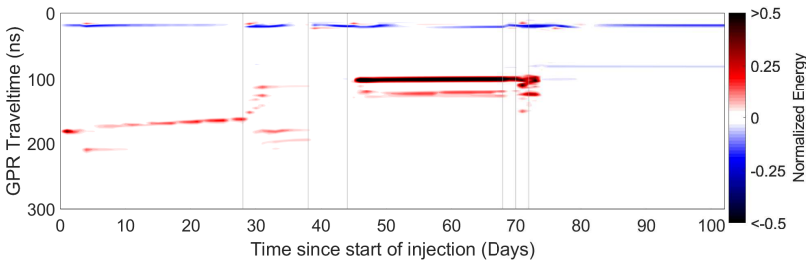

(d) Trace 6.5 m downgradient of the injector

Figure 4.28: Plot of the integrated normalized enveloped amplitude from the layer between 50 ns and 150 ns over the modelled period, as well as the change from background of three traces over the course of the modelling in a homogeneous aquifer with a discontinuous layer ($k = 5.1 \times 10^{-13}$ m^2, $\phi = 0.31$) with a higher entry pressure ($P_c = 2.99$ kPa), discontinuous from 2 m to 3 m.

Chapter 5

Discussion and Conclusions

Geophysical methods have long been a tool used in tracking immiscible-phase contaminants, such as dense non-aqueous phase liquids and gas-phase contaminants (e.g., Brewster & Annan, 1994; Brewster et al., 1995; Hwang et al., 2008; Tomlinson et al., 2003). However, the relative utility of ERT and GPR to monitor a transient gas-phase injected into an unconfined aquifer, simulating a methane leakage event from a point source, remain unclear. Although Steelman et al. (2017) reported field observations of ERT and GPR responses during a controlled methane leakage experiment in the Borden aquifer, it was unclear which physical properties of the groundwater flow system were primarily responsible for the laterally extensive and episodic distribution of gas in the subsurface observed by the geophysical techniques.

Early investigations into the behaviour of immiscible-phase liquids released in the Borden Aquifer (e.g., Brewster et al., 1995; Broholm, Feenstra, & Cherry, 1999; Kueper, Redman, Starr, Reitsma, & Mah, 1993) showed the preferential accumulation of these dense fluids along thin assemblages of coarser grained, well-sorted sand overlying finer grained sand layers. These studies confirmed that dense immiscible fluids would migrate vertically downward, accumulate and spread laterally along subtle depositional boundaries. Here, centimetre scale layers of coarser sand would act as preferential pathways, distributing the fluids away from the source. D. A. Thomson (2004) showed that these sand layers possessed varying permeability effectively resulting in a heterogeneous flow field. These variations in permeability, while negligible for single phase flow (i.e., groundwater), were more than sufficient to affect multi-phase flow. This subtle heterogeneity was responsible for the spatially complex distribution of NAPL and dissolved-phase contaminants in the

Borden aquifer (e.g., Laukonen, Parker, & Cherry, 2000).

A series of physically-based numerical simulations were carried out to evaluate the utility of time-lapse ERT and GPR methods in the detection of highly mobile gas released under pressure within an unconfined aquifer. Model scenarios were defined using field data and insights gained through the Borden Methane Injection (BMI) Experiment (Cahill et al., 2017) and were used to evaluate the physical properties and geometric controls on the evolution of the methane gas plume. Gas-phase modelling showed that the evolution of the gas-phase plume would be variably impacted by changes in anisotropy, groundwater velocity, moderate permeability contrasts, layer thickness, and geometry, with more marked impacts associated with changes in air-entry entry pressure of lower permeability layers within the aquifer. Without changes in entry pressure between two layers, gas-phase accumulations typically did not exhibit sharp boundaries (i.e., changes in saturation). Instead, the gas is smeared, forming a single plume spread over a larger area. This result is consistent with previous immiscible-phase field experiments which show pooling of fluids along permeability contrasts. However, when entry pressure changes are present between two layers, the gas accumulates along the boundary and forms laterally extensive pools. Once gas reaches a pressure higher than the entry pressure of the confining layer or when a discontinuity is reached, the gas migrates upwards via buoyancy resulting in gas hotspots effluxing to the vadose zone. The characteristics of vertical preferential pathways and gas hotspots along the water table interface depended primarily on the severity of the permeability contrast, air-entry pressure variations, and layer discontinuities; although less dominant factors such as groundwater velocity and injection configuration contributed to the formation of hotspots.

Numerical simulations showed that the inclusion of vertical permeability barriers to flow (e.g., vertical permeability contrasts, increasing layer thickness, anisotropy) or a component of horizontal groundwater flow increased the gas retention within the aquifer compared to a homogeneous, weakly anisotropic scenario. The temporary shut-down in gas injection was also shown to have a hysteretic effect on the gas concentrations and its distribution (i.e., lateral mobility) within the aquifer, which again affected gas retention within the aquifer.

Insights gained through these numerical flow simulations were consistent with the interpreted methane migration and behaviour in an unconfined shallow aquifer (e.g., Cahill et al., 2018, 2017; Steelman et al., 2017). Both the modelling and the BMI Experiment demonstrated the role of geologic structures, in the form of thin lenses of sand of varying permeability, as having a substantial impact on the migration paths of methane. Both

studies showed that a portion of the injected methane escaped to the atmosphere while the remainder accumulated in the subsurface. Both the numerical and field results showed that changes in the methane injection rate, particularly a temporary shut down of the injection, affected the migration of the methane; however, perturbations in the lateral extent combined with rapid accumulation or dissipation of gas within the aquifer were not replicated in the numerical models. Therefore, these discrepancies were likely caused by processes independent of the groundwater flow properties (e.g., recharge, barometric pressure variations, temperature) (e.g., Terry et al., 2016).

Electrical resistivity tomography (ERT) was effective at monitoring bulk gas accumulation primarily around the shallow injector but was not able to resolve thin pools extending beyond the main bulb or vertical preferential pathways. This result is not all that surprising considering the inherent limitations of electrical resistivity methods with respect to resolution with increased depth. The inability to detect changes at depth could be overcome by increasing the electrode spacing (Revil et al., 2012); however, this would come at the expense of resolution of spatially limited zones of desaturation. It should be noted that the height of the model blocks increases with depth, which, when combined with relatively low levels of desaturation, results in a small response to the bulk resistivity. Similarly, model parametrization could have impacted the detection of thin elements; for instance, lateral discretization in the hydrogeologic modelling was 10 cm, while in the forward geophysical modelling of the ERT response it was 25 cm, resulting in a smoothed representation in the actual gas distribution. Further modelling using a more sophisticated forward modelling scheme may yield greater consistency between the gas saturations calculated from the flow model and the inverted geophysical model. Although the modelled ERT response to the gas distribution in the subsurface was only effective at detecting the primary gas bulb, there was limited evidence of an electrical response associated with the establishment of vertical preferential pathways farther away. This observation is consistent with Steelman et al. (2017), which showed both a gas bulb and a thin zone of higher resistivity farther down-gradient. However, ERT remains relatively insensitive to gas injection in both the field experiment and modelled scenarios.

As it stands, the modelled scenarios demonstrate that ERT has the capacity to show where gas might be venting to the vadose zone and provide a good qualitative measure of the position of the main plume assuming limited lateral migration has occurred. However, as the geology becomes more complex, resulting in higher lateral mobility and spreading along thin pools, ERT quickly becomes a less effective imaging tool. The spatially complex distribution together with the numerical simulations indicate that the ERT will most likely

be moderately useful in the field, especially if the goal is to resolve individual migration pathways.

In contrast, the GPR was highly sensitive to the accumulation of gas beneath permeability contrasts and responded to a wide range of dielectric contrasts induced by the movement of gas in the subsurface; thin pools beneath capillary barriers extending beyond the limits of the primary gas plume were effectively detected by GPR. However, there were some differences between the modelled scenarios and the results of the BMI Experiment (Steelman et al., 2017). The diffractions that defined the edges of the plume in the modelled GPR response were not readily identified in the field, and no notable pull-up in reflection events was observed during the field experiment. Steelman et al. (2017) also noted that methane primarily migrated down-gradient, and to much farther distances than observed in these simulations. The results of the BMI Experiment are best approximated by the response associated with an increase in the entry pressure at a permeability barrier. The main difference being that instead of a single layer, the field results indicate multiple lenses of short lateral extent trapped gas in pockets which resulted in the more spatially distributed increase in signal reflectivity. The build-up and spill over of methane from one layer to another, analogous to the pattern of DNAPL migration observed by Brewster and Annan (1994), also showed significant lateral migration; these numerical simulations demonstrated the potential for high lateral mobility of a pressurized methane source in an unconfined aquifer characterized by subtle permeability contrasts with increased capillary pressure. The mix of areas of high and low gas concentrations (Cahill et al., 2018), together with the spatially variable reflectivity distribution (Steelman et al., 2017), indicates that the gas was largely directed through a complex network of interbedded sand layers, acting as preferential pathways of variable length scales.

This modelling was completed under the assumption that the bulk hydraulic properties of soil would adequately describe the movement of methane gas in the aquifer, and that the resulting model would be sufficient to evaluate the essential geophysical responses associated with gas migration in the aquifer. Although the scenarios used to evaluate the geophysical response to methane migration were somewhat simplistic, they demonstrate the importance of heterogeneity (i.e., layers with variable permeability and capillary pressure) on the evolution of a methane gas plume emanating from a wellbore depicted in this study as two point sources. Here, the lateral extent of gas migration relative to the depth of the injection was quite substantial (2–3 times the depth). Other numerical simulations of wellbore leakage in an unconfined aquifer by Roy et al. (2016) suggest that gas leakage would simply migrate upwards due to buoyancy and eventually escape to the atmosphere.

Although their study examined potential reactions within the aquifer, which could contribute to methane oxidation, Cahill et al. (2018) showed that methane would persist in the aquifer, showing little signs of microbial degradation one year after the injection commenced.

A well constrained plume conceptualization hinges on an accurate understanding of the distribution of the gas-phase in the subsurface. While ERT results were generally consistent with the BMI experimental results, the numerial simulations confirm that ERT is only moderately effective at characterizing methane leakage from a well, especially if heterogeneity contributes to lateral migration. Meanwhile, GPR would be a much more effective tool in tracking the migration of gas along preferential pathways, assuming the gas is not constrained to a bulb with limited lateral mobility. The BMI Experiment suggests that both geophysical methods could be applicable in monitoring the evolution and migration of methane plumes depending on the state of the plume's evolution. In addition, this modelling, despite its simplicity, does confirm that application of these geophysical methods to evaluate the migration and distribution of fugitive methane in unconfined aquifers is tenable.

Questions remain following this modelling. The first question is the efficacy of these methods in borehole scenarios. How will these methods operate in the boreholes and will they image zones of gas accumulation more or less accurately than surface methods? Secondly, the question of site complexity remains somewhat unresolved. How will multiple structures on different length scales interact with the gas-phase flow, and how will that in turn impact the geophysical response of these methods? Further modelling could provide a clearer response to these questions, but field scale studies will ultimately be needed to decide if these methods are useful. This study, coupled with the BMI Experiment, give a theoretical basis for the application GPR and ERT in the detection of fugitive methane and these studies provide a starting point in developing a response to this serious environmental issue.

References

Ain-Lhout, F., Boutaleb, S., Diaz-Barradas, M. C., Jauregui, J., & Zunzunegui, M. (2015). Monitoring the evolution of soil moisture in root zone system of Argania spinosa using electrical resistivity imaging. *Agricultural Water Management*, *164*(September), 158–166. Retrieved from http://dx.doi.org/10.1016/j.agwat.2015.08.007 doi: 10.1016/j.agwat.2015.08.007

Andres, K. G., & Canace, R. (1984). Use of the electrical resistivity technique to delineate a hydrocarbon spill in the coastal planes deposit of New Jersey. In *Conference on petroleum hydrocarbons and organic chemicals in groundwater* (pp. 188–197). American Petroleum Instituition.

Annan, A. P. (2005). GPR methods for hydrogeological studies. In *Hydrogeophysics* (pp. 185–213).

Annan, A. P. (2009). Electromagnetic principles of ground penetrating radar. In H. M. Jol (Ed.), *Ground penetrating radar: Theory and applications* (pp. 3–40). Amsterdam, The Netherlands: Elsevier B.V.

Archie, G. E. (1942). The electrical resistivity log as an aid in determining some reservoir characteristics. In *Petroleum technology* (pp. 54–62). Dallas, TX.

Atekwana, E. A., & Atekwana, E. A. (2010). Geophysical signatures of microbial activity at hydrocarbon contaminated sites: A review. *Surveys in Geophysics*, *31*, 247–283. doi: 10.1007/s10712-009-9089-8

Attia, A. M. (2005). Effects of petrophysical rock properties on tortuosity factor. *Journal of Petroleum Science and Engineering*, *48*(3-4), 185–198. doi: 10.1016/j.petrol.2005.06.012

Barker, R. (1989). Depth of investigation of collinear symmetrical four-electrode arrays. *Geophysics*, *54*(8), 1031–1037. doi: 10.1190/1.1442728

Bass, D. H., Hastings, N. A., & Brown, R. A. (2000). Performance of air sparging systems: A review of case studies. *Journal of Hazardous Materials*, *72*(2-3), 101–119. doi: 10.1016/S0304-3894(99)00136-3

Binley, A., Hubbard, S. S., Huisman, J. a., Revil, A., Robinson, D. A., Singha, K., &

Slater, L. (2015). The emergence of hydrogeophysics for improved understanding of subsurface processes over multiple scales. *Water Resources Research*, 3837–3866. doi: 10.1002/2015WR017016

Bret-Rouzaut, N., & Favennec, J.-P. (2011). Oil and gas exploration and production. In *Oil and gas exploration and production: Reserves, costs, contracts* (3rd ed., pp. 61–91). Paris, France: Technip.

Brewster, M. L., & Annan, A. P. (1994). Ground-penetrating radar monitoring of a controlled DNAPL release : 200 MHz radar. *Geophysics*, *59*(8), 1211–1221. doi: 10.1190/1.1443679

Brewster, M. L., Annan, A. P., Greenhouse, J. P., Kueper, B. H., Olhoeft, G. R., Redman, J. D., & Sander, K. A. (1995). Observed migration of a controlled DNAPL release by geophysical methods. *Ground Water*, *33*(6), 977–987.

Broholm, K., Feenstra, S., & Cherry, J. A. (1999). Solvent release into a Sandy Aquifer. 1. Overview of source distribution and dissolution behavior. *Environmental Science and Technology*, *33*(5), 681–690. doi: 10.1021/es980097d

Brooks, R. H., & Corey, A. (1964). Hydraulic properties of porous media. *Hydrology Papers, Colorado State University. Fort Collins CO*, *3*(3), 27 pgs. doi: citeulike-article-id: 711012

Burger, H. R., Sheehan, A. F., & Jones, C. H. (2006). *Introduction to Applied Geophysics*. New York, N.Y.: W. W. Norton & Company Inc.

Cahill, A. G., Parker, B. L., Mayer, B., Mayer, K. U., & Cherry, J. A. (2018). High resolution spatial and temporal evolution of dissolved gases in groundwater during a controlled natural gas release experiment. *Science of the Total Environment*, *622-623*, 1178–1192. Retrieved from https://doi.org/10.1016/j.scitotenv.2017.12.049 doi: 10.1016/j.scitotenv.2017.12.049

Cahill, A. G., Steelman, C. M., Forde, O., Kuloyo, O., Emil Ruff, S., Mayer, B., ... Parker, B. L. (2017). Mobility and persistence of methane in groundwater in a controlled-release field experiment. *Nature Geoscience*, *10*(4), 289–294. doi: 10.1038/ngeo2919

Chen, X., & Slater, L. (2015). Gas bubble transport and emissions for shallow peat from a northern peatland: The role of pressure changes and peat structure. *Water Resources Research*, *51*(1), 151–168. doi: 10.1002/2013WR014979.Reply

Comas, X., & Slater, L. (2007). Evolution of biogenic gases in peat blocks inferred from noninvasive dielectric permittivity measurements. *Water Resources Research*, *43*(5), 1–10. doi: 10.1029/2006WR005562

Comas, X., Slater, L., & Reeve, A. (2005). Spatial variability in biogenic gas accumulations in peat soils is revealed by ground penetrating radar (GPR). *Geophysical Research Letters*, *32*(8), 1–4. doi: 10.1029/2004GL022297

Council of Canadian Academies. (2014). *Environmental Impacts of Shale Gas Extraction*

in Canada.

Daily, W., Ramirez, A., Binley, A., & LaBrecque, D. J. (2005). Electrical resistance tomography - Theory and practice. In D. K. Butler (Ed.), *Near surface geophysics* (pp. 525–550). Tulsa, OK: Society of Exploration Geophysicists.

Daniels, J. J., Roberts, R., & Vendl, M. (1992). Site studies of ground penetrating radar for monitoring petroleum product contaminants. In *Symposium of the application of geophysics to engineering and nvironmental problems* (pp. 597–609).

Das, B. M. (2008). *Advanced Soil Mechanics* (3rd ed.). New York, NY. doi: 10.1029/EO066i042p00714-02

Davis, J. L., & Annan, a. P. (1989). Ground-Penetrating Radar for High-Resolution Mapping of Soil and Rock Stratigraphy. *Geophysical Prospecting*, *39*, 531–551. doi: 10.1111/j.1365-2478.1989.tb02221.x

Dey, A., & Morrison, H. (1976). Resistivity Modeling for Arbitrarily Shaped Two-Dimensional Structures. *Geophysics*, *41*(1), 62. doi: 10.1190/1.1440608

Dobrin, M. B., & Savit, C. H. (1988). *Introduction to geophysical prospecting* (4th ed.). McGraw-Hill Book Company.

Doetsch, J., Fiandaca, G., Auken, E., Christiansen, A. V., & Cahill, A. G. (2015). Field-scale time-domain spectral induced polarization monitoring of geochemical changes induced by injected CO2 in a shallow aquifer. *Geophysics*, *16*(2), 10294. Retrieved from http://library.seg.org/doi/abs/10.1190/geo2014-0315.1?journalCode=gpysa7 doi: 10.1190/geo2014-0315.1

Doveton, J. H. (1986). *Log analysis of subsurface geology: Concepts and computer methods*. John Wiley & Sons, Inc.

Everett, M. E. (2013). *Near-Surface Applied Geophysics*. Cambridge: Cambridge University Press.

Fetter, C. W. (1992). *Contaminant hydrogeology*. New York, N.Y.: Macmillan Publishing Company.

Friedman, S. P. (2005). Soil properties influencing apparent electrical conductivity: A review. *Computers and Electronics in Agriculture*, *46*(1-3 SPEC. ISS.), 45–70. doi: 10.1016/j.compag.2004.11.001

Gasperikova, E., & Hoversten, G. M. (2006). A feasibility study of nonseismic geophysical methods for monitoring geologic sequestration. *The Leading Edge*, *25*(10), 1282–1288. Retrieved from http://library.seg.org/doi/abs/10.1190/1.2360621 doi: 10.1190/1.2360621

Gasperikova, E., & Hoversten, G. M. (2008). Gravity monitoring of CO[sub 2] movement during sequestration: Model studies. *Geophysics*, *73*(6), WA105. doi: 10.1190/1.2985823

Hwang, Y. K., Endres, A. L., Piggott, S. D., & Parker, B. L. (2008). Long-term

ground penetrating radar monitoring of a small volume DNAPL release in a natural groundwater flow field. *Journal of Contaminant Hydrology*, *97*(1-2), 1–12. doi: 10.1016/j.jconhyd.2007.11.004

Jackson, R. B., Vengosh, A., Darrah, T. H., Warner, N. R., Down, A., Poreda, R. J., ... Karr, J. D. (2013). Increased stray gas abundance in a subset of drinking water wells near Marcellus shale gas extraction. *Proceedings of the National Academy of Sciences of the United States of America*, *110*(28), 11250–5. Retrieved from http://www.pnas.org/cgi/content/long/110/28/11250 doi: 10.1073/pnas.1221635110

Johansson, S., Rosqvist, H., Svensson, M., Dahlin, T., & Leroux, V. (2011). An alternative methodology for the analysis of electrical resistivity data from a soil gas study. *Geophysical Journal International*, *186*(2), 632–640. doi: 10.1111/j.1365-246X.2011.05080.x

Jorgensen, D. J. (1996). The ratio method of estimating water resistivity and TDS from resistovoty logs. *Ground Water*, *34*(3), 519–522.

Kaye, G. W. C., & Laby, T. H. (1995). *Tables of physical and chemical constants* (16th ed.). Essex, England: Longman Group Limited.

Keller, G. V. (1987). Rock and Mineral Properties. In M. N. Nabighian (Ed.), *Electromagnetic methods in applied geophysics - theory: Volume 1* (pp. 13–51). Tulsa, OK: Society of Exploration Geophysicists.

Kelly, W. R., Matisoff, G., & Fisher, J. B. (1985). The effects of a gas well blow out on groundwater chemistry. *Environmental Geology and Water Sciences*, *7*(4), 205–213. doi: 10.1007/BF02509921

Kim, J., Nam, M. J., & Matsuoka, T. (2013). Estimation of CO2 saturation during both CO2 drainage and imbibition processes based on both seismic velocity and electrical resistivity measurements. *Geophysical Journal International*, *195*(1), 292–300. doi: 10.1093/gji/ggt232

Knight, R. (2001). Ground Penetrating Radar for environmental applications. *Annual Review of Earth and Planetary Sciences*.

Kovacs, T., Poulussen, D. F., & de Dios, C. (2015). *Strategies for injection of CO2 into carbonate rocks at Hontomin* (Tech. Rep.).

Kueper, B. H., & Frind, E. O. (1991). *Two-phase flow in heterogeneous porous media 2. Model application* (Vol. 27) (No. 6).

Kueper, B. H., Redman, D., Starr, R. C., Reitsma, S., & Mah, M. (1993). *A Field Experiment to Study the Behavior of Tetrachloroethylene Below the Water Table: Spatial Distribution of Residual and Pooled DNAPL* (Vol. 31) (No. 5). doi: 10.1111/j.1745-6584.1993.tb00848.x

Lassen, R. N., Sonnenborg, T. O., Jensen, K. H., & Looms, M. C. (2015). Monitoring CO2 gas-phase migration in a shallow sand aquifer using cross-borehole ground

penetrating radar. *International Journal of Greenhouse Gas Control*, *37*, 287–298. Retrieved from http://dx.doi.org/10.1016/j.ijggc.2015.03.030 doi: 10.1016/j.ijggc.2015.03.030

Laukonen, K., Parker, B., & Cherry, J. (2000). Internal characteristics of a bromide tracer zone during natural flow in the Borden aquifer, Ontario, Canada. In *Tram2000.*

Leverett, M. C. (1940). Capillary Behavior in Porous Solids. In *Petroleum technology* (pp. 152–169). Tulsa, OK.

Loke, M. H. (2002). Rapid 2D resistivity forward modelling using the finite- difference and finite-element methods. *International immunology*, *25*(6), 28.

Lumley, D. (2010). 4D seismic monitoring of CO2 sequestration. *The Leading Edge*, 150–155.

Lundegard, P., & LaBrecque, D. J. (1998). Geophysical and Hydrologic Monitoring of Air Sparging Flow Behavior: Comparison of Two Extreme Sites. *Remediation*(Summer), 59–71.

Ma, R., McBratney, A., Whelan, B., Minasny, B., & Short, M. (2011). Comparing temperature correction models for soil electrical conductivity measurement. *Precision Agriculture*, *12*(1), 55–66. doi: 10.1007/s11119-009-9156-7

Mickle, R. J. (2005). *A coupled hydrogeological-petrophysical analysis of geophysical variation in the vadose zone* (Master of Science). University of Waterloo.

Moortgat, J., Schwartz, F. W., & Darrah, T. H. (2018). Numerical Modeling of Methane Leakage from a Faulty Natural Gas Well into Fractured Tight Formations. *Groundwater*, 1–13. doi: 10.1111/gwat.12630

Neal, A. (2004). Ground-penetrating radar and its use in sedimentology: Principles, problems and progress. *Earth-Science Reviews*, *66*(3-4), 261–330. doi: 10.1016/j.earscirev.2004.01.004

Okpoli, C. C. (2013). Application of 2D Electrical Resistivity Tomography in Landfill Site: A Case Study of Iku, Ikare Akoko, Southwestern Nigeria. *Journal of Geological Research*, *895160*(8). Retrieved from http://dx.doi.org/10.1155/2013/895160 doi: 10.1155/2013/895160

Osborn, S. G., Vengosh, A., Warner, N. R., & Jackson, R. B. (2011). Methane contamination of drinking water accompanying gas-well drilling and hydraulic fracturing. *Proceedings of the National Academy of Sciences*, *108*(37), E665–E666. Retrieved from http://www.pnas.org/cgi/doi/10.1073/pnas.1109270108 doi: 10.1073/pnas.1109270108

Pearce, J., & Mittleman, D. (2002). Defining the Fresnel zone for broadband radiation. *Physical Review*, *66*(5), 1–4. doi: 10.1103/PhysRevE.66.056602

Perrodon, A. (1983). *Dynamics of oil and gas accumulations.* Pau, France: Elf Aquitaine.

Revil, A., Karaoulis, M., Johnson, T., & Kemna, A. (2012). Review: Some low-frequency

electrical methods for subsurface characterization and monitoring in hydrogeology. *Hydrogeology Journal*, *20*(4), 617–658. doi: 10.1007/s10040-011-0819-x

Rice, A. K., McCray, J. E., & Singha, K. (2018). Methane leakage from hydrocarbon wellbores into overlying groundwater: Numerical investigation of the multiphase flow processes governing migration (accepted). *Water Resources Research*.

Robinson, E. S., & Çoruh, C. (1988). *Basic Exploration Geophysics*. John Wiley & Sons, Inc.

Rosqvist, H., Leroux, V., Dahlin, T., Svensson, M., Lindsjö, M., Månsson, C.-H., & Johansson, S. (2011). Mapping landfill gas migration using resistivity monitoring. *Waste and Resource Management*, *164*(1), 3–15. doi: 10.1680/warm.2011.164.1.3

Roth, K., Schulin, R., Fluhler, H., & Attinger, W. (1990). Calibration of time domain reflectometry for water content measurement using a composite dielectric approach. *Water Resources Research*, *26*(10), 2267–2273.

Roy, N., Molson, J., Lemieux, J. M., Van Stempvoort, D., & Nowamooz, A. (2016). Three-dimensional numerical simulations of methane gas migration from decommissioned hydrocarbon production wells into shallow aquifers. *Water Resources Research*, *52*(7), 5598–5618. doi: 10.1002/2016WR018686

Royal Academy of Science. (2012). Shale gas extraction in the UK : a review of hydraulic fracturing. *Royal Academy of Engineering*(June), 76. doi: 10.1016/j.petrol.2013.04.023

Ruffet, C., Darot, M., & Guéguen, Y. (1995). Surface conductivity in rocks: a review. *Surveys in Geophysics*, *16*(1), 83–105. doi: 10.1007/BF00682714

Sandmeier, K. J. (2017). *ReflexW: Version 8.5 Windows XP/7/8/10-program for the processing of seismic, acoustic or electromagnetic reflection, refraction and transmission data* (No. 49). Karlsruhe, Germany: Sandmeier Geophysical Research.

Schout, G., Hartog, N., Hassanizadeh, S. M., & Griffioen, J. (2018). Impact of an historic underground gas well blowout on the current methane chemistry in a shallow groundwater system. *Proceedings of the National Academy of Sciences*, *115*(2), 296–301. Retrieved from http://www.pnas.org/lookup/doi/10.1073/pnas.1711472115 doi: 10.1073/pnas.1711472115

Shaw, H., & Lancaster-Jones, E. (1922). The Eötvös Torsion Balance. *Proceedings of the Physical Society of London*, *35*(1), 151. Retrieved from http://stacks.iop.org/1478-7814/35/i=1/a=319

Slater, L., Comas, X., Ntarlagiannis, D., & Moulik, M. R. (2007). Resistivity-based monitoring of biogenic gases in peat soils. *Water Resources Research*, *43*(10), 1–13. doi: 10.1029/2007WR006090

Spies, B. R. (1983). Recent developments in the use of surface electrical methods for oil and gas exploration in the Soviet Union. *Geophysics*, *48*(08), 1102–1112. doi:

10.1190/1.1441532

Stanfill, D. F. I., & McMillan, K. S. (1985). Radar mapping of gasoline and other hydrocarbons in the ground: Management of uncontrolled hazardous waste sites. *Hmcri*, 269–274.

Steelman, C., Klazinga, D., Cahill, A. G., Endres, A. L., & Parker, B. L. (2017). Monitoring the migration and evolution of methane gas injected into an unconfined sandy aquifer using time-lapse GPR and ERT. *Journal of Contaminant Hydrology*, *205*, 12–24.

Terry, N., Slater, L., Comas, X., Reeve, A., Schäfer, K. V. R., & Yu, Z. (2016). Free phase gas processes in a northern peatland inferred from autonomous field-scale resistivity imaging. *Water Resources Research*, *52*, 1–23. doi: 10.1002/2015WR018111

The MathWorks, I. (2010). Cluster analysis. In *Statistics toolbox: user's guide* (R2010a ed.).

Thomson, D. A. (2004). *Influence of grain size variability and sedimentology on solvent DNAPL distribution in the Borden aquifer* (Master's). University of Waterloo.

Thomson, N. R., & Johnson, R. L. (2000). Air distribution during in situ air sparging: An overview of mathematical modeling. *Journal of Hazardous Materials*, *72*(2-3), 265–282. doi: 10.1016/S0304-3894(99)00143-0

Tomlinson, D. W., Thomson, N. R., Johnson, R. L., & Redman, J. D. (2003). Air distribution in the Borden aquifer during in situ air sparging. *Journal of Contaminant Hydrology*, *67*(1-4), 113–132. doi: 10.1016/S0169-7722(03)00070-6

Tsui, F., & Matthews, S. L. (1997). Analytical modelling of the dielectric properties of concrete for subsurface radar applications. *Construction and Building Materials*, *11*(3), 149–161.

U. S. Exchange Delegation in Exploration Geophysics. (1974). Exploration geophysics in the USSR. *Geophysics*, *39*, 671–711.

U. S. Exchange Delegation in Petroleum Geophysics. (1966). Tour of petroleum geophysics activities in the USSR. *Geophysics*, *31*(3), 630–637.

Unger, A. J. A., Sudicky, E. A., & Forsyth, P. A. (1995). Mechanisms Controlling Vacuum Extraction Coupled With Air Sparging for Remediation of Heterogeneous Formations Contaminated by Dense Nonaqueous Phase Liquids. *Water Resources Research*, *31*(8), 1913–1925. doi: 10.1029/95WR00172

Vidic, R. D., Brantley, S. L., Vandenbossche, J. M., Yoxtheimer, D., & Abad, J. D. (2013). Impact of Shale Gas Development on Regional Water Quality. *Science*, *340*(6134), 1235009–1235009. Retrieved from http://www.sciencemag.org/cgi/doi/10.1126/science.1235009 doi: 10.1126/science.1235009

Walker, J. (2011). *Fundamentals of Physics* (9th ed.). Hoboken, NJ: John Wiley & Sons, Inc.

Walton, K. M. (2013). *On Modeling Three - Phase Flow in Discretely Fractured Porous*

Rock (Doctor of Philosophy). University of Waterloo.

Zonge, K., Wynn, J., & Urquhart, S. (2005). Resistivity, induced polarization, and complex resistivity. In D. K. Butler (Ed.), *Near surface geophysics* (pp. 265–300). Tulsa, OK: Society of Exploration Geophysicists.

APPENDICES

Appendix A

Data CD

The material contained on this CD includes the Matlab scripts for generating the input models as well as raw input and output files from the gas flow, GPR, and ERT models and is available from the Department of Earth and Environmental Sciences, upon request.

Appendix B

Additional Electrical Resistivity Plots

B.1 Homogeneous Aquifer

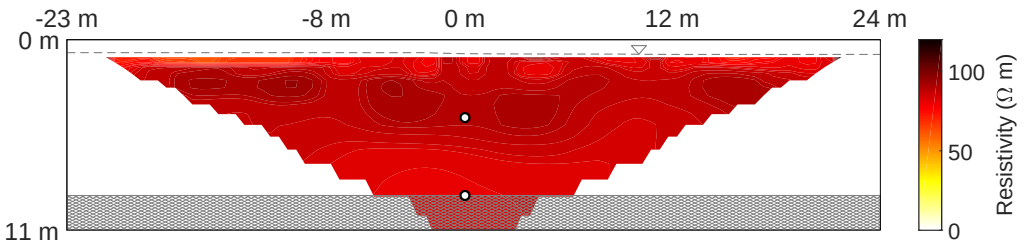

B.1: Background ERT response of a homogeneous aquifer

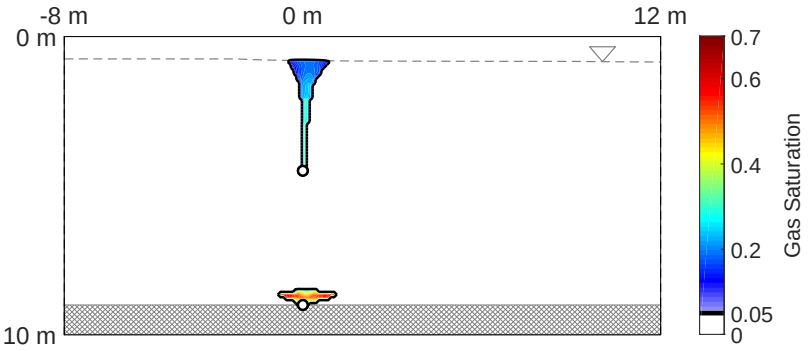

(a) Gas Saturation

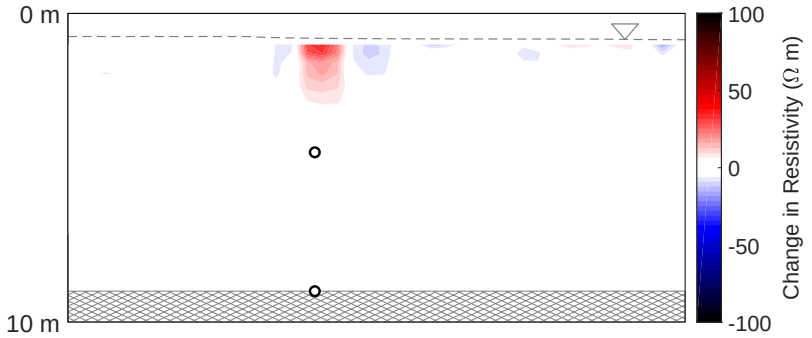

(b) ERT Response

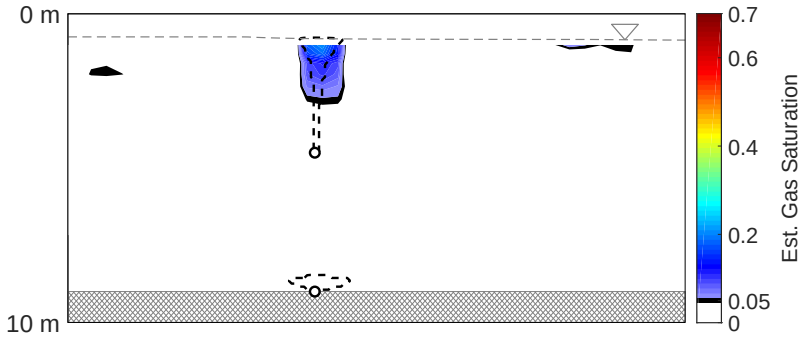

(c) Estimated change in the gas saturation from the inverted ERT data

B.2: Results from saturation model, ERT model, and the estimated saturation from ERT at Day 1 for a homogeneous aquifer.

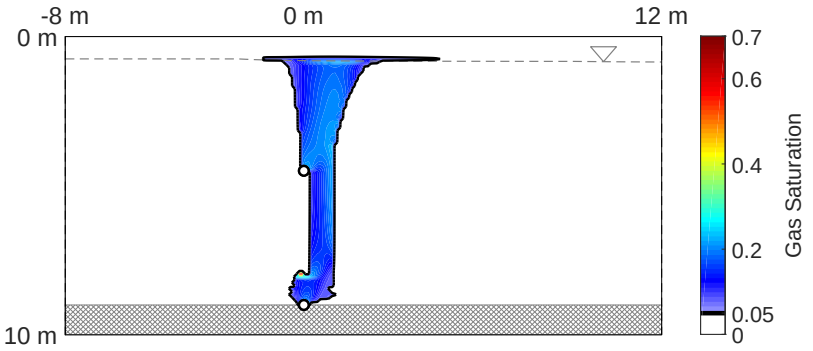

(a) Gas Saturation

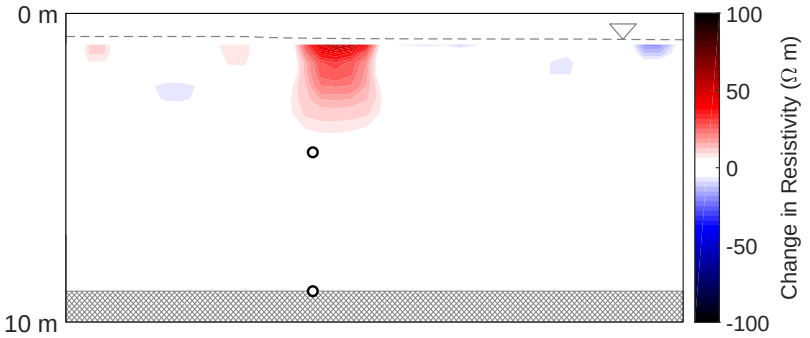

(b) ERT Response

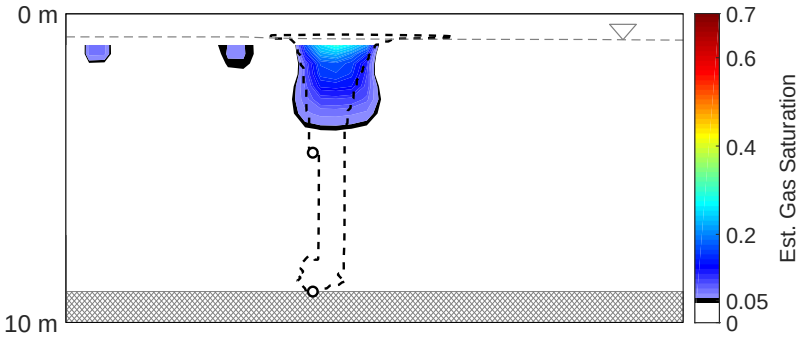

(c) Estimated change in the gas saturation from the inverted ERT data

B.3: Results from saturation model, ERT model, and the estimated saturation from ERT at Day 20 for a homogeneous aquifer.

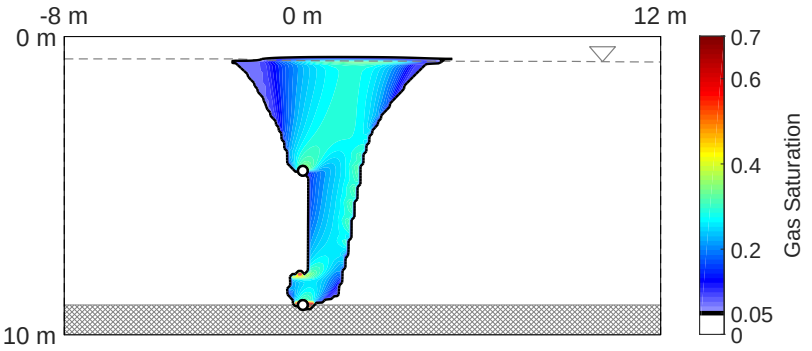

(a) Gas Saturation

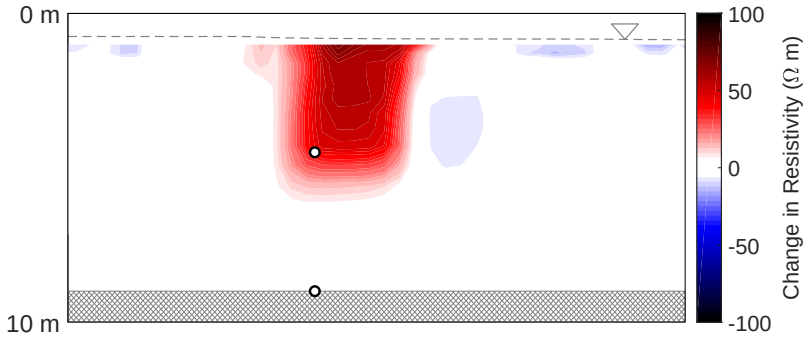

(b) ERT Response

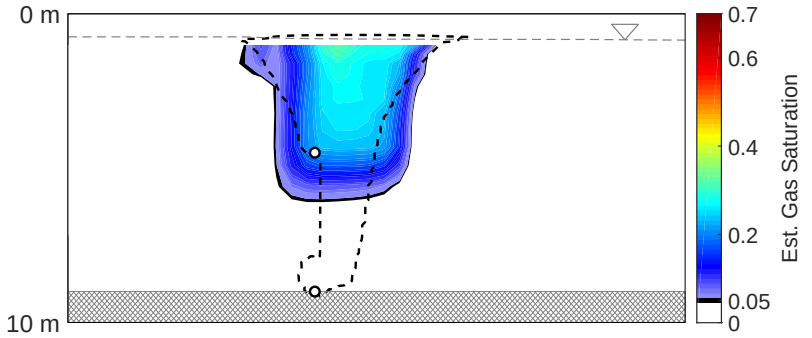

(c) Estimated change in the gas saturation from the inverted ERT data

B.4: Results from saturation model, ERT model, and the estimated saturation from ERT at Day 37 for a homogeneous aquifer.

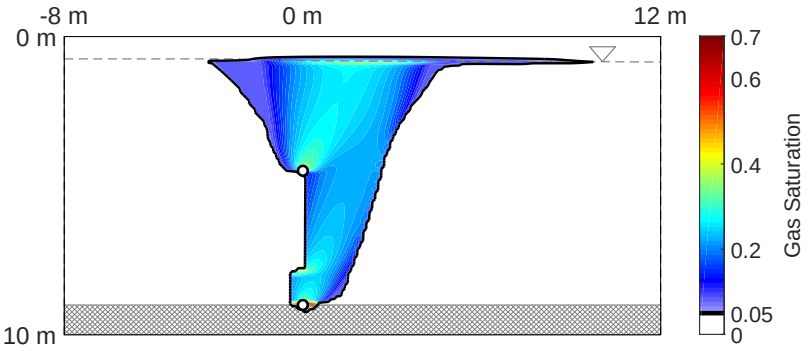

(a) Gas Saturation

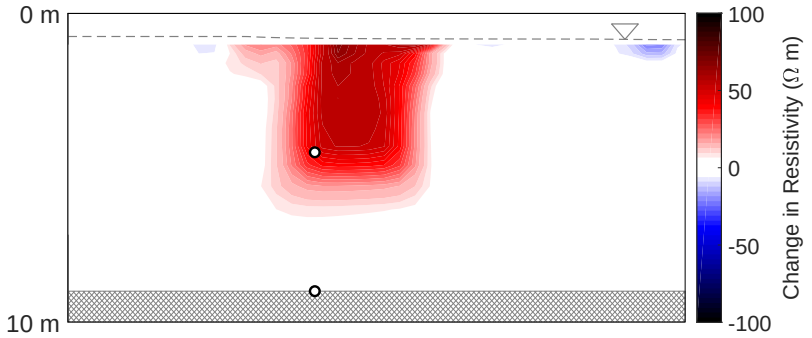

(b) ERT Response

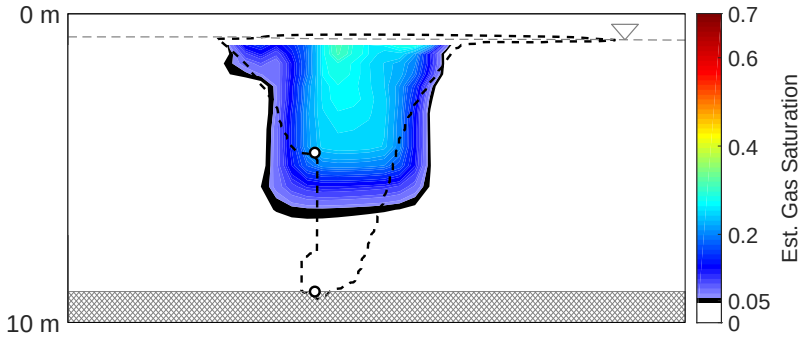

(c) Estimated change in the gas saturation from the inverted ERT data

B.5: Results from saturation model, ERT model, and the estimated saturation from ERT at Day 56 for a homogeneous aquifer.

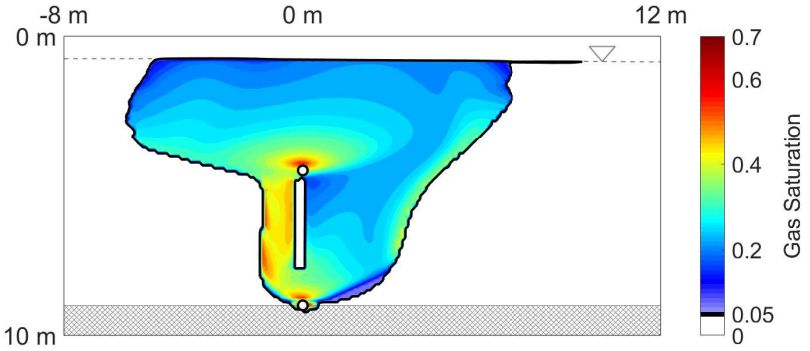

(a) Gas Saturation

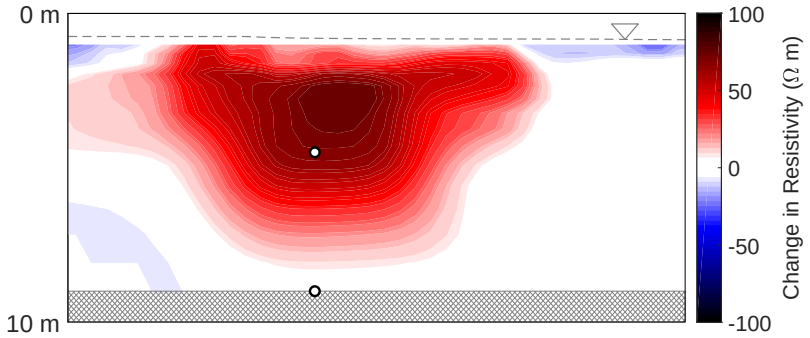

(b) ERT Response

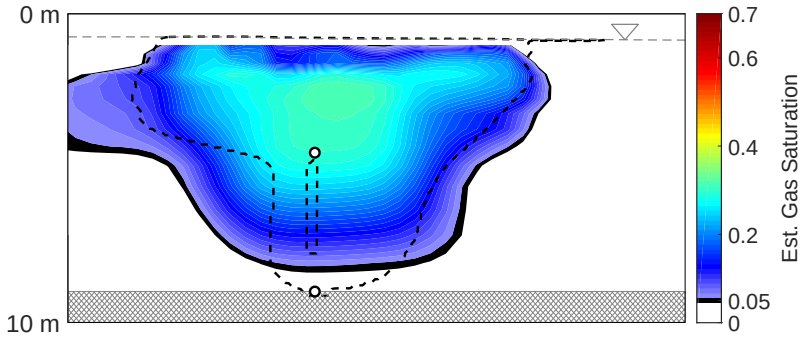

(c) Estimated change in the gas saturation from the inverted ERT data

B.6: Results from saturation model, ERT model, and the estimated saturation from ERT at Day 71 for a homogeneous aquifer.

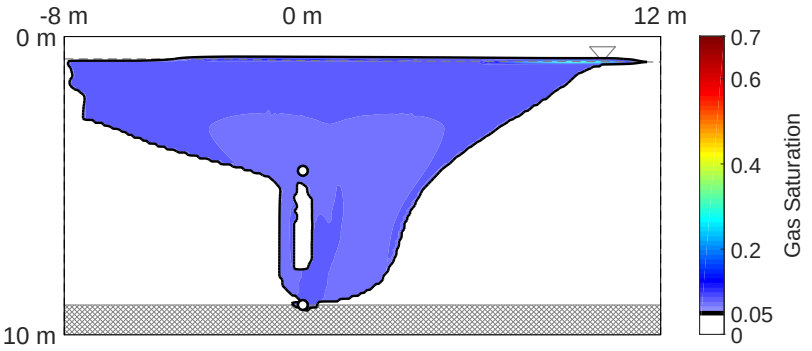

(a) Gas Saturation

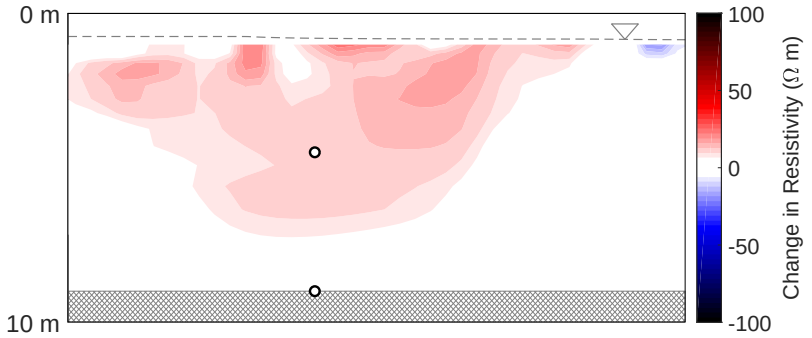

(b) ERT Response

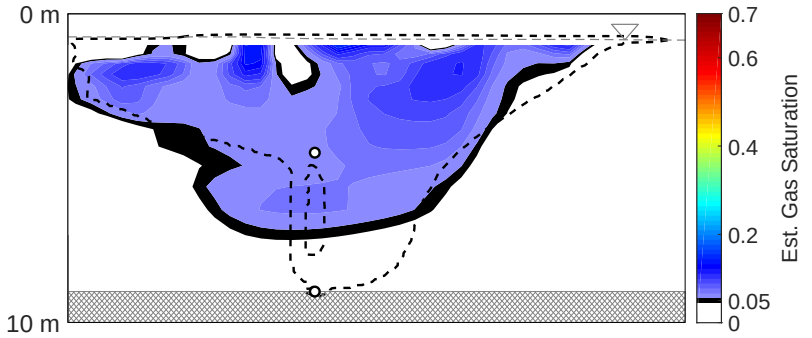

(c) Estimated change in the gas saturation from the inverted ERT data

B.7: Results from saturation model, ERT model, and the estimated saturation from ERT at Day 102 for a homogeneous aquifer.

B.2 Layer without Entry Pressure Change

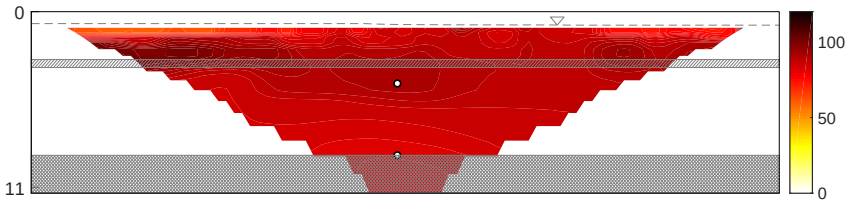

B.8: Background ERT response of a continuous layer ($k = 5.1 \times 10^{-13}$, $\phi = 0.31$), no entry pressure change

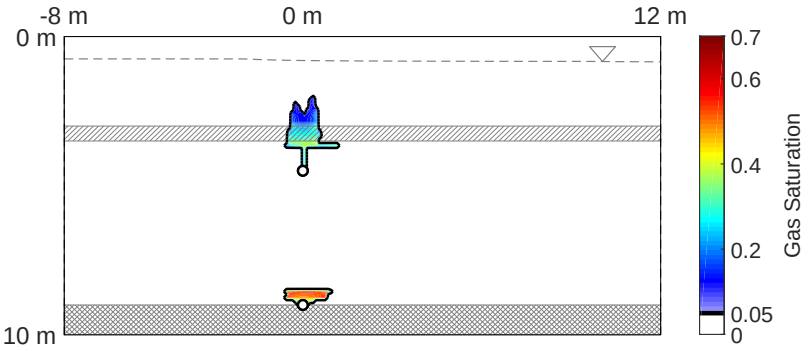

(a) Gas Saturation

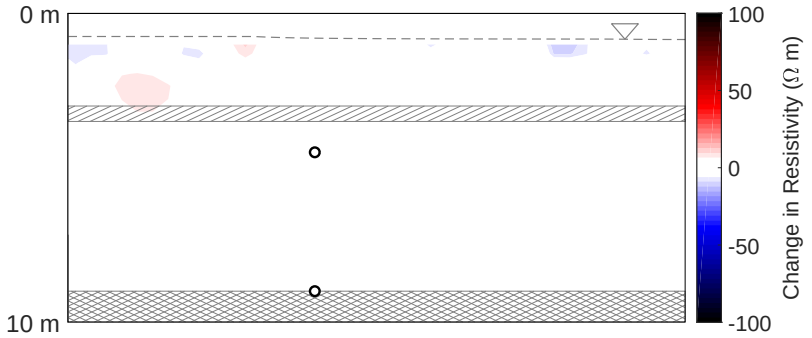

(b) ERT Response

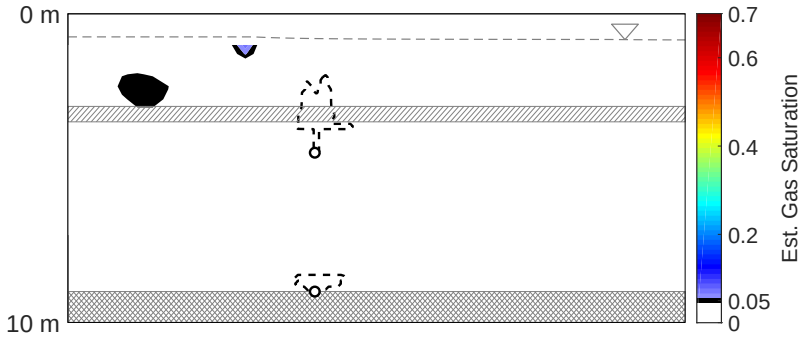

(c) Estimated change in the gas saturation from the inverted ERT data

B.9: Results from saturation model, ERT model, and the estimated saturation from ERT at Day 1 for a continuous layer ($k = 5.1 \times 10^{-13}$, $\phi = 0.31$), no entry pressure change.

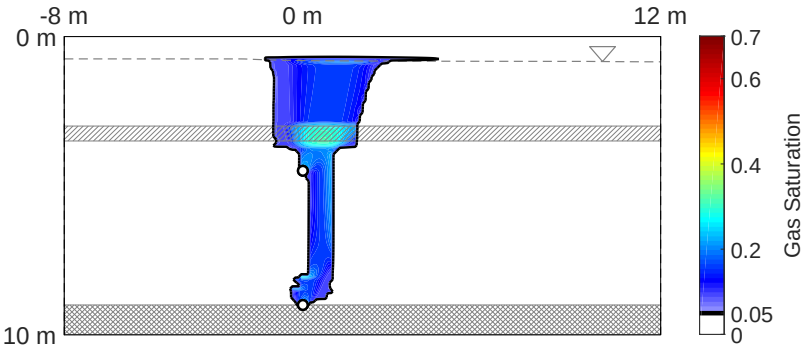

(a) Gas Saturation

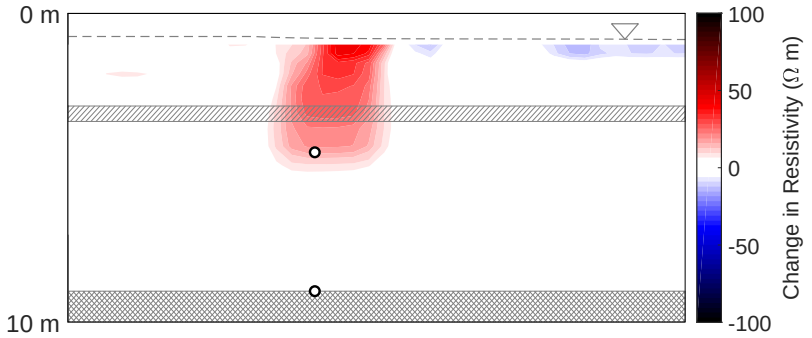

(b) ERT Response

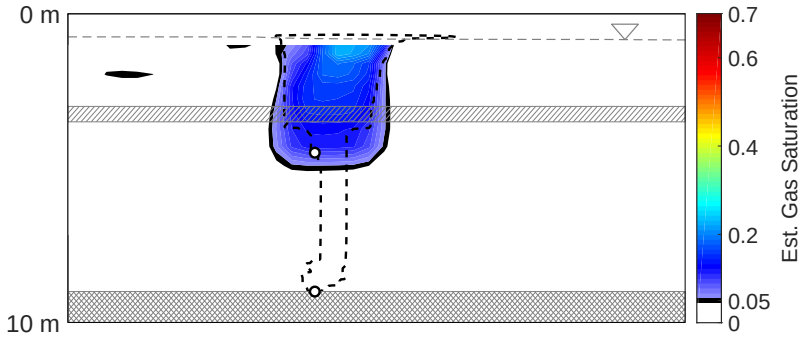

(c) Estimated change in the gas saturation from the inverted ERT data

B.10: Results from saturation model, ERT model, and the estimated saturation from ERT at Day 20 for a continuous layer ($k = 5.1 \times 10^{-13}$, $\phi = 0.31$), no entry pressure change.

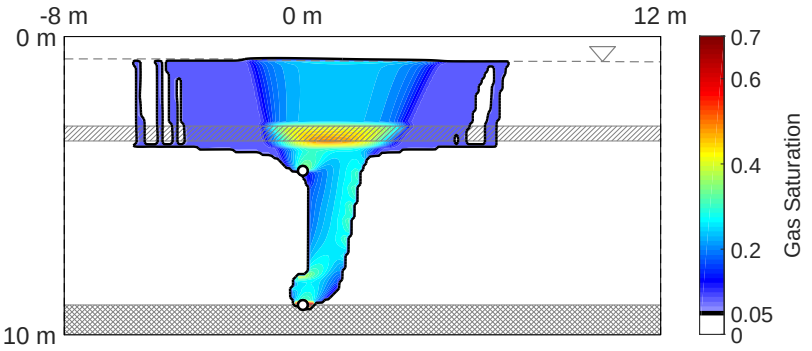

(a) Gas Saturation

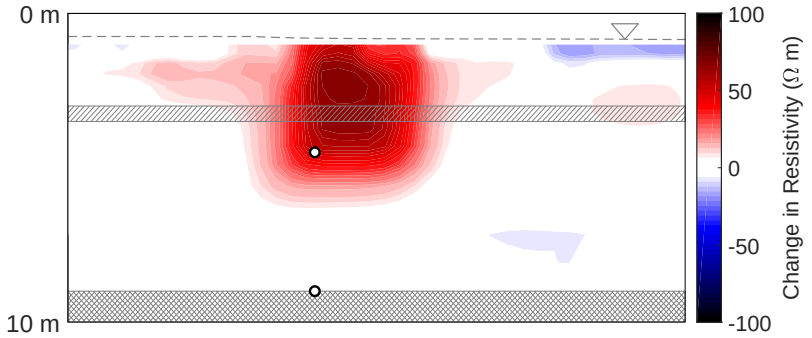

(b) ERT Response

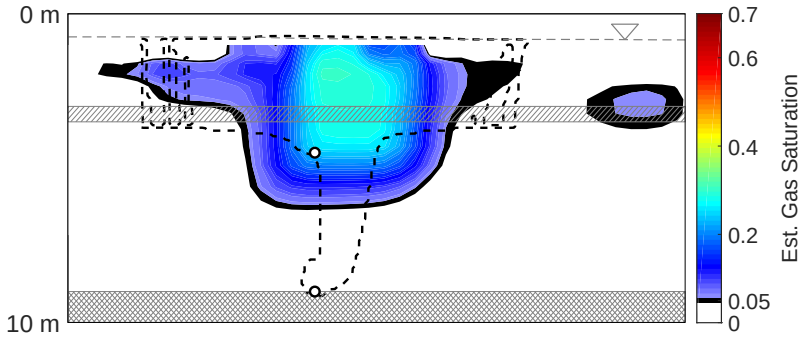

(c) Estimated change in the gas saturation from the inverted ERT data

B.11: Results from saturation model, ERT model, and the estimated saturation from ERT at Day 37 for a continuous layer ($k = 5.1 \times 10^{-13}$, $\phi = 0.31$), no entry pressure change.

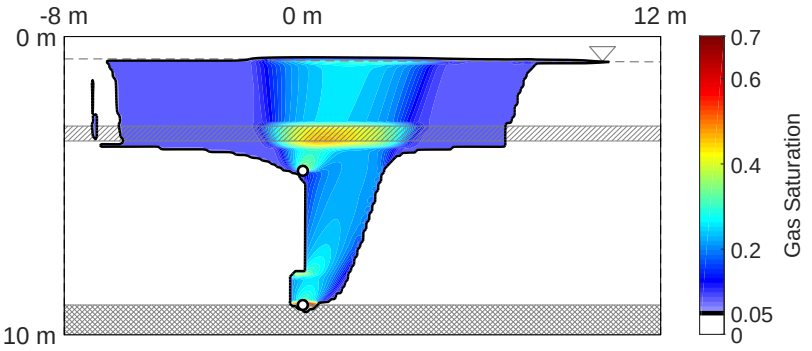

(a) Gas Saturation

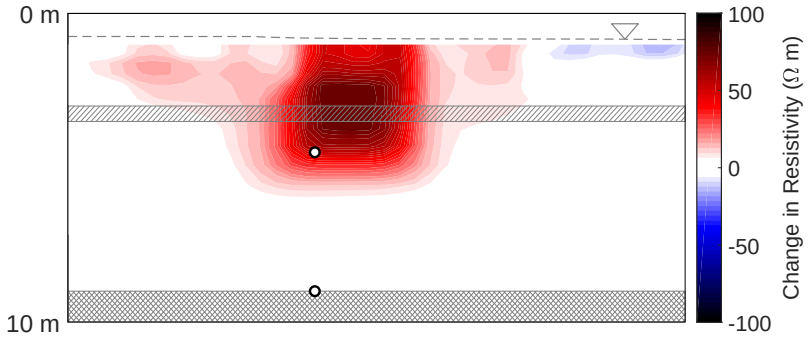

(b) ERT Response

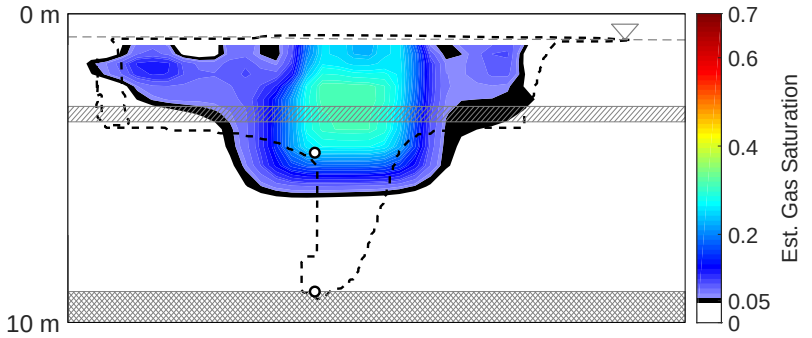

(c) Estimated change in the gas saturation from the inverted ERT data

B.12: Results from saturation model, ERT model, and the estimated saturation from ERT at Day 56 for a continuous layer ($k = 5.1 \times 10^{-13}$, $\phi = 0.31$), no entry pressure change.

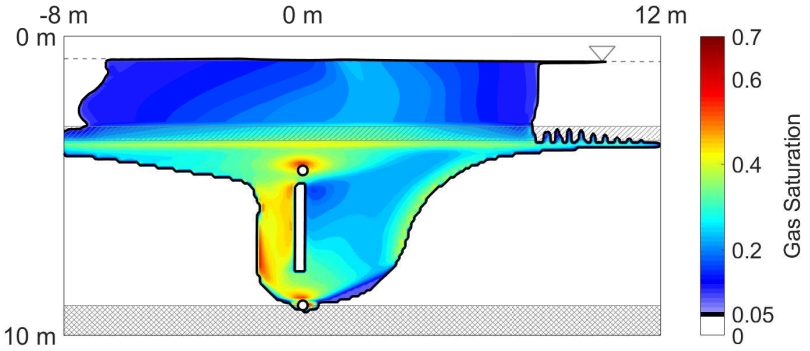

(a) Gas Saturation

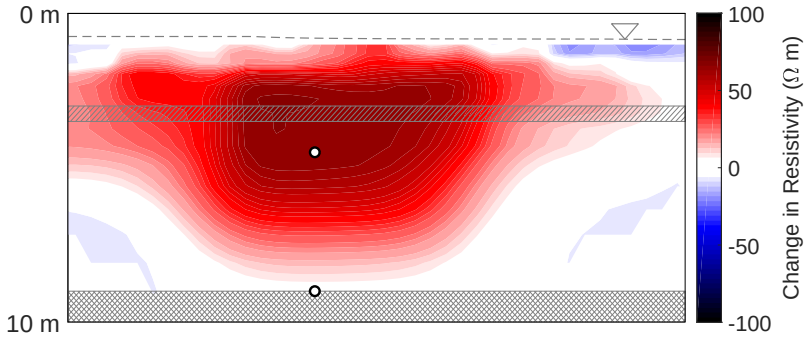

(b) ERT Response

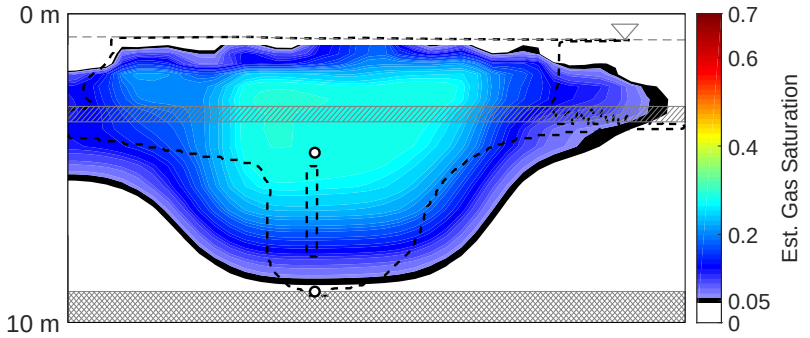

(c) Estimated change in the gas saturation from the inverted ERT data

B.13: Results from saturation model, ERT model, and the estimated saturation from ERT at Day 71 for a continuous layer ($k = 5.1 \times 10^{-13}$, $\phi = 0.31$), no entry pressure change.

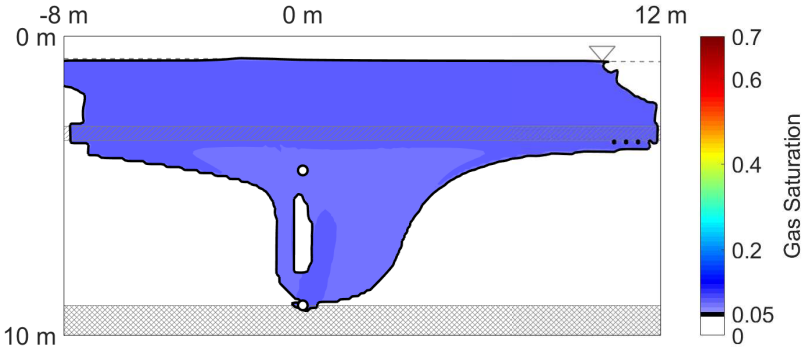

(a) Gas Saturation

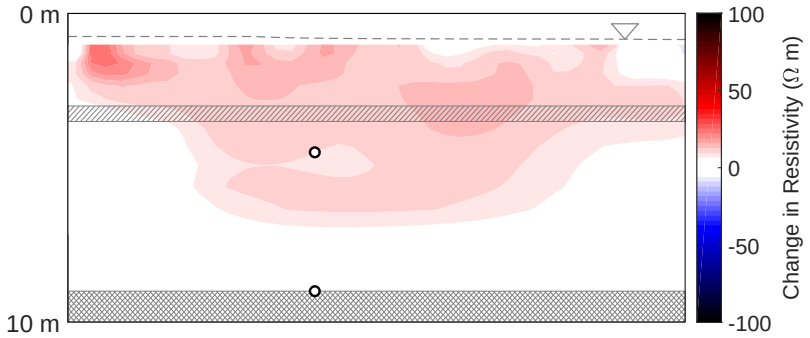

(b) ERT Response

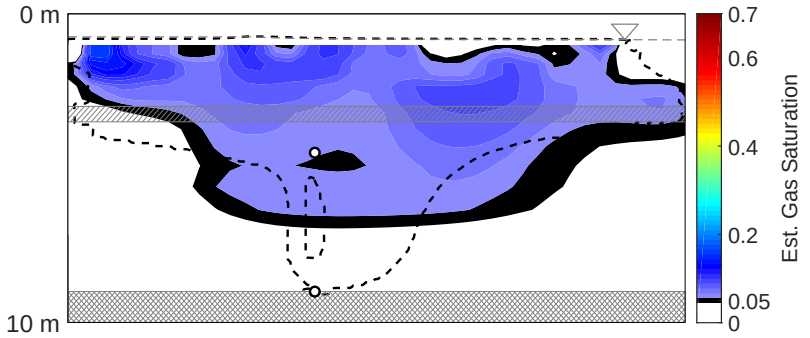

(c) Estimated change in the gas saturation from the inverted ERT data

B.14: Results from saturation model, ERT model, and the estimated saturation from ERT at Day 102 for a continuous layer ($k = 5.1 \times 10^{-13}$, $\phi = 0.31$), no entry pressure change.

B.3 Layer with Entry pressure

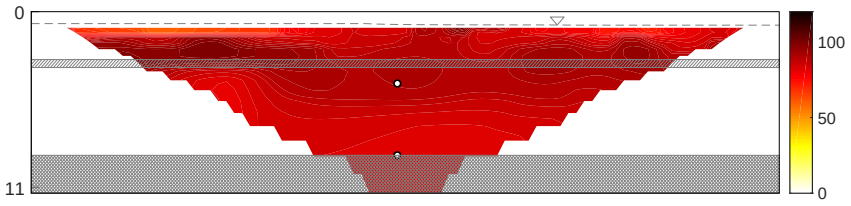

B.15: Background ERT response of a continuous layer ($k = 5.1 \times 10^{-13}$, $\phi = 0.31$) with a higher entry pressure ($P_c = 2.99$ kPa)

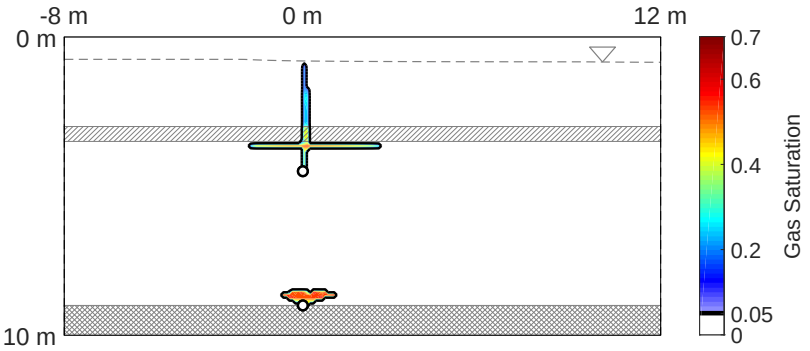

(a) Gas Saturation

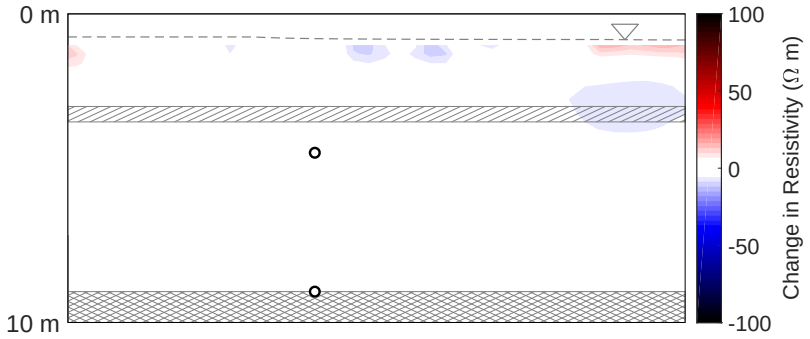

(b) ERT Response

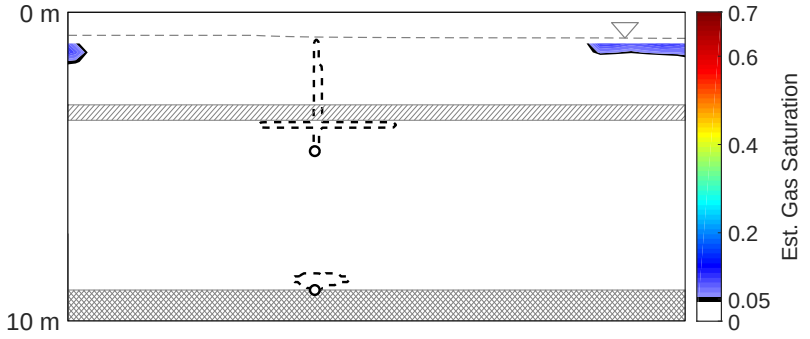

(c) Estimated change in the gas saturation from the inverted ERT data

B.16: Results from saturation model, ERT model, and the estimated saturation from ERT at Day 1 for a continuous layer ($k = 5.1 \times 10^{-13}$, $\phi = 0.31$) with a higher entry pressure ($P_c = 2.99$ kPa).

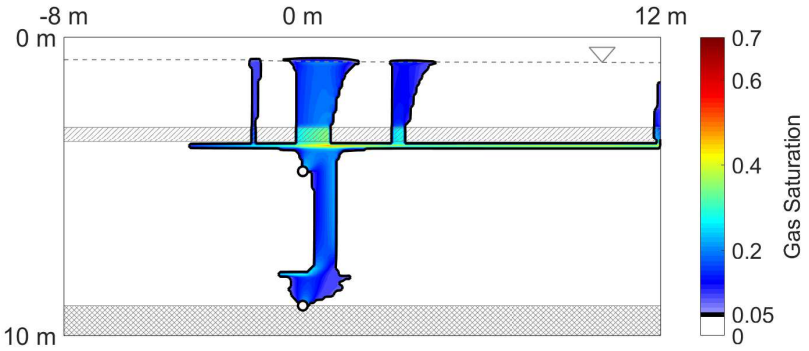

(a) Gas Saturation

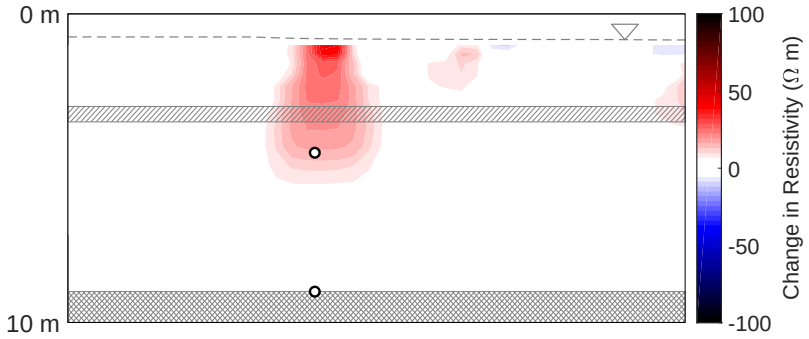

(b) ERT Response

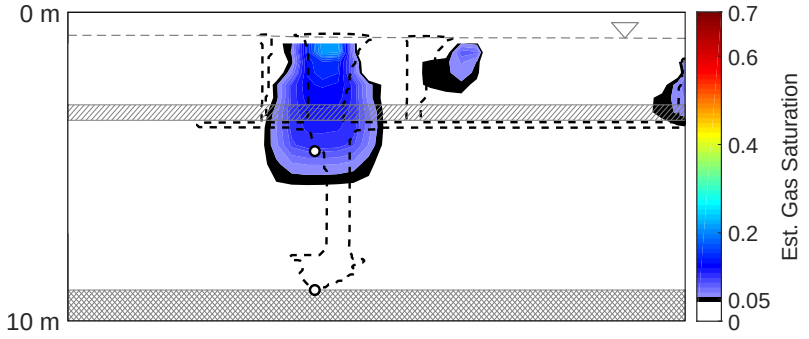

(c) Estimated change in the gas saturation from the inverted ERT data

B.17: Results from saturation model, ERT model, and the estimated saturation from ERT at Day 20 for a continuous layer ($k = 5.1 \times 10^{-13}$, $\phi = 0.31$) with a higher entry pressure ($P_c = 2.99$ kPa).

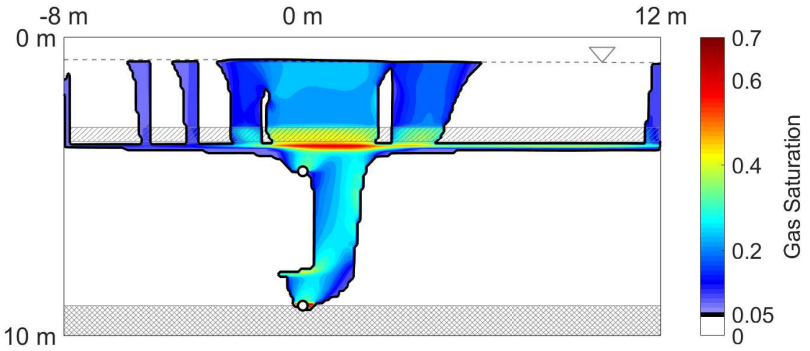

(a) Gas Saturation

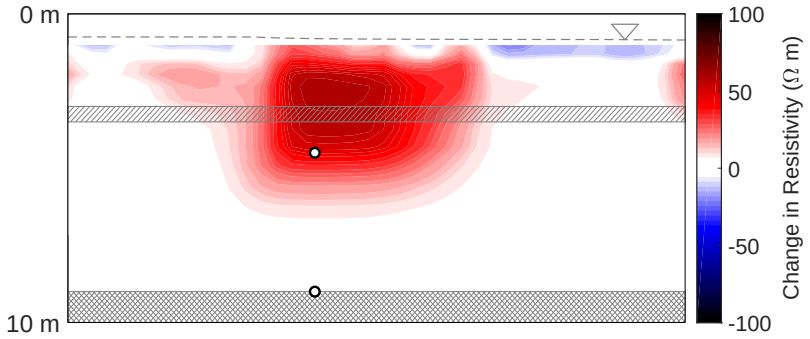

(b) ERT Response

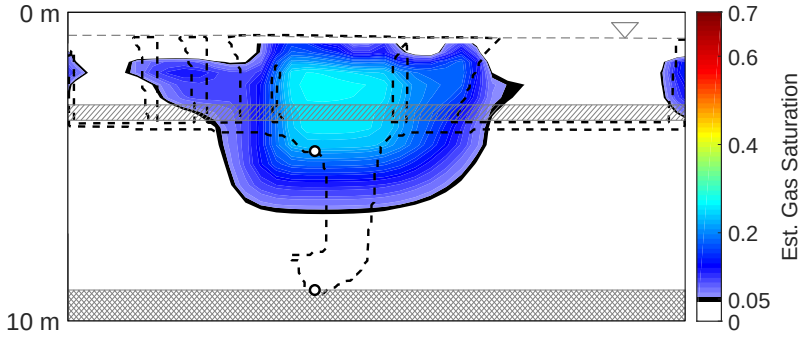

(c) Estimated change in the gas saturation from the inverted ERT data

B.18: Results from saturation model, ERT model, and the estimated saturation from ERT at Day 37 for a continuous layer ($k = 5.1 \times 10^{-13}$, $\phi = 0.31$) with a higher entry pressure ($P_c = 2.99$ kPa).

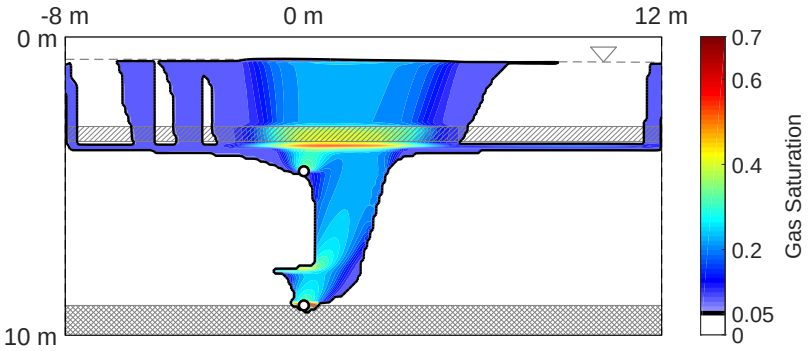

(a) Gas Saturation

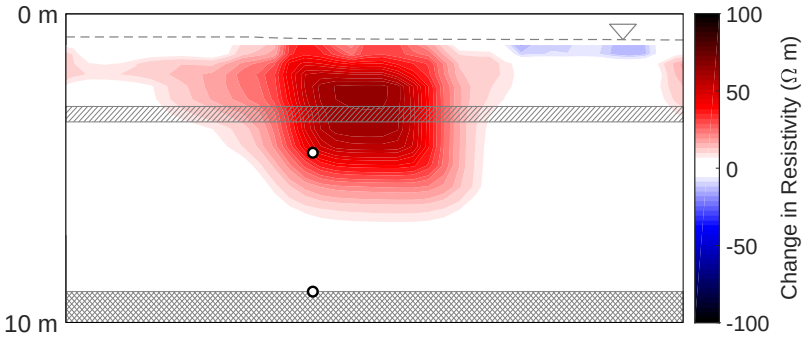

(b) ERT Response

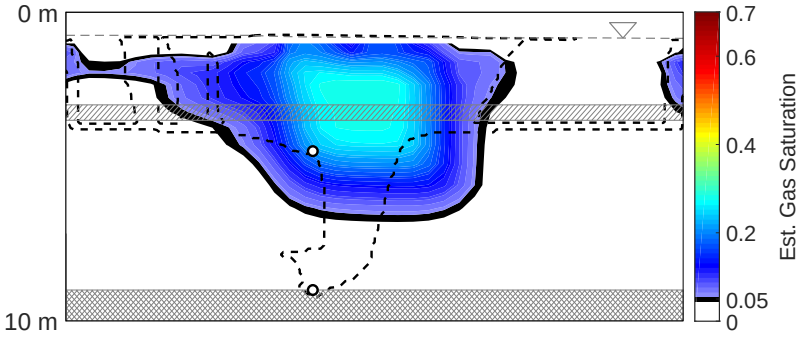

(c) Estimated change in the gas saturation from the inverted ERT data

B.19: Results from saturation model, ERT model, and the estimated saturation from ERT at Day 56 for a continuous layer ($k = 5.1 \times 10^{-13}$, $\phi = 0.31$) with a higher entry pressure ($P_c = 2.99$ kPa).

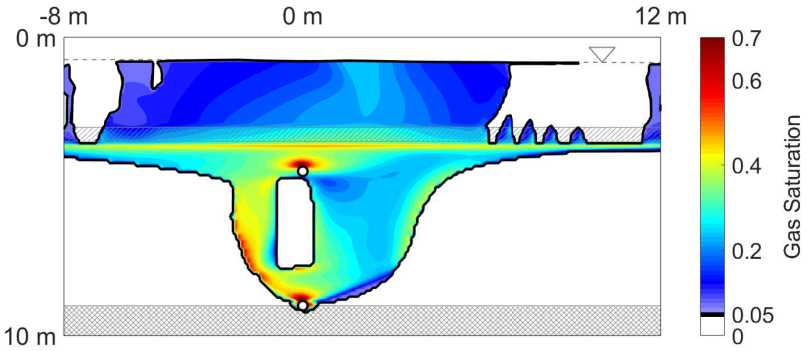

(a) Gas Saturation

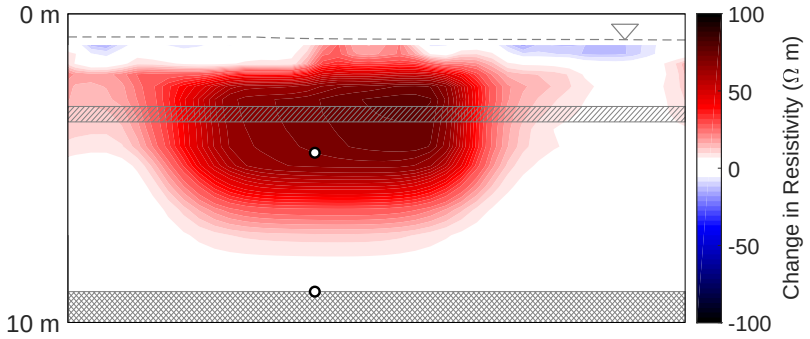

(b) ERT Response

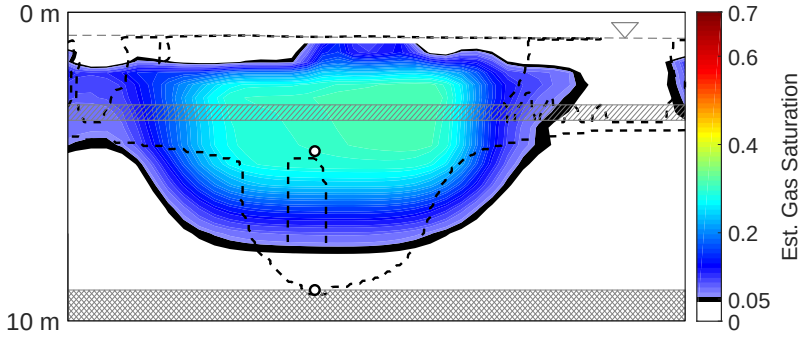

(c) Estimated change in the gas saturation from the inverted ERT data

B.20: Results from saturation model, ERT model, and the estimated saturation from ERT at Day 71 for a continuous layer ($k = 5.1 \times 10^{-13}$, $\phi = 0.31$) with a higher entry pressure ($P_c = 2.99$ kPa).

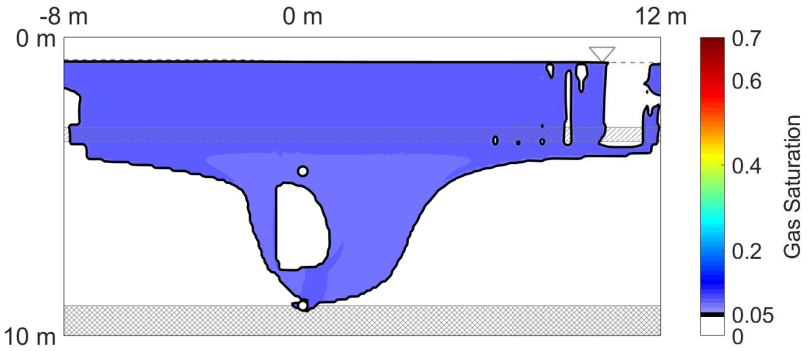

(a) Gas Saturation

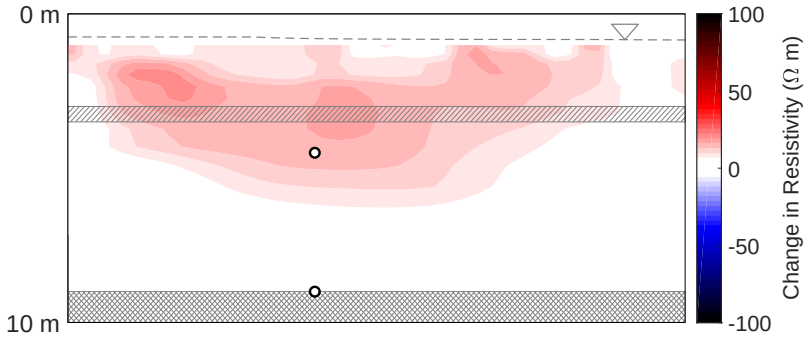

(b) ERT Response

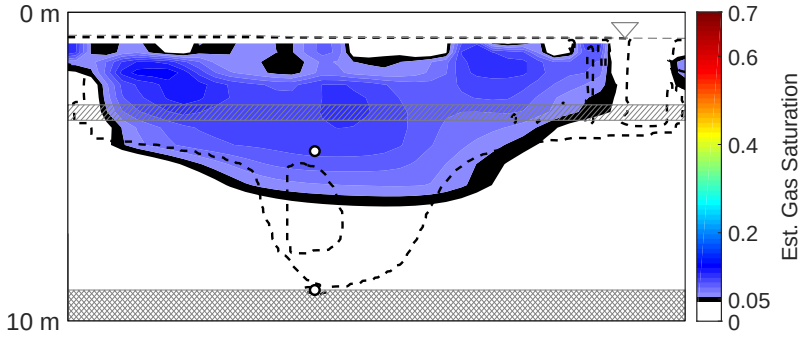

(c) Estimated change in the gas saturation from the inverted ERT data

B.21: Results from saturation model, ERT model, and the estimated saturation from ERT at Day 102 for a continuous layer ($k = 5.1 \times 10^{-13}$, $\phi = 0.31$) with a higher entry pressure ($P_c = 2.99$ kPa).

B.4 Discontinuous Layer

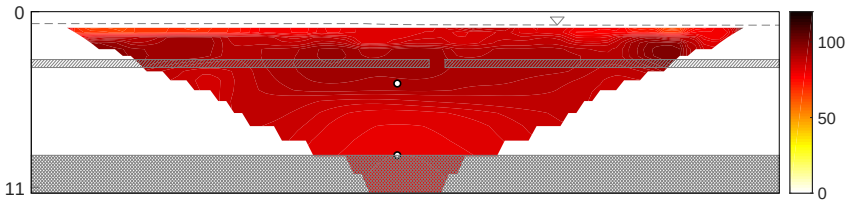

B.22: Background ERT response of a discontinuous layer ($k = 5.1 \times 10^{-13}$, $\phi = 0.31$) with a higher entry pressure ($P_c = 2.99$ kPa), discontinuous from 2 m to 3 m

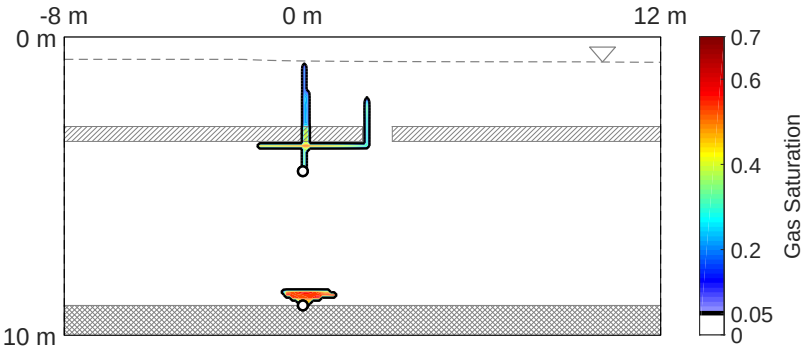

(a) Gas Saturation

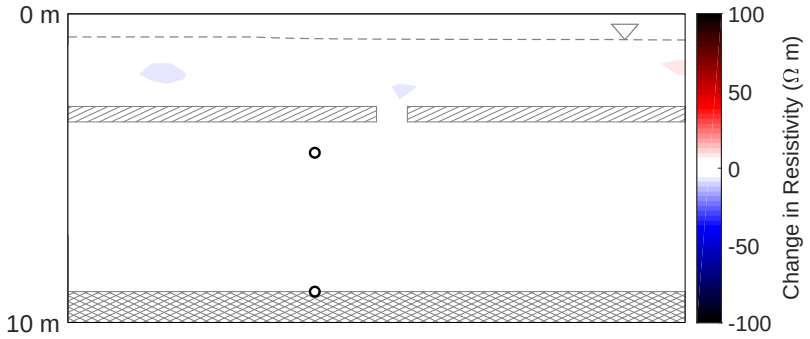

(b) ERT Response

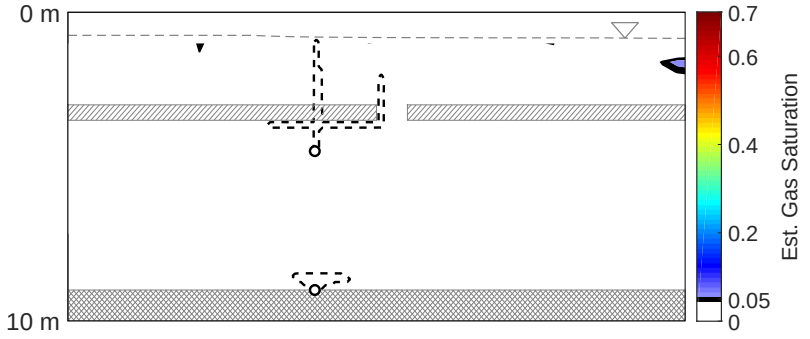

(c) Estimated change in the gas saturation from the inverted ERT data

B.23: Results from saturation model, ERT model, and the estimated saturation from ERT at Day 1 for a discontinuous layer ($k = 5.1 \times 10^{-13}$, $\phi = 0.31$) with a higher entry pressure ($P_c = 2.99$ kPa), discontinuous from 2 m to 3 m.

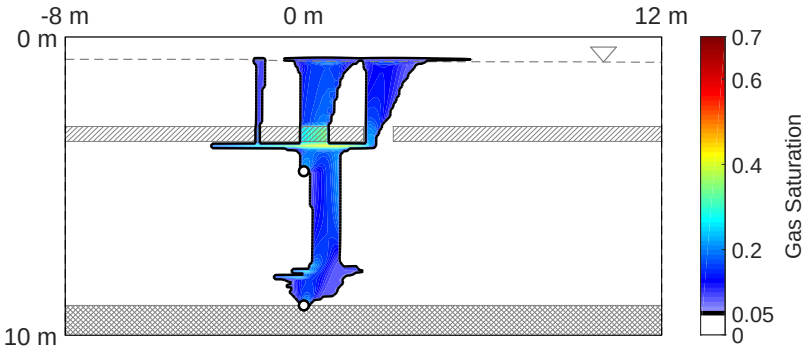

(a) Gas Saturation

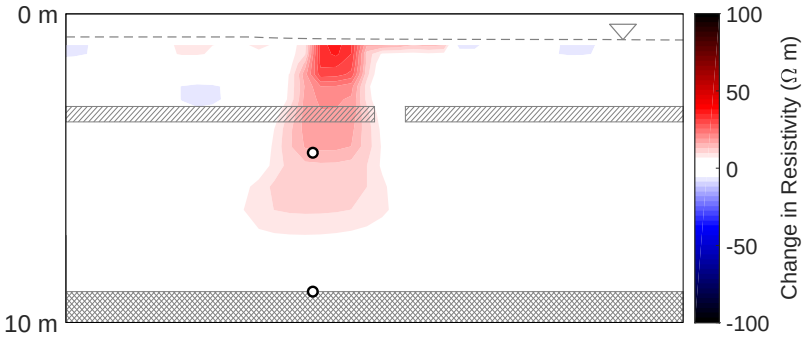

(b) ERT Response

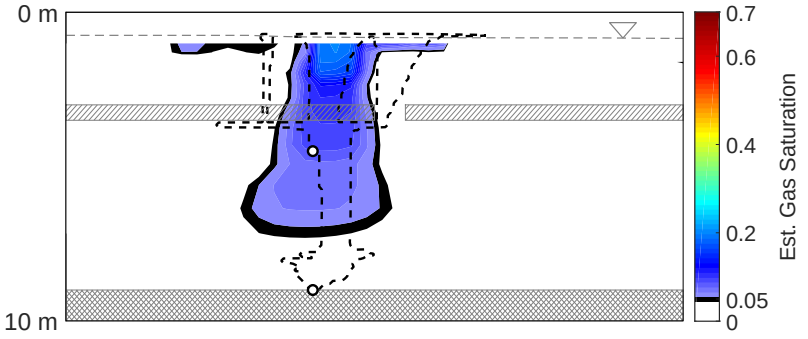

(c) Estimated change in the gas saturation from the inverted ERT data

B.24: Results from saturation model, ERT model, and the estimated saturation from ERT at Day 20 for a discontinuous layer ($k = 5.1 \times 10^{-13}$, $\phi = 0.31$) with a higher entry pressure ($P_c = 2.99$ kPa), discontinuous from 2 m to 3 m.

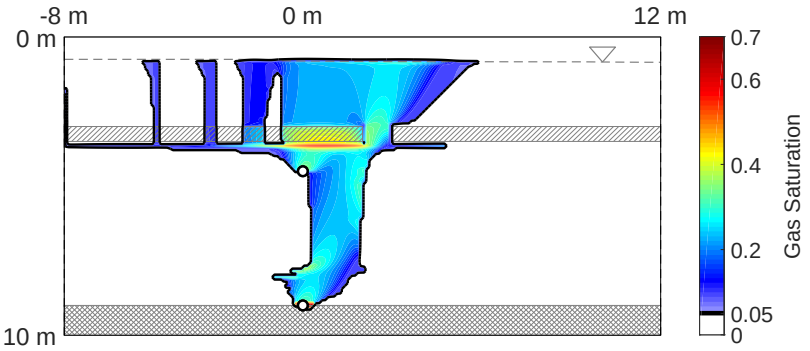

(a) Gas Saturation

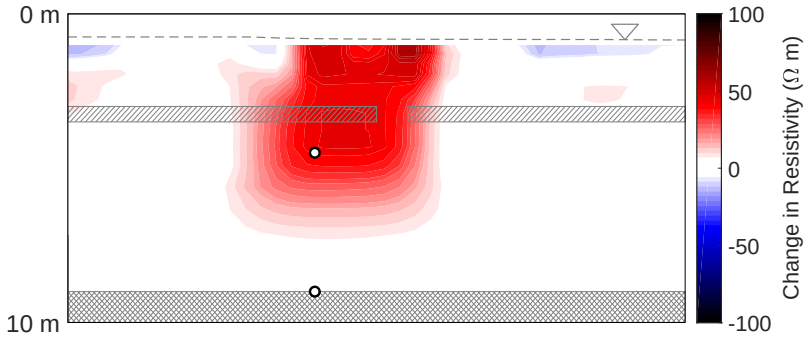

(b) ERT Response

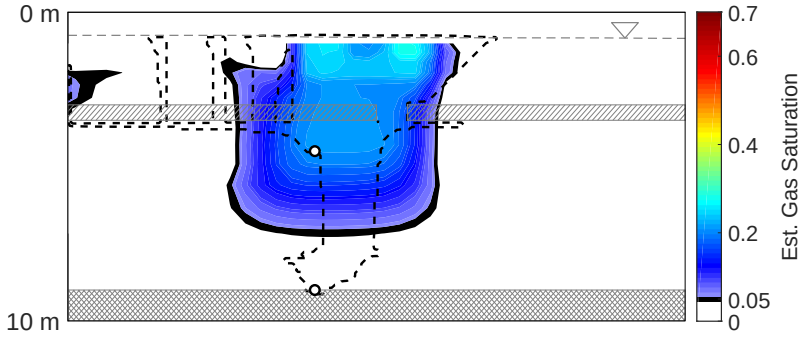

(c) Estimated change in the gas saturation from the inverted ERT data

B.25: Results from saturation model, ERT model, and the estimated saturation from ERT at Day 37 for a discontinuous layer ($k = 5.1 \times 10^{-13}$, $\phi = 0.31$) with a higher entry pressure ($P_c = 2.99$ kPa), discontinuous from 2 m to 3 m.

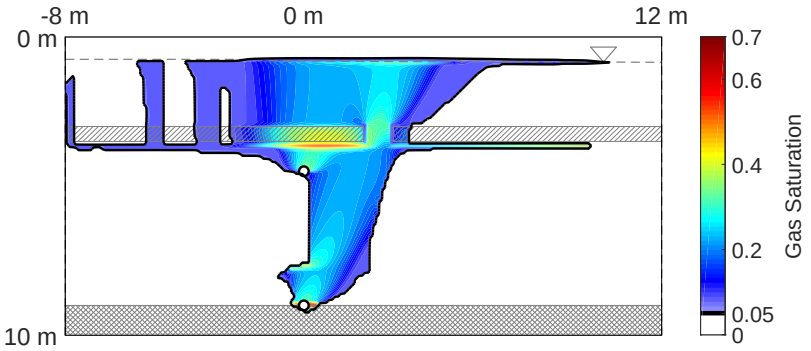

(a) Gas Saturation

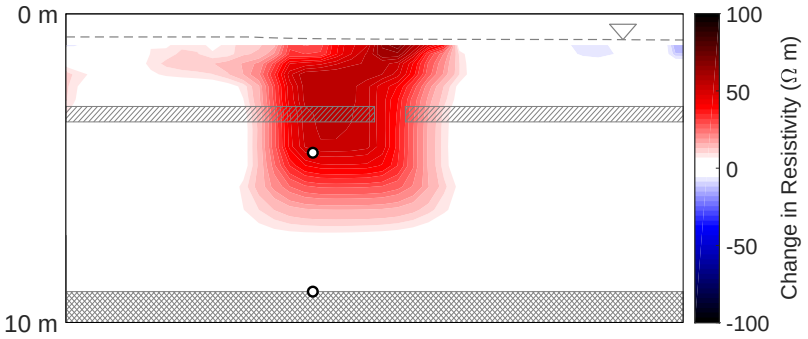

(b) ERT Response

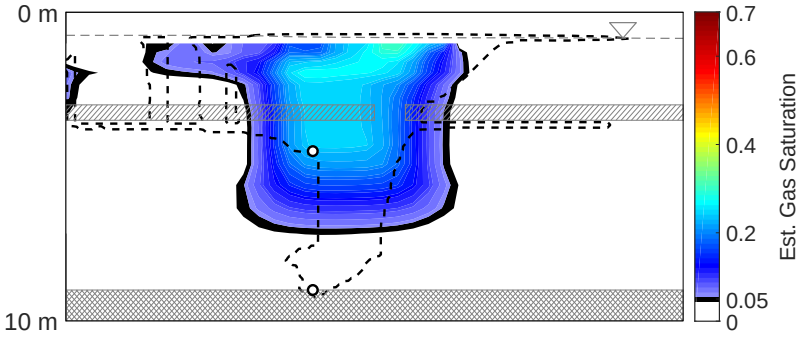

(c) Estimated change in the gas saturation from the inverted ERT data

B.26: Results from saturation model, ERT model, and the estimated saturation from ERT at Day 56 for a discontinuous layer ($k = 5.1 \times 10^{-13}$, $\phi = 0.31$) with a higher entry pressure ($P_c = 2.99$ kPa), discontinuous from 2 m to 3 m.

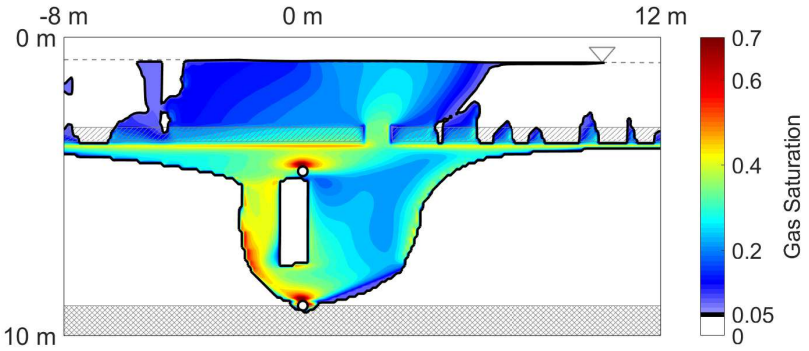

(a) Gas Saturation

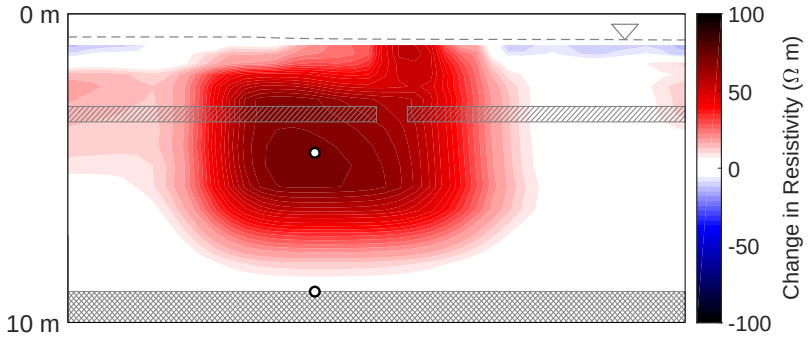

(b) ERT Response

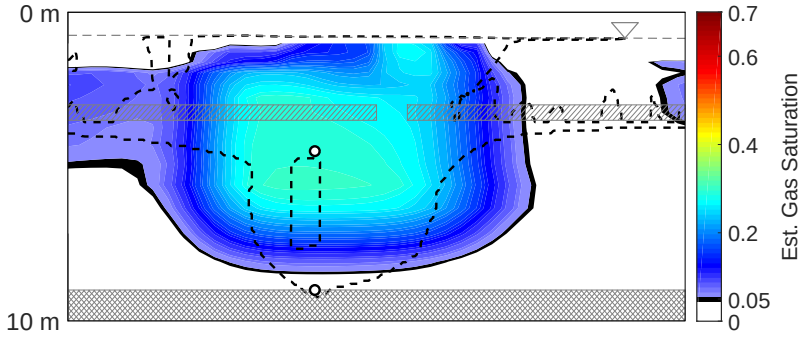

(c) Estimated change in the gas saturation from the inverted ERT data

B.27: Results from saturation model, ERT model, and the estimated saturation from ERT at Day 71 for a discontinuous layer ($k = 5.1 \times 10^{-13}$, $\phi = 0.31$) with a higher entry pressure ($P_c = 2.99$ kPa), discontinuous from 2 m to 3 m.

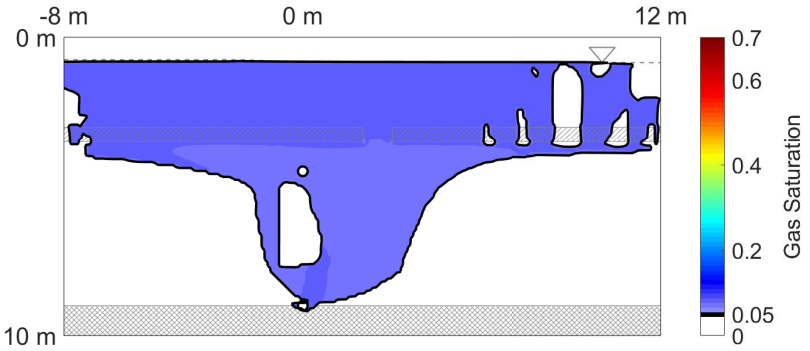

(a) Gas Saturation

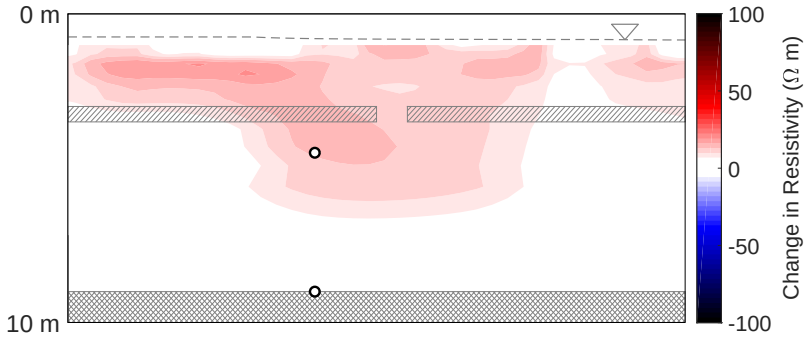

(b) ERT Response

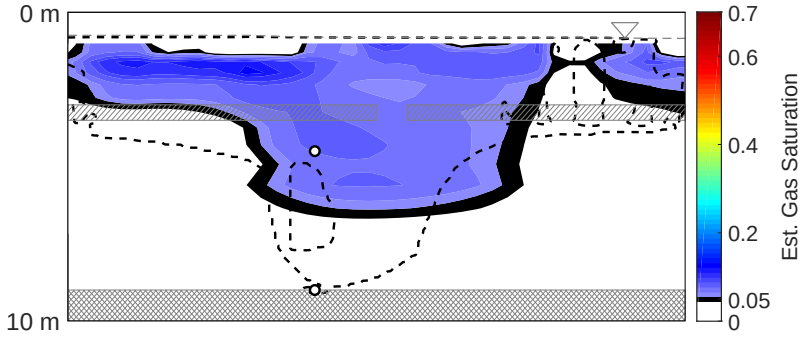

(c) Estimated change in the gas saturation from the inverted ERT data

B.28: Results from saturation model, ERT model, and the estimated saturation from ERT at Day 102 for a discontinuous layer ($k = 5.1 \times 10^{-13}$, $\phi = 0.31$) with a higher entry pressure ($P_c = 2.99$ kPa), discontinuous from 2 m to 3 m.

Appendix C

Additional Ground-Penetrating Radar Plots

C.1 Homogeneous Aquifer

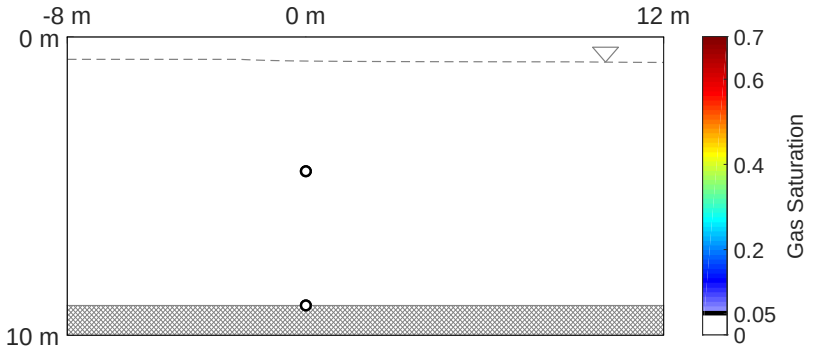

(a) Gas saturation

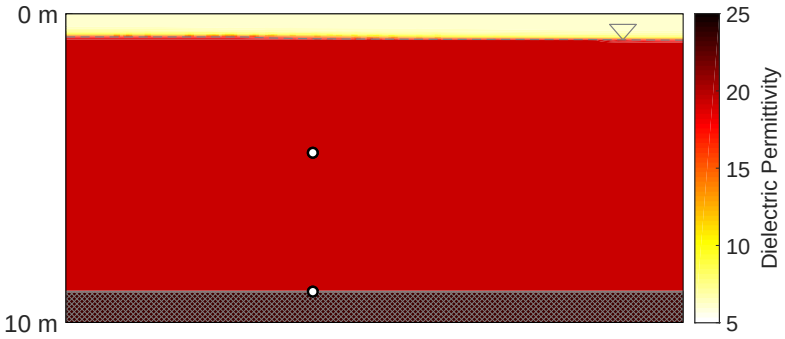

(b) Relative Permittivity

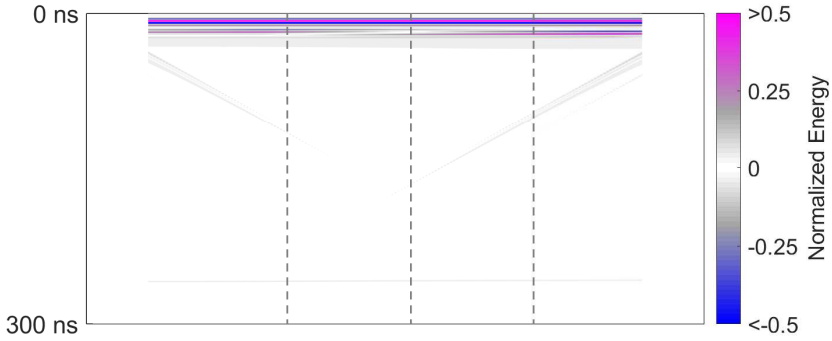

(c) Normalized GPR Amplitude

Figure C.1: Results from saturation model and GPR model, as well as the dielectric permittivity distribution at Day 0 for a homogeneous aquifer. The grey dashed lines show the locations used for the time-lapse plots.

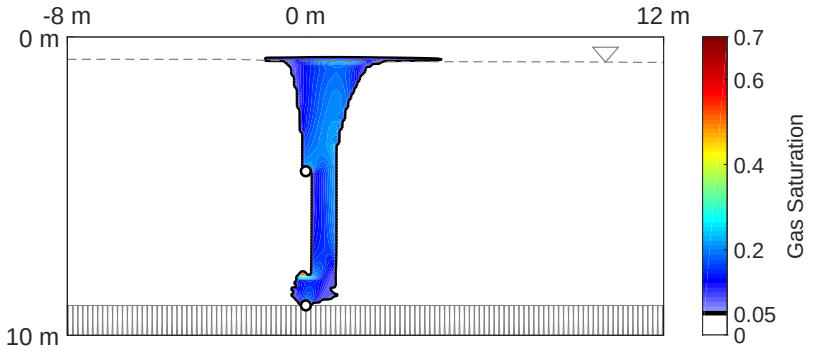

(a) Gas saturation

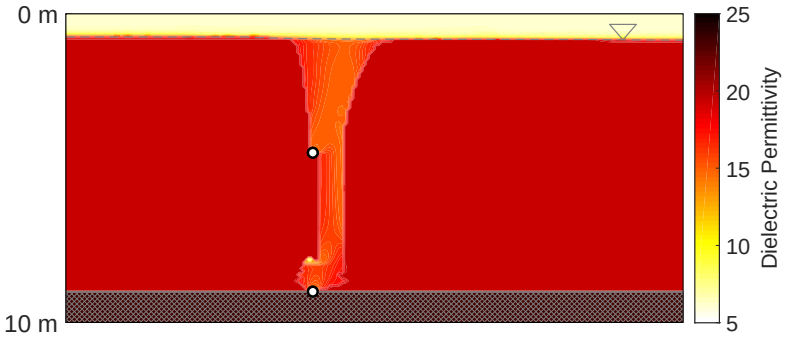

(b) Relative Permittivity

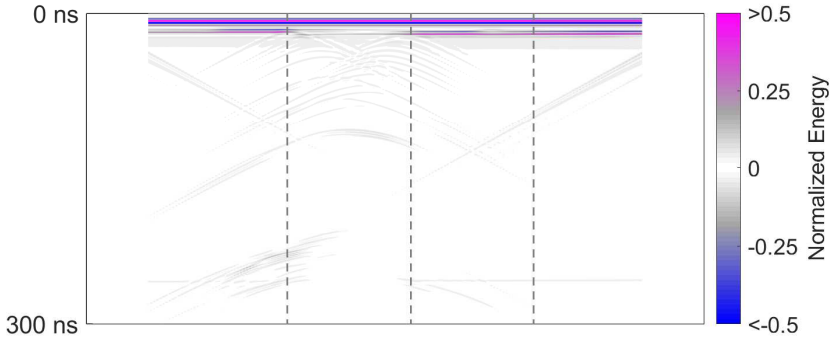

(c) Normalized GPR Amplitude

Figure C.2: Results from saturation model and GPR model, as well as the dielectric permittivity distribution at Day 20 for a homogeneous aquifer. The grey dashed lines show the locations used for the time-lapse plots.

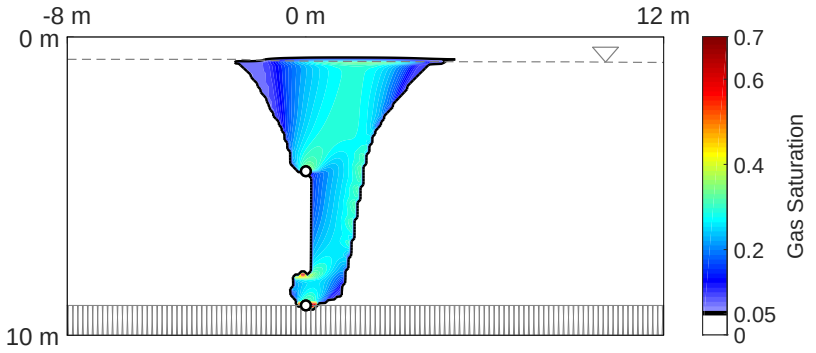

(a) Gas saturation

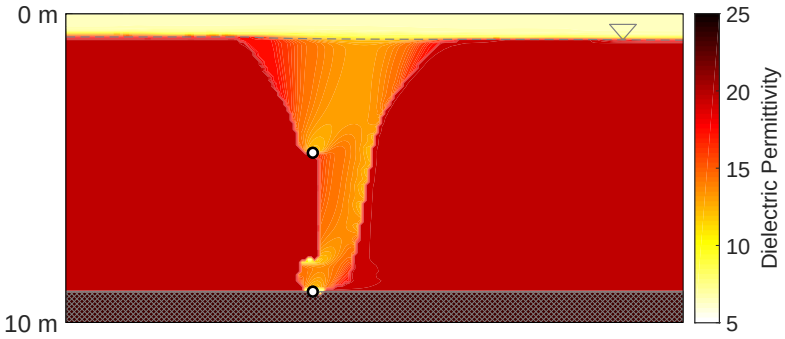

(b) Relative Permittivity

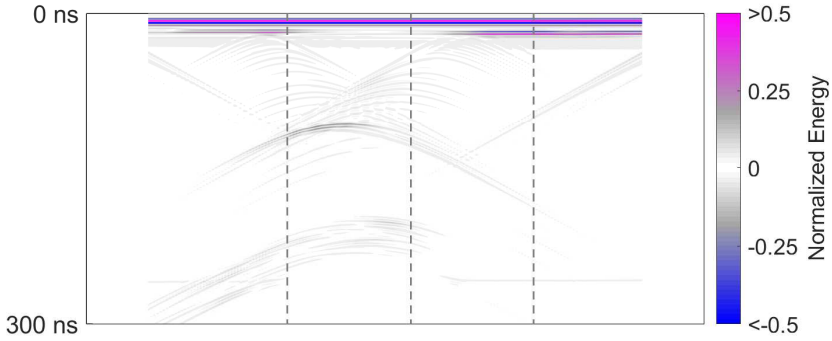

(c) Normalized GPR Amplitude

Figure C.3: Results from saturation model and GPR model, as well as the dielectric permittivity distribution at Day 37 for a homogeneous aquifer. The grey dashed lines show the locations used for the time-lapse plots.

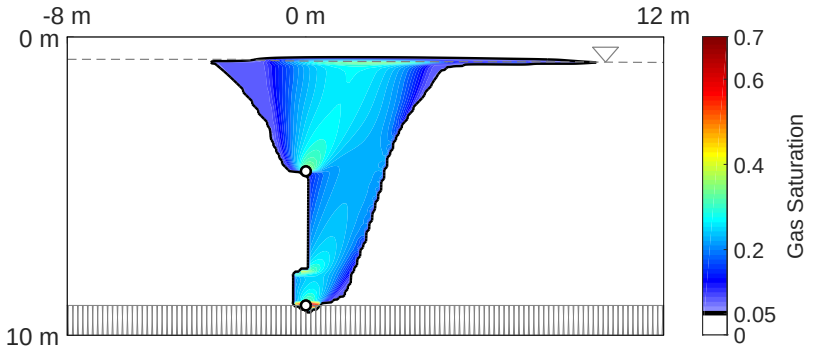

(a) Gas saturation

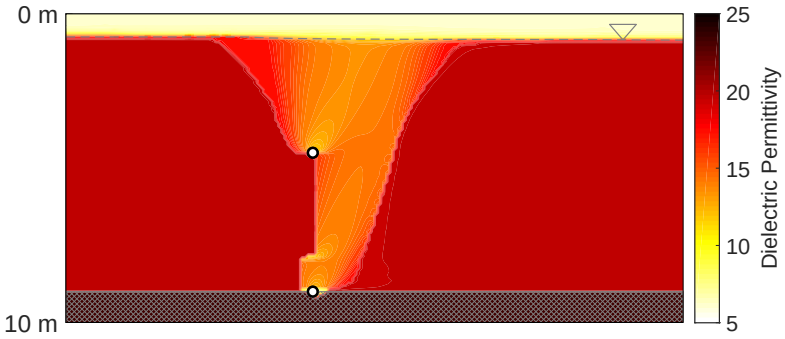

(b) Relative Permittivity

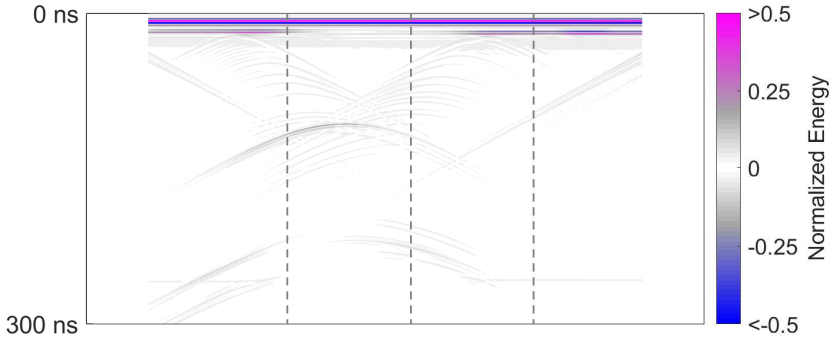

(c) Normalized GPR Amplitude

Figure C.4: Results from saturation model and GPR model, as well as the dielectric permittivity distribution at Day 56 for a homogeneous aquifer. The grey dashed lines show the locations used for the time-lapse plots.

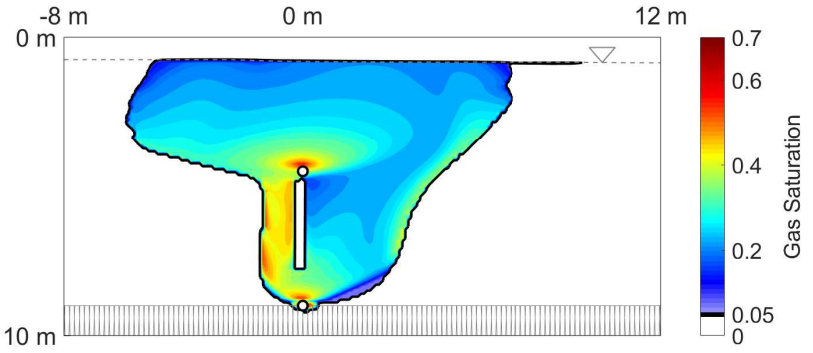

(a) Gas saturation

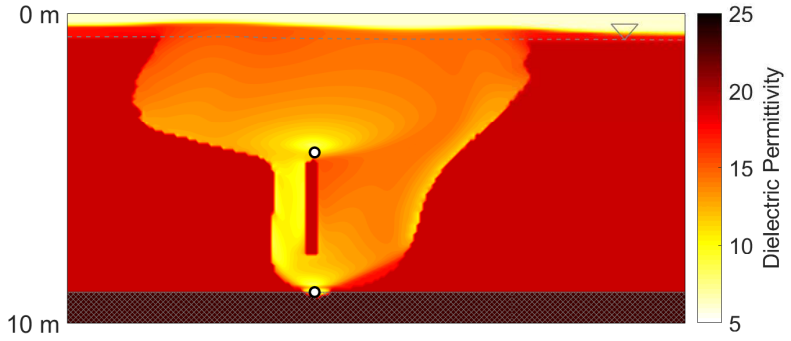

(b) Relative Permittivity

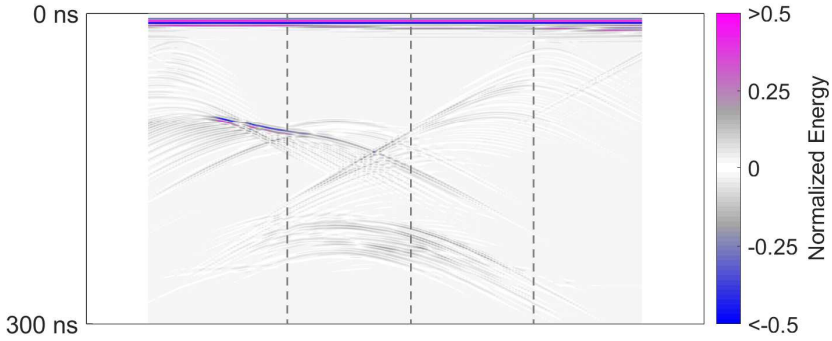

(c) Normalized GPR Amplitude

Figure C.5: Results from saturation model and GPR model, as well as the dielectric permittivity distribution at Day 71 for a homogeneous aquifer. The grey dashed lines show the locations used for the time-lapse plots.

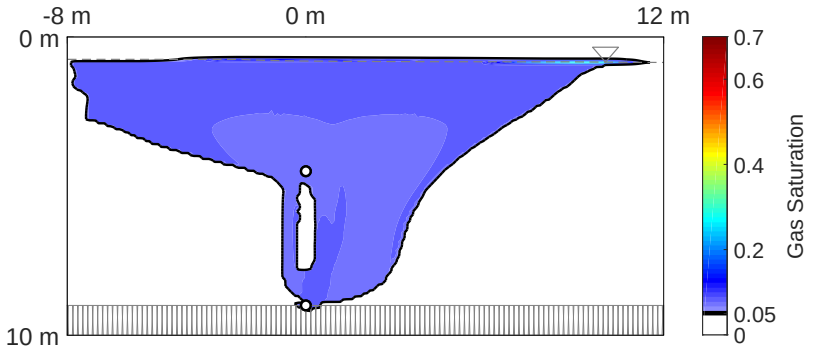

(a) Gas saturation

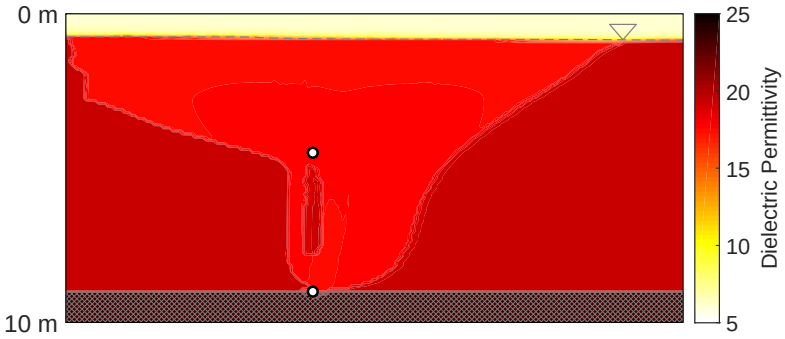

(b) Relative Permittivity

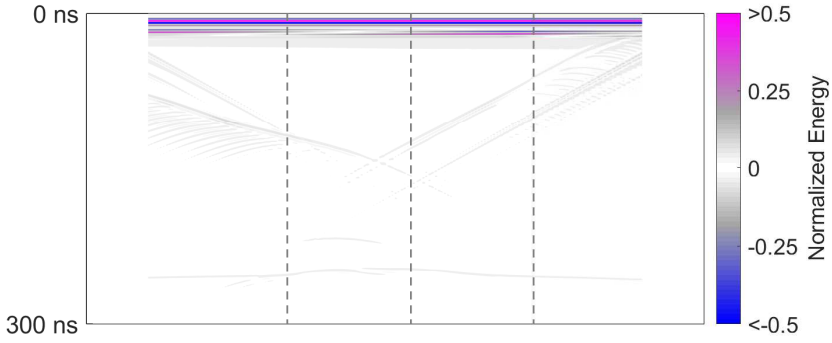

(c) Normalized GPR Amplitude

Figure C.6: Results from saturation model and GPR model, as well as the dielectric permittivity distribution at Day 102 for a homogeneous aquifer. The grey dashed lines show the locations used for the time-lapse plots.

C.2 Layer without Entry Pressure Change

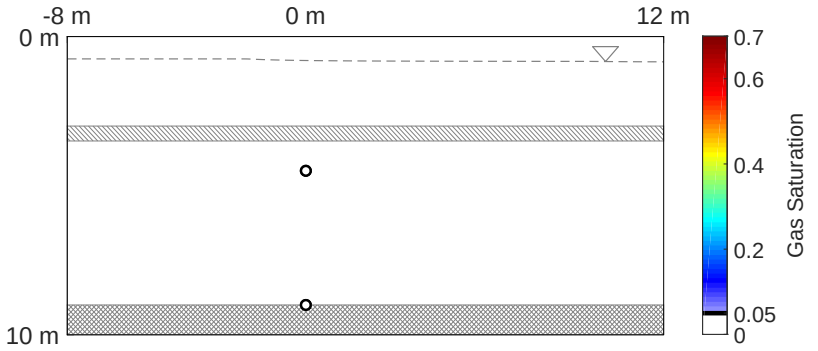

(a) Gas saturation

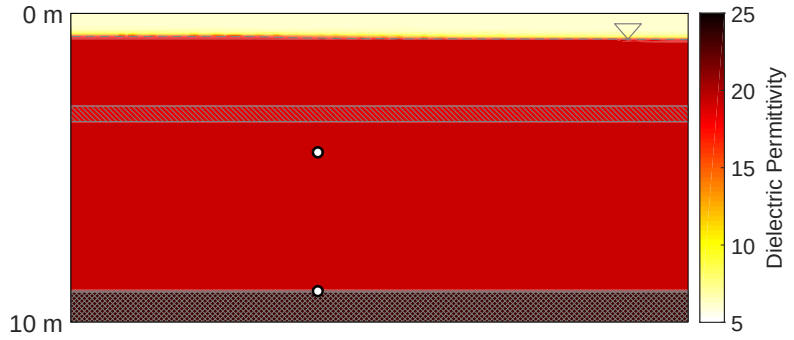

(b) Relative Permittivity

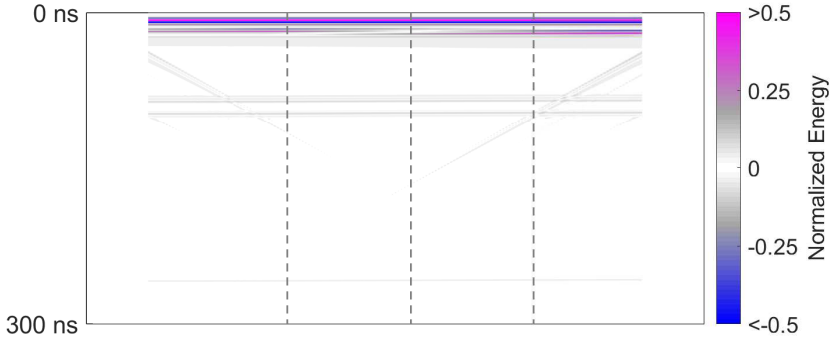

(c) Normalized GPR Amplitude

Figure C.7: Results from saturation model and GPR model, as well as the dielectric permittivity distribution at Day 0 for a continuous layer ($k = 5.1 \times 10^{-13}$, $\phi = 0.31$), no entry pressure change. The grey dashed lines show the locations used for the time-lapse plots.

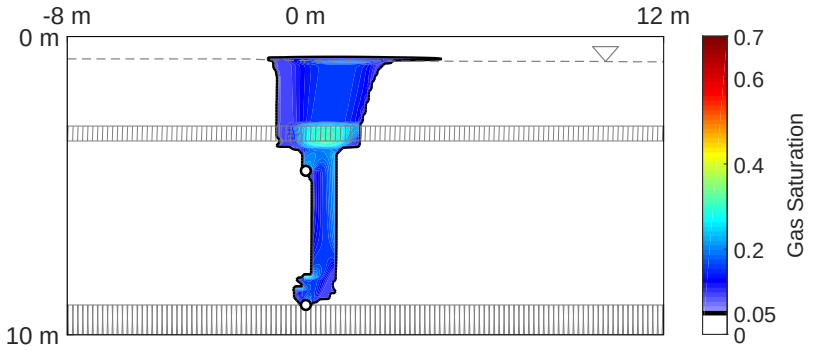

(a) Gas saturation

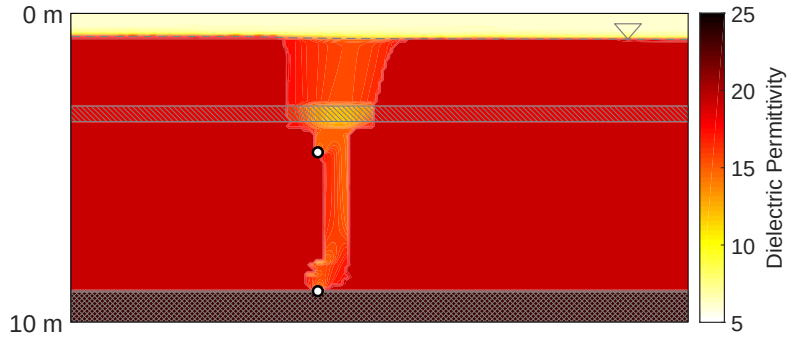

(b) Relative Permittivity

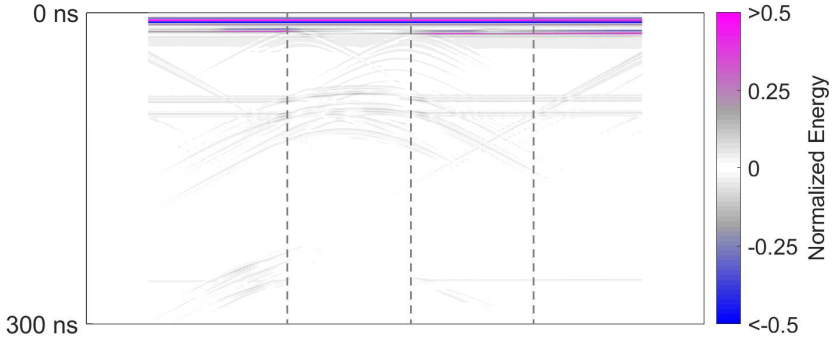

(c) Normalized GPR Amplitude

Figure C.8: Results from saturation model and GPR model, as well as the dielectric permittivity distribution at Day 20 for a continuous layer ($k = 5.1 \times 10^{-13}$, $\phi = 0.31$), no entry pressure change. The grey dashed lines show the locations used for the time-lapse plots.

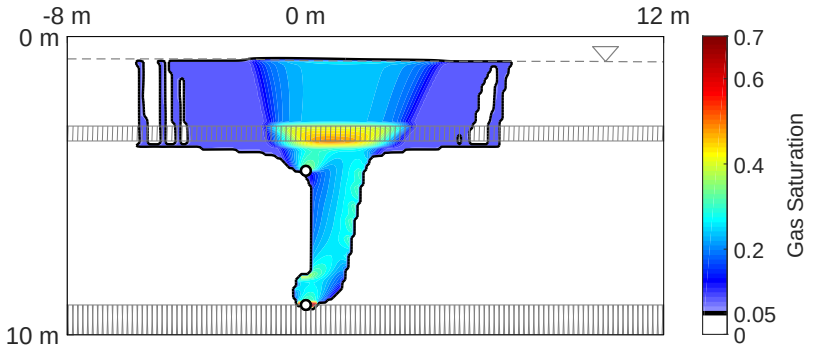

(a) Gas saturation

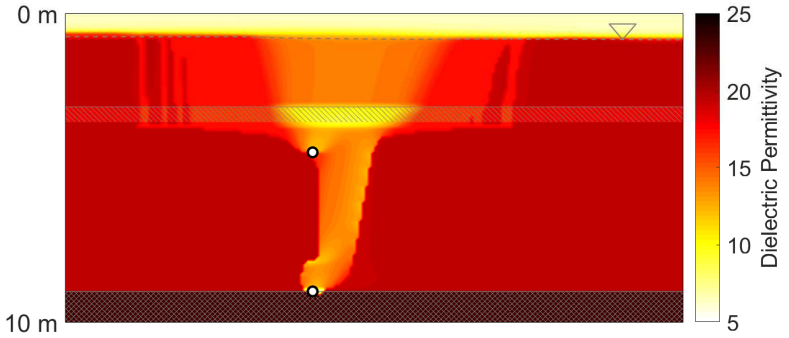

(b) Relative Permittivity

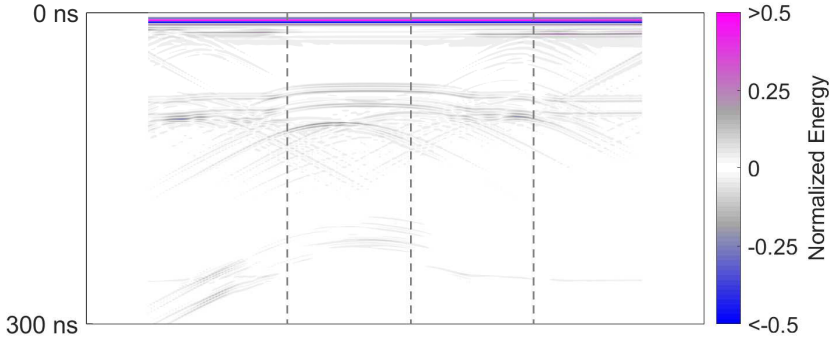

(c) Normalized GPR Amplitude

Figure C.9: Results from saturation model and GPR model, as well as the dielectric permittivity distribution at Day 37 for a continuous layer ($k = 5.1 \times 10^{-13}$, $\phi = 0.31$), no entry pressure change. The grey dashed lines show the locations used for the time-lapse plots.

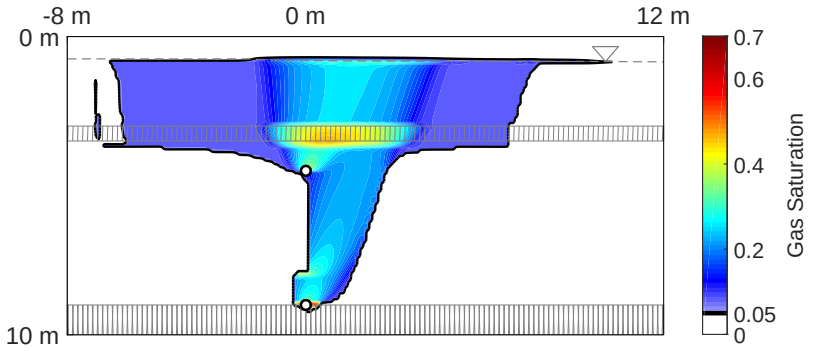

(a) Gas saturation

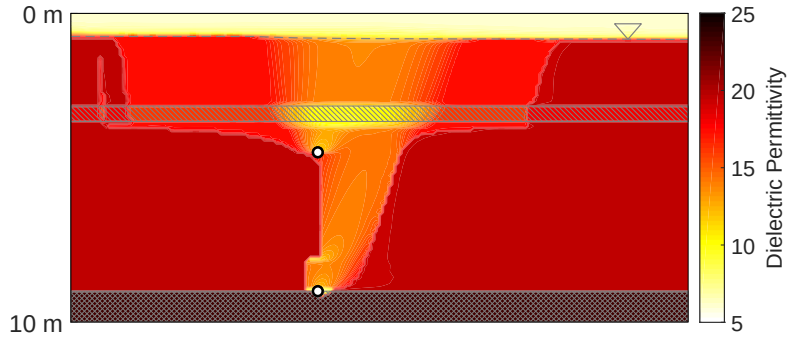

(b) Relative Permittivity

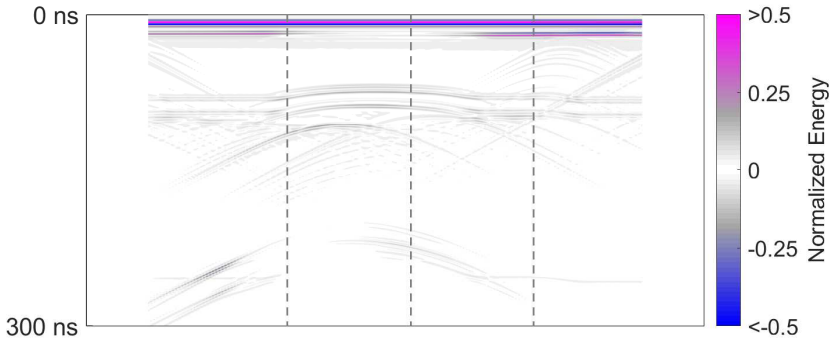

(c) Normalized GPR Amplitude

Figure C.10: Results from saturation model and GPR model, as well as the dielectric permittivity distribution at Day 56 for a continuous layer ($k = 5.1 \times 10^{-13}$, $\phi = 0.31$), no entry pressure change. The grey dashed lines show the locations used for the time-lapse plots.

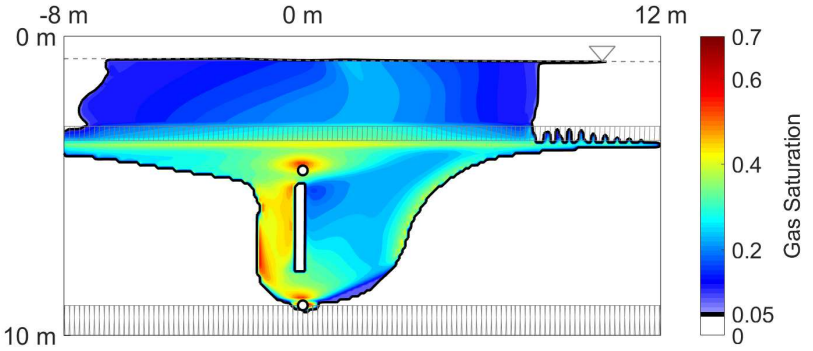

(a) Gas saturation

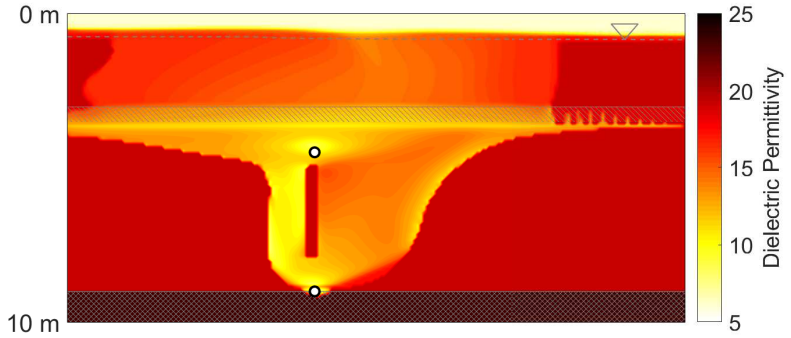

(b) Relative Permittivity

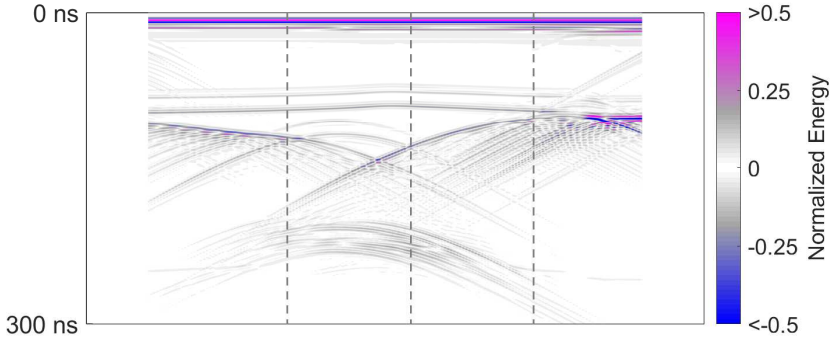

(c) Normalized GPR Amplitude

Figure C.11: Results from saturation model and GPR model, as well as the dielectric permittivity distribution at Day 71 for a continuous layer ($k = 5.1 \times 10^{-13}$, $\phi = 0.31$), no entry pressure change. The grey dashed lines show the locations used for the time-lapse plots.

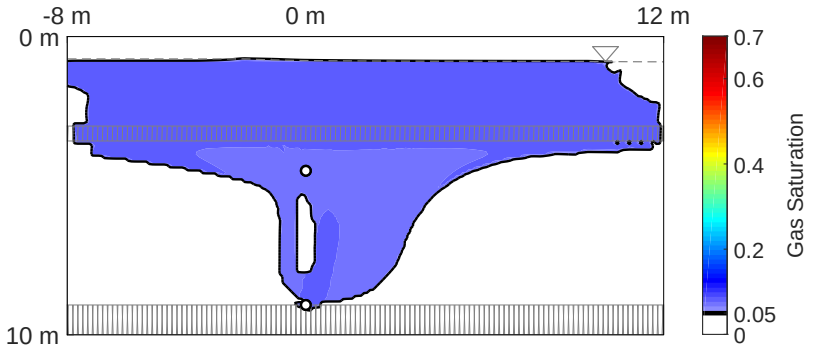

(a) Gas saturation

(b) Relative Permittivity

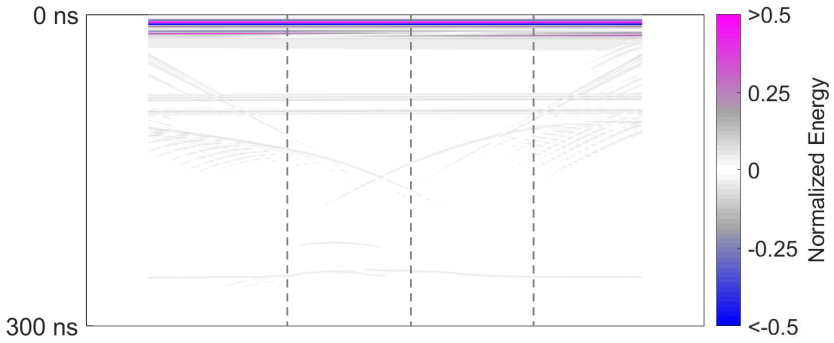

(c) Normalized GPR Amplitude

Figure C.12: Results from saturation model and GPR model, as well as the dielectric permittivity distribution at Day 102 for a continuous layer ($k = 5.1 \times 10^{-13}$, $\phi = 0.31$), no entry pressure change. The grey dashed lines show the locations used for the time-lapse plots.

C.3 Layer with Entry pressure

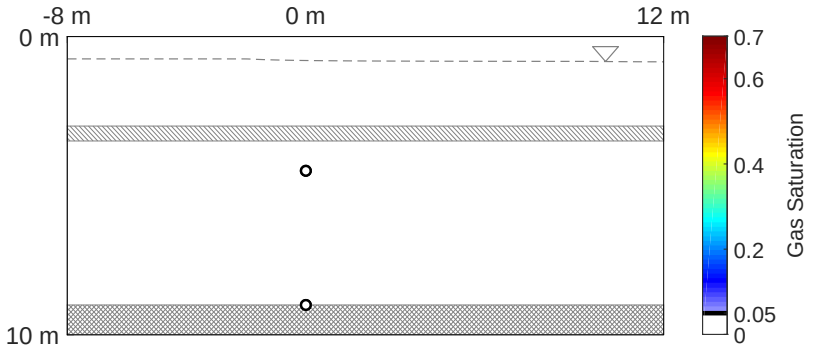

(a) Gas saturation

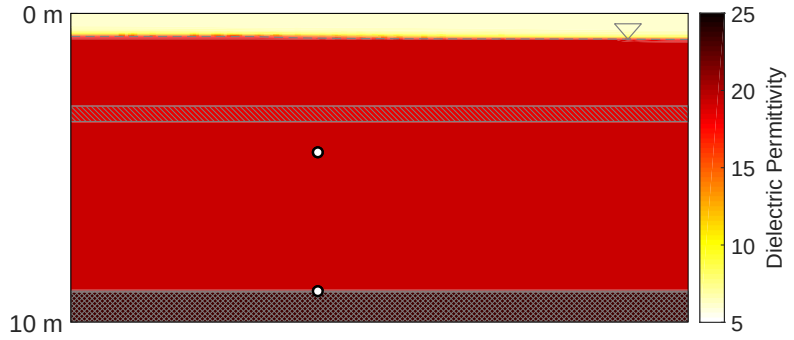

(b) Relative Permittivity

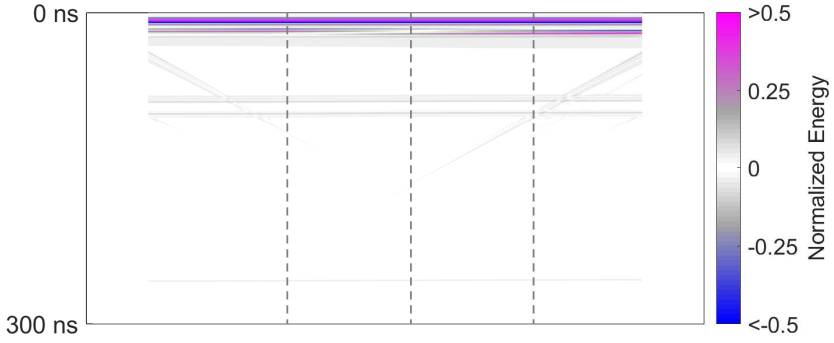

(c) Normalized GPR Amplitude

Figure C.13: Results from saturation model and GPR model, as well as the dielectric permittivity distribution at Day 0 for a continuous layer ($k = 5.1 \times 10^{-13}$, $\phi = 0.31$) with a higher entry pressure ($P_c = 2.99$ kPa). The grey dashed lines show the locations used for the time-lapse plots.

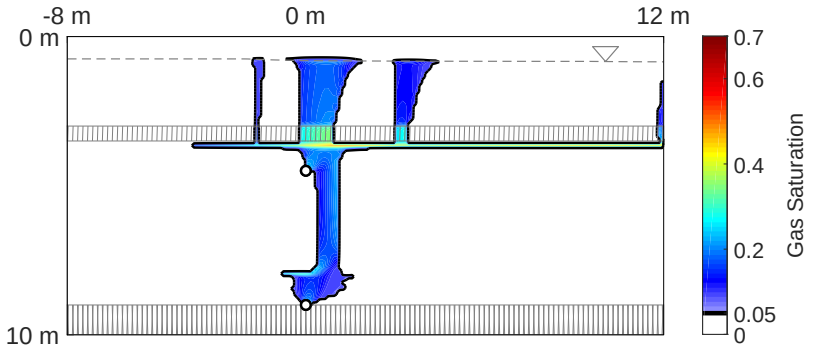

(a) Gas saturation

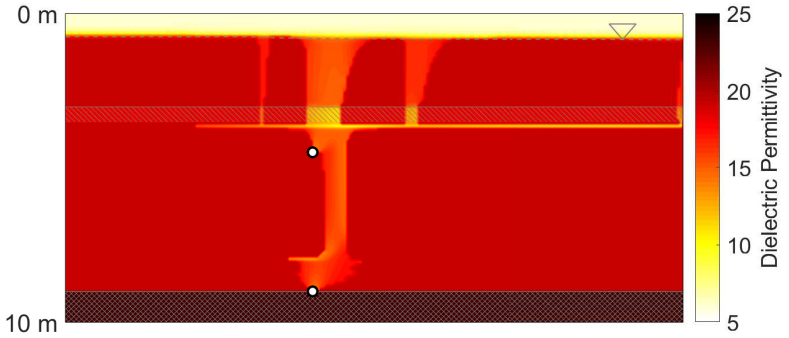

(b) Relative Permittivity

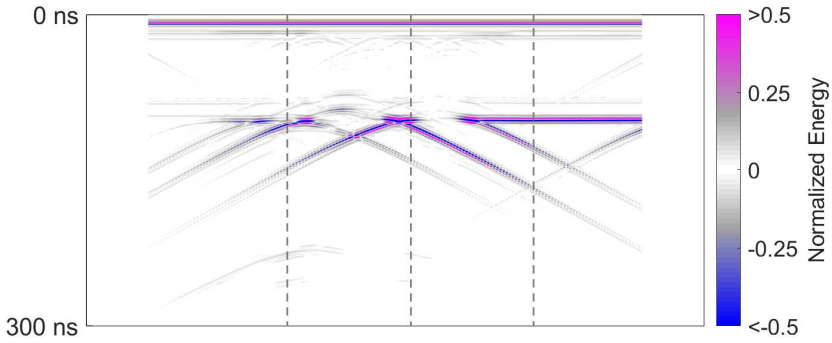

(c) Normalized GPR Amplitude

Figure C.14: Results from saturation model and GPR model, as well as the dielectric permittivity distribution at Day 20 for a continuous layer ($k = 5.1 \times 10^{-13}$, $\phi = 0.31$) with a higher entry pressure ($P_c = 2.99$ kPa). The grey dashed lines show the locations used for the time-lapse plots.

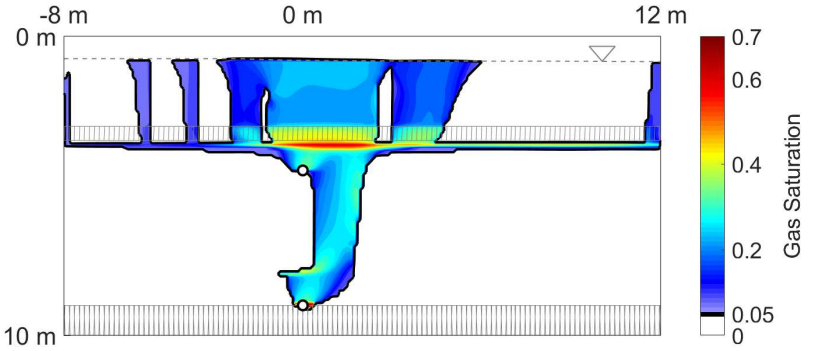

(a) Gas saturation

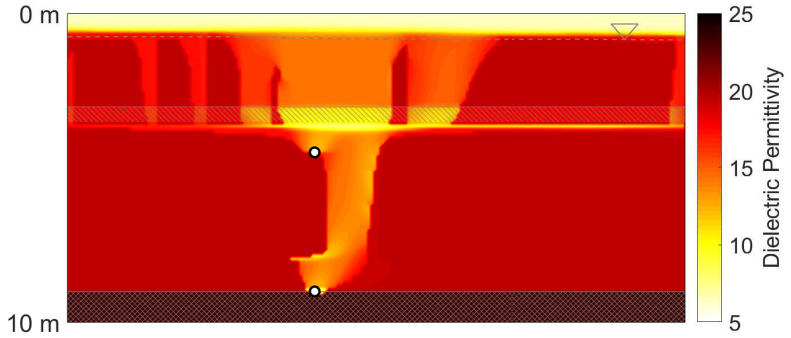

(b) Relative Permittivity

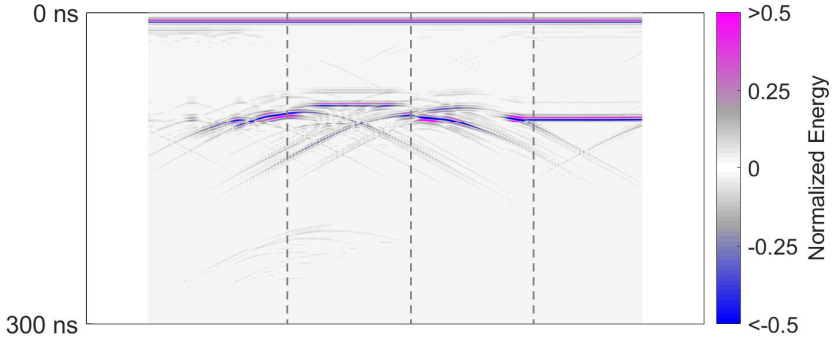

(c) Normalized GPR Amplitude

Figure C.15: Results from saturation model and GPR model, as well as the dielectric permittivity distribution at Day 37 for a continuous layer ($k = 5.1 \times 10^{-13}$, $\phi = 0.31$) with a higher entry pressure ($P_c = 2.99$ kPa). The grey dashed lines show the locations used for the time-lapse plots.

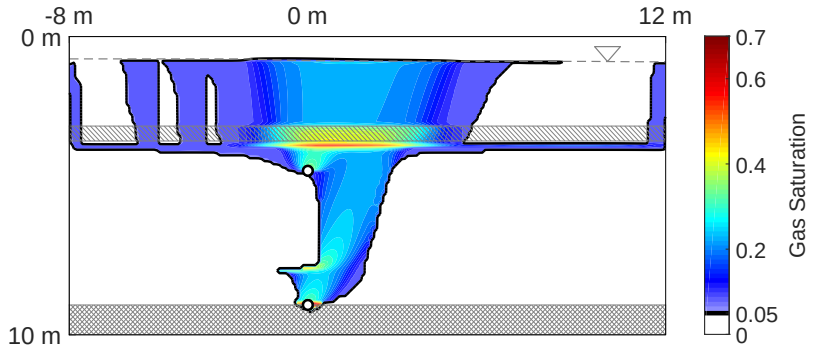

(a) Gas saturation

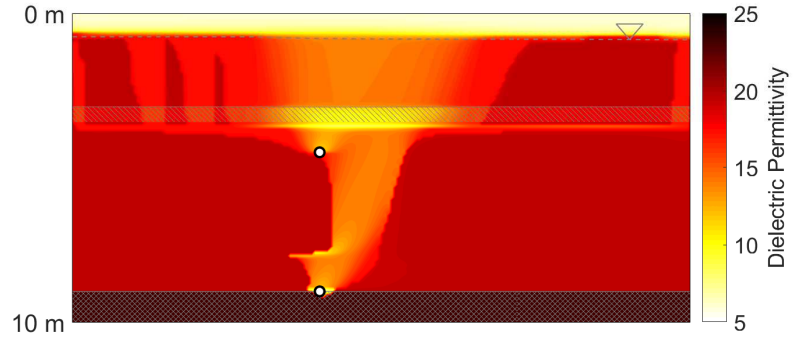

(b) Relative Permittivity

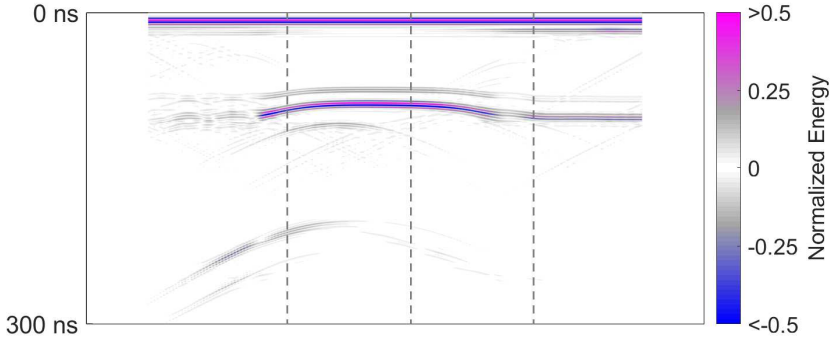

(c) Normalized GPR Amplitude

Figure C.16: Results from saturation model and GPR model, as well as the dielectric permittivity distribution at Day 56 for a continuous layer ($k = 5.1 \times 10^{-13}$, $\phi = 0.31$) with a higher entry pressure ($P_c = 2.99$ kPa). The grey dashed lines show the locations used for the time-lapse plots.

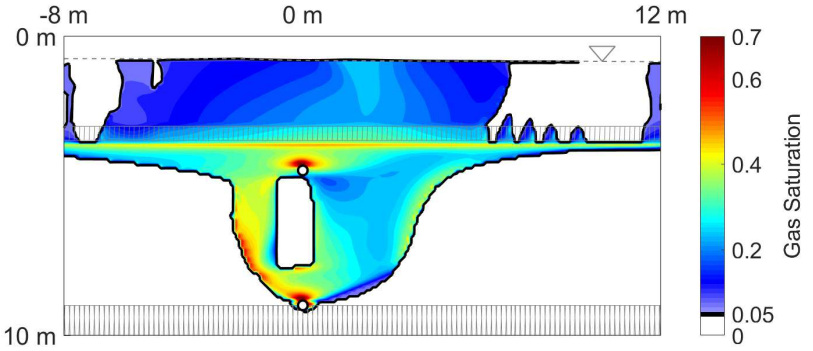

(a) Gas saturation

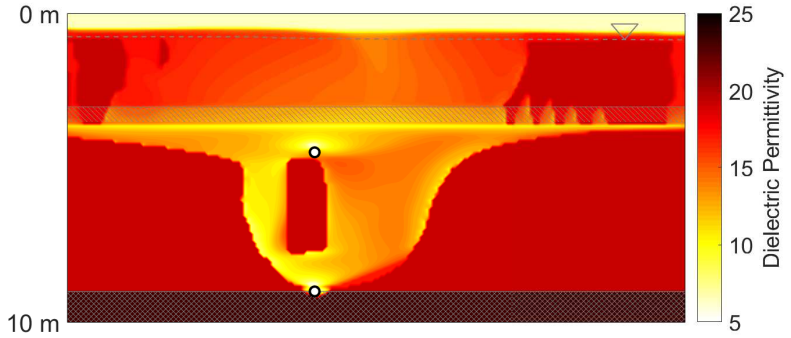

(b) Relative Permittivity

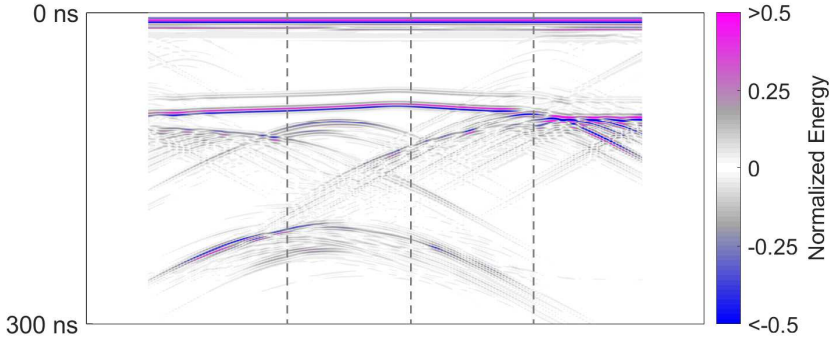

(c) Normalized GPR Amplitude

Figure C.17: Results from saturation model and GPR model, as well as the dielectric permittivity distribution at Day 71 for a continuous layer ($k = 5.1 \times 10^{-13}$, $\phi = 0.31$) with a higher entry pressure ($P_c = 2.99$ kPa). The grey dashed lines show the locations used for the time-lapse plots.

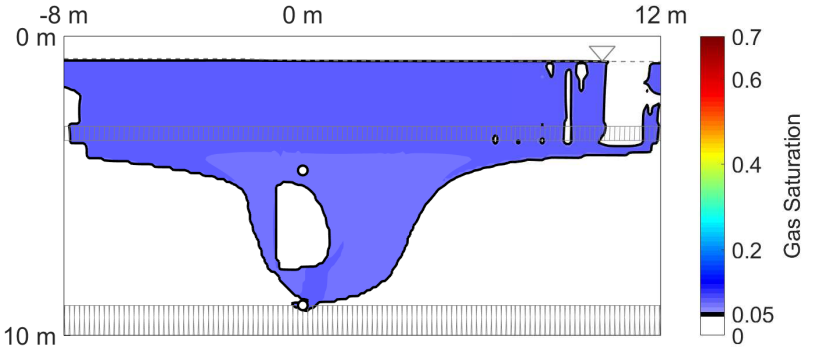

(a) Gas saturation

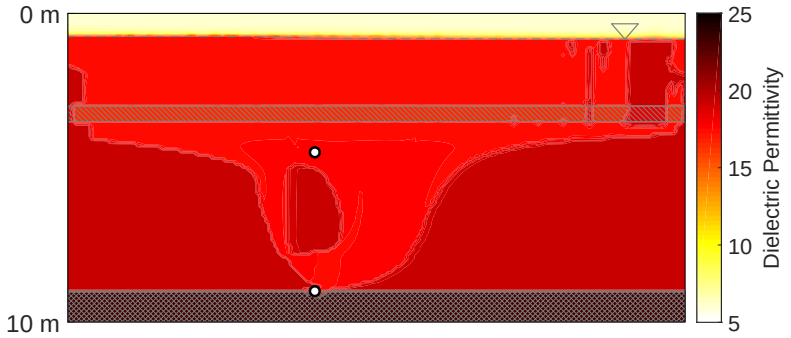

(b) Relative Permittivity

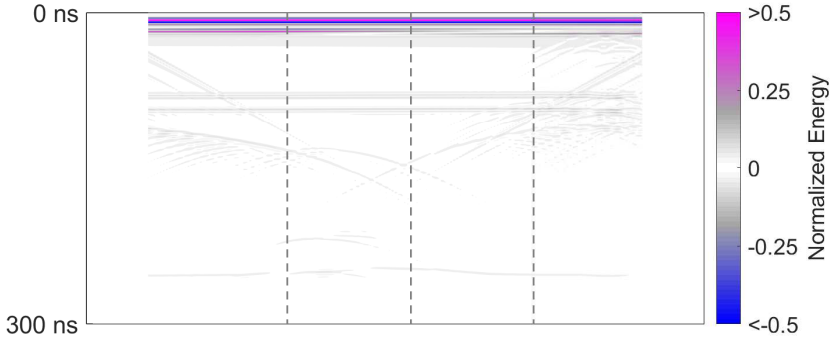

(c) Normalized GPR Amplitude

Figure C.18: Results from saturation model and GPR model, as well as the dielectric permittivity distribution at Day 102 for a continuous layer ($k = 5.1 \times 10^{-13}$, $\phi = 0.31$) with a higher entry pressure ($P_c = 2.99$ kPa). The grey dashed lines show the locations used for the time-lapse plots.

C.4 Discontinuous Layer

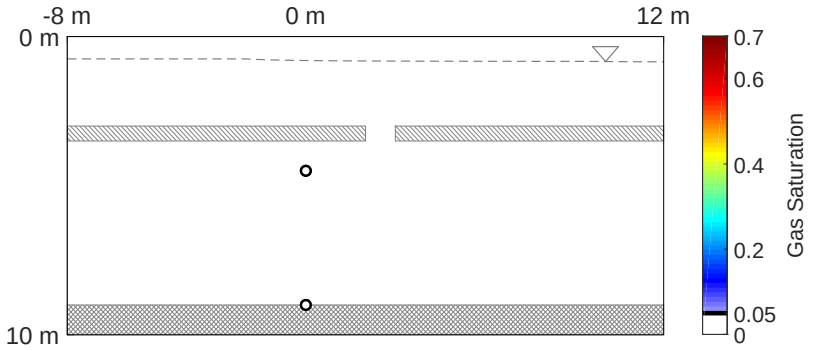

(a) Gas saturation

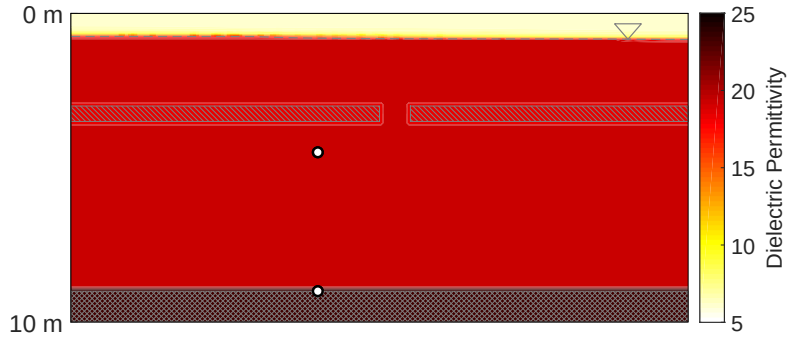

(b) Relative Permittivity

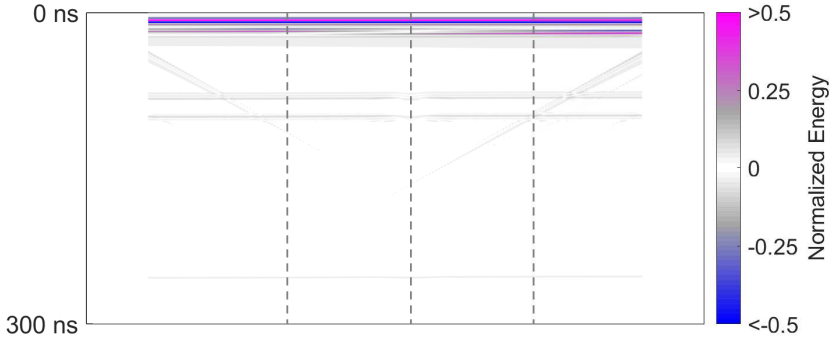

(c) Normalized GPR Amplitude

Figure C.19: Results from saturation model and GPR model, as well as the dielectric permittivity distribution at Day 0 for a discontinuous layer ($k = 5.1 \times 10^{-13}$, $\phi = 0.31$) with a higher entry pressure ($P_c = 2.99$ kPa), discontinuous from 2 m to 3 m. The grey dashed lines show the locations used for the time-lapse plots.

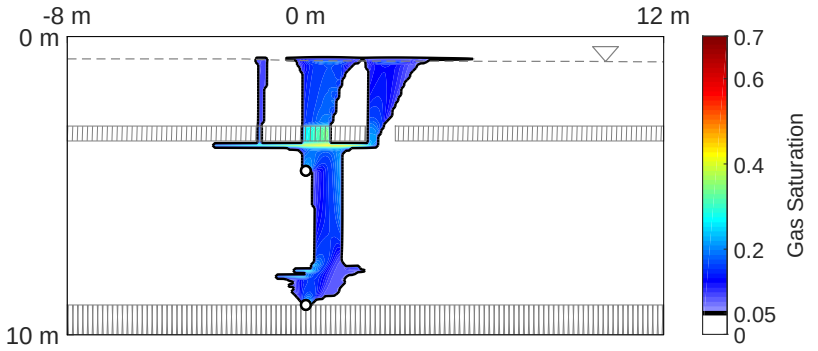

(a) Gas saturation

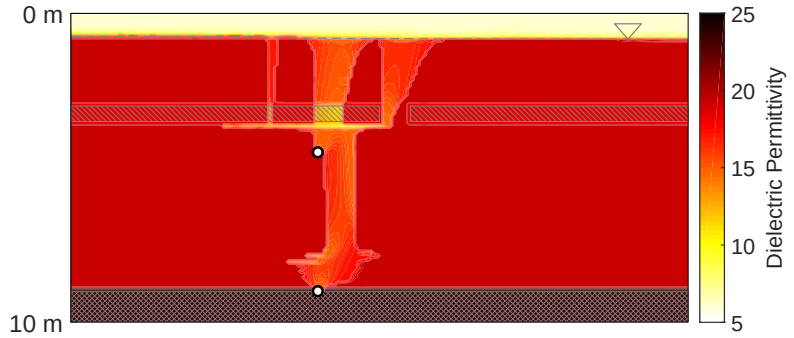

(b) Relative Permittivity

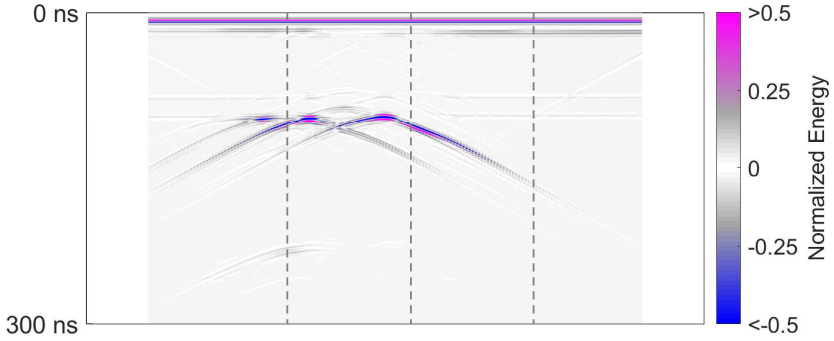

(c) Normalized GPR Amplitude

Figure C.20: Results from saturation model and GPR model, as well as the dielectric permittivity distribution at Day 20 for a discontinuous layer ($k = 5.1 \times 10^{-13}$, $\phi = 0.31$) with a higher entry pressure ($P_c = 2.99$ kPa), discontinuous from 2 m to 3 m. The grey dashed lines show the locations used for the time-lapse plots.

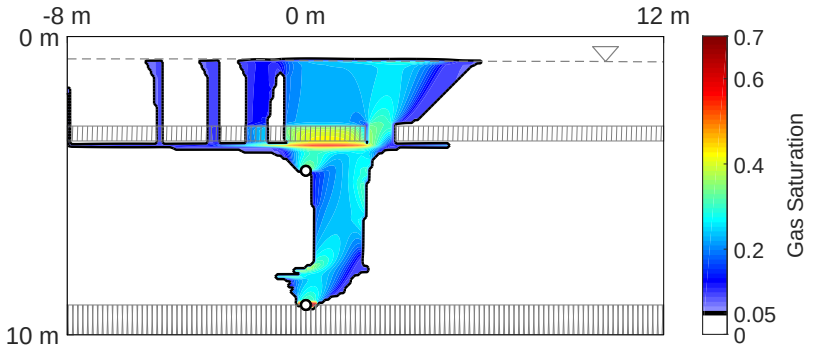

(a) Gas saturation

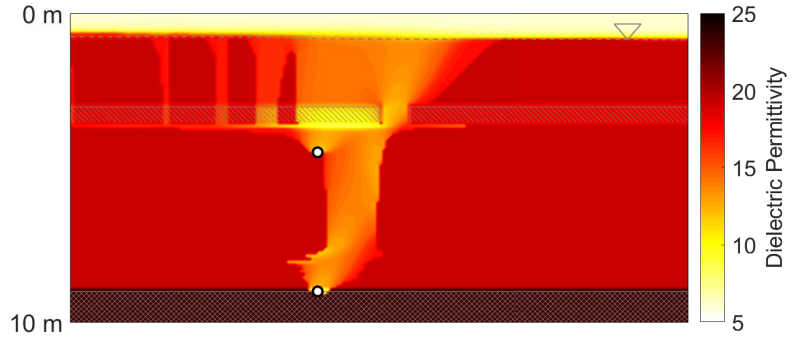

(b) Relative Permittivity

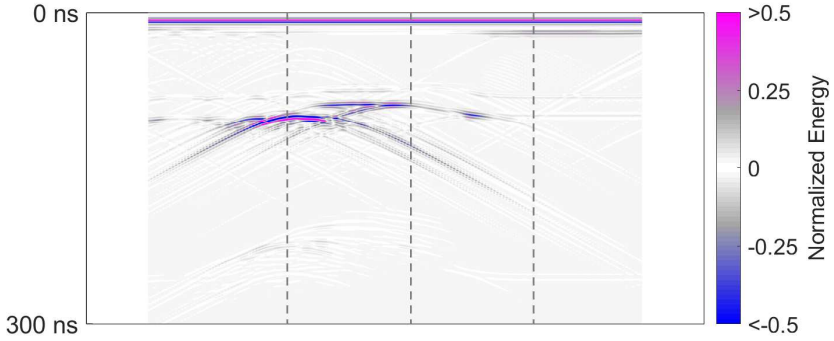

(c) Normalized GPR Amplitude

Figure C.21: Results from saturation model and GPR model, as well as the dielectric permittivity distribution at Day 37 for a discontinuous layer ($k = 5.1 \times 10^{-13}$, $\phi = 0.31$) with a higher entry pressure ($P_c = 2.99$ kPa), discontinuous from 2 m to 3 m. The grey dashed lines show the locations used for the time-lapse plots.

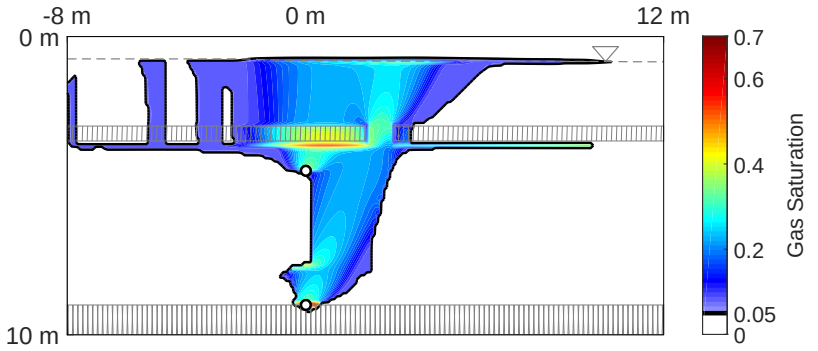

(a) Gas saturation

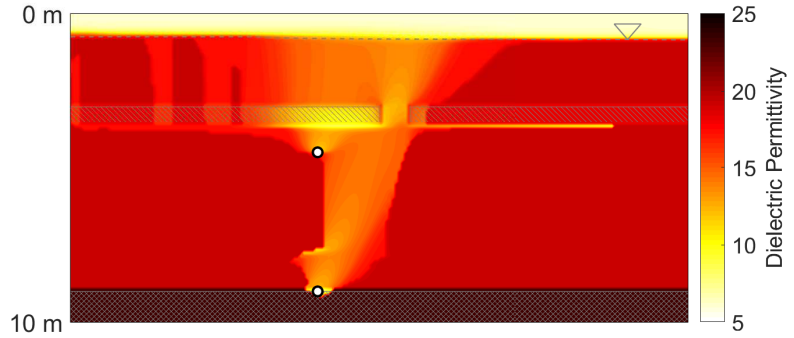

(b) Relative Permittivity

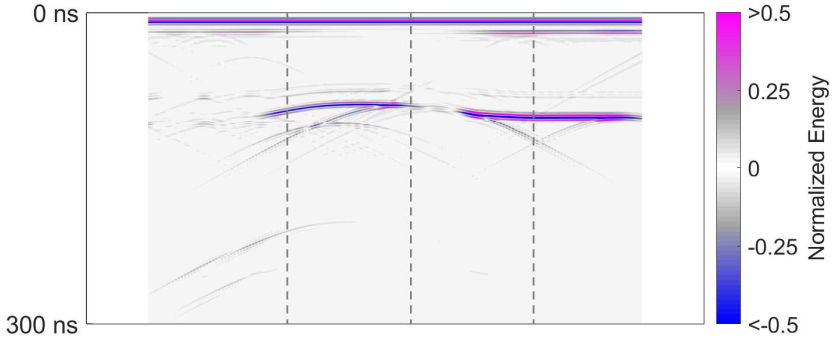

(c) Normalized GPR Amplitude

Figure C.22: Results from saturation model and GPR model, as well as the dielectric permittivity distribution at Day 56 for a discontinuous layer ($k = 5.1 \times 10^{-13}$, $\phi = 0.31$) with a higher entry pressure ($P_c = 2.99$ kPa), discontinuous from 2 m to 3 m. The grey dashed lines show the locations used for the time-lapse plots.

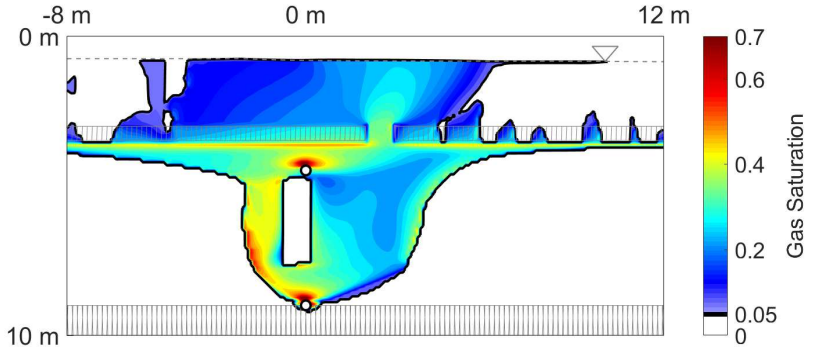

(a) Gas saturation

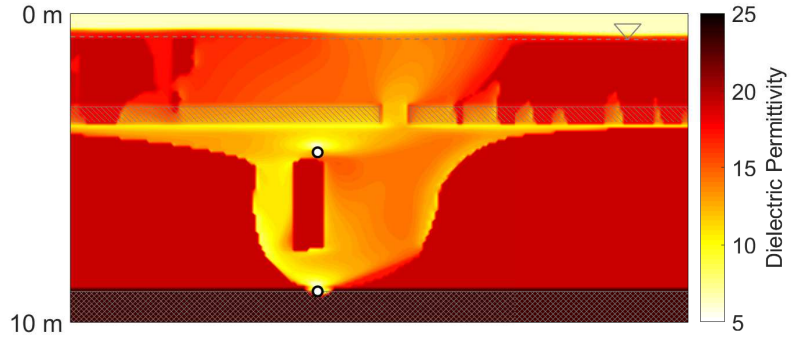

(b) Relative Permittivity

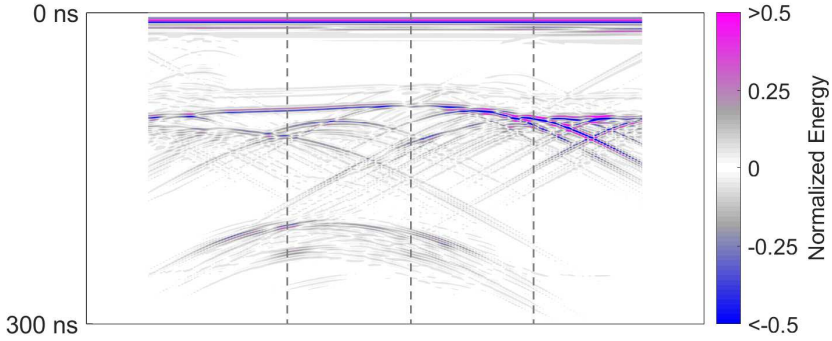

(c) Normalized GPR Amplitude

Figure C.23: Results from saturation model and GPR model, as well as the dielectric permittivity distribution at Day 71 for a discontinuous layer ($k = 5.1 \times 10^{-13}$, $\phi = 0.31$) with a higher entry pressure ($P_c = 2.99$ kPa), discontinuous from 2 m to 3 m. The grey dashed lines show the locations used for the time-lapse plots.

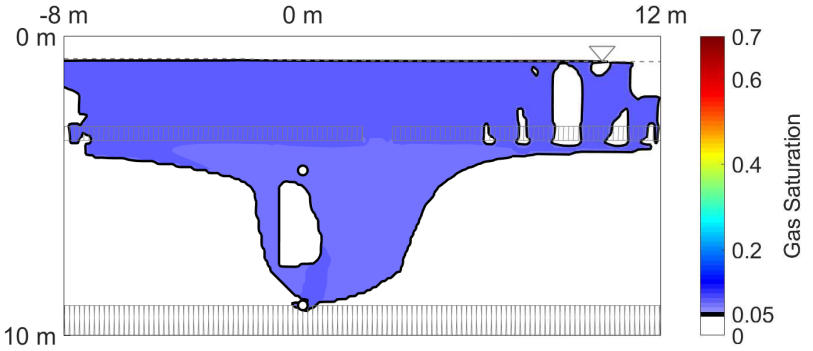

(a) Gas saturation

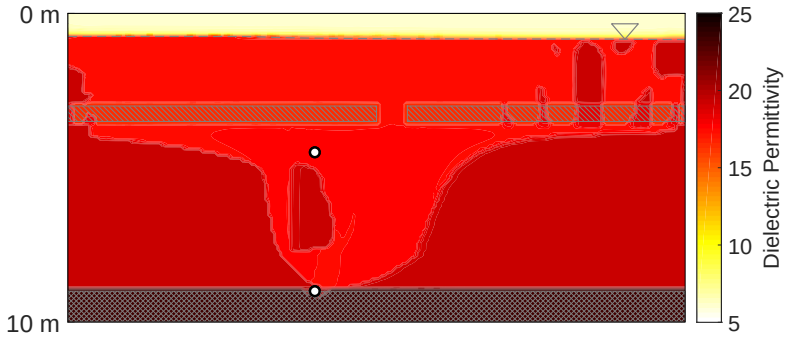

(b) Relative Permittivity

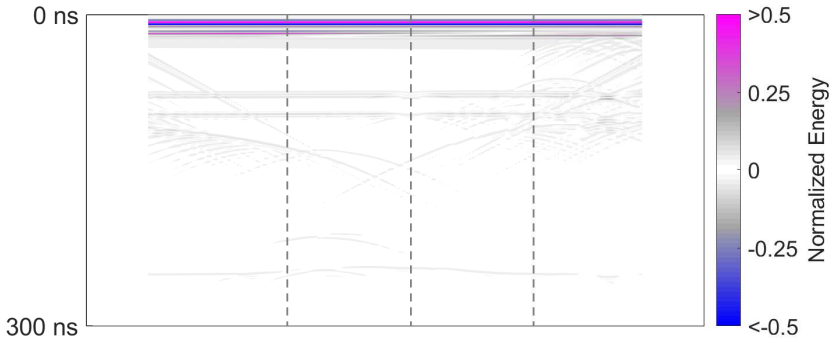

(c) Normalized GPR Amplitude

Figure C.24: Results from saturation model and GPR model, as well as the dielectric permittivity distribution at Day 102 for a discontinuous layer ($k = 5.1 \times 10^{-13}$, $\phi = 0.31$) with a higher entry pressure ($P_c = 2.99$ kPa), discontinuous from 2 m to 3 m. The grey dashed lines show the locations used for the time-lapse plots.